The tonal noise produced by a contra-rotating unmanned aerial vehicle rotor system

Riul Jung

Doctor of Philosophy

Department of Mechanical Engineering

University of Auckland

June 2023

Abstract

Contra-rotating coaxial rotor systems are sometimes used as propulsors for small unmanned aerial vehicles (UAVs) due to their small planform area, high thrust output, and the low torque they impart on the airframe. However, these propulsion systems generate significant levels of noise which is primarily due to the multitude of 'interaction tones' which they produce. These interaction tones occur at the sum of harmonics of the blade passing frequencies of each rotor and are produced by the periodic unsteady loading on the rotor blades caused by their interaction with the periodic unsteady flow produced by the adjacent rotor. This thesis describes a detailed investigation into these interaction tones.

This thesis presents two methods for predicting the unsteady periodic loading on the rotor blades. The first method uses loading data directly taken from computational fluid dynamics (CFD) simulations, whilst the second method is semi-analytic and predicts the unsteady loading due to the bound potential field produced by the adjacent rotor interacting with the rotor. A novel frequency-domain method is also presented for directing calculating the far-field sound radiated from the rotor system. Predictions made using these methods agree well with experimental measurements made in an anechoic chamber. The agreement of the predictions made using the CFD and the semi-analytical model suggests that bound potential field interactions are a significant cause of the interaction tones.

Several methods for attenuating these interaction tones are explored. The effect of skew angle on the interaction tones is investigated using the prediction methods presented in this thesis. The prediction methods also correlate well with experimental data for various skew angled blades. It is shown that skew angle can reduce the level of the interaction tones significantly without compromising aerodynamic performance. Secondly, the effect of cropping the bottom rotors on the interaction tones is explored. Cropping the bottom blades can have a minor effect on the radiated noise. Lastly, the effect of changing the pitch angle of the bottom blades on the interaction tones is explored.

Acknowledgements

Table of Contents

List of Figures

List of Tables

1. Introduction

1.1 Motivation

Unmanned aerial vehicles (UAVs) using multirotor propulsion systems have become increasingly popular in recent years due to their affordability and versatility. Colloquially referred to as "drones", these vehicles provide a stable platform in the air where a variety of equipment such as cameras and microphones can be mounted. Due to their utility in many industries, new and useful applications for drones have developed rapidly. The rotors used to provide thrust to the UAVs can be arranged in a variety of configurations. Typically, vertical take-off and landing (VTOL), multirotor UAVs use 4, 6 or 8 rotors mounted in the same plane and distributed around the UAV. A drone typically uses several single rotors as its propulsion system. An alternative or perhaps a better rotor arrangement to this is the contra-rotating coaxial rotor configuration. This arrangement uses two rotors which are mounted coaxially, but which rotate in opposite directions.

The main benefit of using contra-rotating rotors on UAVs is the additional thrust that they provide without increasing the planform area of the rotor system. An additional benefit is that the net torque imparted on the airframe by a contra-rotating rotor system is typically significantly lower than an equivalent single rotor, which provides more stability. The additional rotor can also provide redundancy in case of the failure of one rotor.

A potential disadvantage of contra-rotating rotor systems is the generally higher levels of noise which they produce in comparison to equivalent single rotors. This is attributed to the interaction tones produced by the periodic loading on the rotor blades caused by their interaction with the unsteady periodic flow from the adjacent, contra-rotating rotor. Prior to the start of the work described in this thesis, there had been little work done investigating the physical mechanisms responsible for the noise produced by contra-rotating rotor systems for use on small UAVs.

The noise produced by a subsonic UAV rotor is primarily due to the thickness and loading noise sources on the surface of the rotor blades. The interaction tones produced by a contra-rotating system are caused by the periodic unsteady loading on the rotor blades due to their interaction with the flow field produced by the adjacent contra-rotating rotor. Therefore, this work focusses on analysing the unsteady aerodynamics which generates this unsteady loading in order to explain how these interaction tones are produced. Although previous work has been done on contra-rotating rotors for aeroplanes and helicopters, the rotors used on UAVs are relatively small and slow moving compared to those used on larger aircraft – which makes this problem unique.

1.2 Background

This chapter presents a review of previous research work relevant to the tonal noise produced by contra-rotating UAV rotor systems. This includes a brief review of work investigating the aeroacoustics and aerodynamics of small UAV propellers as well as work done on the aeroacoustics of other contra-rotating propulsion systems such as helicopter rotor systems and the contra-rotating propeller designs intended for use on large, fixed wing aircraft (which are often referred to as "contra-rotating open rotors", "advanced open rotors", or "contra-rotating unducted fans"). Section 1.2.4 presents a review of recent work done by other investigators on the noise produced by contra-rotating UAV rotor systems and sections 1.2.5 and 1.2.6 present an overview of the experimental and numerical methods which can be used to investigate UAV rotor noise.

It should be noted that there are similarities and differences between contra-rotating rotors used on aircraft, helicopters, and multi-rotor UAVs. In particular, the differences in the size of the rotors and the speeds at which they operate means that the aerodynamics and resulting noise produced by small

UAV propellers are somewhat different to those of large aeronautical propulsors (with these typically operating at much higher Reynolds and Mach numbers). The solidity and number of blades used on a UAV propeller are also typically much lower than those of a contra-rotating open rotor design. The Reynolds number of a helicopter rotor based on blade chord-length and speed at a radius equal to 75% of the tip radius is typically in the order of 10^6 compared to 10^4 for the equivalent location on small UAV rotor blades at a typical operating condition. It is therefore expected that the boundary layer on the surface of the helicopter blades will be turbulent, while the boundary layer on the surface of a UAV rotor blade may be laminar or transitional during operation. In addition, helicopter rotors commonly operate with tip Mach numbers of 0.7 – 0.8 which means that the compressibility of the flow must be considered. On the other hand, UAV rotors typically operate with tip Mach numbers less than 0.3 and thus the flow can be treated as being incompressible for the purposes of aerodynamic analysis. Lastly, typical UAV propellers have 2 or 3 thin blades with small chord-lengths and thus these propellers typically have low solidity, whereas modern rotor designs for fixed wing aircraft can have 10 blades or more and relatively high solidity. It is therefore expected that there will be some differences between the aerodynamics and noise generation mechanisms which are important for the different propulsor types. Nevertheless, these examples should provide some insight.

1.2.1 Noise produced by single subsonic rotors

The sources of noise produced by a propeller can be divided into tonal (deterministic) and broadband (non-deterministic) components [1]. For a subsonic propeller, the tonal components can include thickness noise, steady loading noise, and periodic loading noise. The non-linear quadrupole sources in the flow around transonic and supersonic propellers also produce significant levels of noise for those cases. However, that noise source is not relevant to UAV propellers and is not discussed further here.

Thickness noise is caused by the displacement of the surrounding air by the rotor blade. Steady and unsteady loading noise is due to the steady and unsteady stresses exerted on the fluid by the rotor blade surface. In the case of a single helicopter rotor in forward flight, periodic loading occurs due to the change in velocity of the blade relative to the air as it simultaneously rotates and translates through the air and because of interaction of each propeller blade with the tip vortex from the preceding blade. The former source can become impulsive in nature when the tip speed of the blade is transonic in which case it is referred to as high-speed impulsive noise.

Zawodny et al. [1] investigated the thickness and steady loading noise produced by a single conventional UAV propeller using computational methods. This investigation included the use of an unsteady Reynolds-averaged Navier Stokes (URANS) computational fluid dynamics (CFD) code to estimate the steady loading on the blade surfaces. This loading data was fed into an acoustical analogy method [4] based on the Ffowcs-Williams and Hawkings equation which was used to compute the acoustic pressure time histories at defined observer locations due to the steady loading and thickness noise sources. Predictions were also made using loading data calculated from a blade element theory code. Sound pressure level predictions made using the two methods were in good agreement with experimental data for the first and second harmonics of the blade passing frequencies of the propellers at observer locations close to the plane of the propeller.

Broadband noise is caused by the unsteady stresses on the blade surface due to turbulent flow. This turbulent flow can come from different sources including turbulence in the atmosphere, turbulence from the wake of the preceding rotor blade, and turbulence in the boundary layer and near-wake adjacent to the rotor blades. Noise produced by these mechanisms is often referred to as turbulence ingestion noise, blade-wake interaction noise, and blade self-noise, respectively.

Nardari et al. [2] have found that turbulence ingestion noise produces a significant number of 'quasi-tonal' peaks in the sound pressure level spectrum which occur at harmonics of the BPF. The ingested turbulent structures are tilted, stretched, and elongated in the axial direction. This means that a single turbulent eddy can be 'chopped' multiple times by the propeller causing unsteady blade loading which is correlated over several blade passages. Nardari et al. [2] predicted the noise produced by a UAV propeller installed in an anechoic chamber using a computational method and drew comparisons with experimental results. They identified that flow confinement effects within the anechoic chamber could be significant and lead to high levels of turbulence ingestion noise. If the turbulent eddies ingested by the propeller are not sufficiently long in the axial direction to be chopped multiple times by the propeller blades, then turbulence ingestion will produce broadband noise [3,4]. Glegg et al. [4] have developed a theoretical model for the prediction of turbulent inflow noise using a time domain approach. The comparison between measured and predicted spectra showed good agreement and they claim that the time domain calculations were much faster than the equivalent computations based on a frequency domain method.

A number of methods have been developed for predicting blade-wake interaction noise. In particular, Glegg [5] developed a model which utilised a turbulent vortex model to represent the wake of the preceding blade and then implemented a method similar to that used for theoretical turbulent inflow noise prediction methods to calculate the radiated noise field.

Aerofoil self-noise is generated by the pressure fluctuations in the turbulent boundary layer and wake of the aerofoil being scattered by the aerofoil surface (principally the surface close to the trailing edge). Types of self-noise include turbulent boundary layer trailing edge noise, separation-stall noise, laminar boundary layer vortex shedding noise, tip vortex formation noise, and trailing edge bluntness vortex shedding noise. Brooks, Pope and Marcolini [6] present an empirical model for predicting the self-noise produced by a NACA0012 aerofoil operating at different angles of attack and Reynolds numbers. This model was developed using a comprehensive dataset obtained from wind tunnel experiments. They also describe how the model can be applied to predict the noise from a rotor and present comparisons of the predictions made using this approach with experimental data. Zawodny et al. [1] have used this approach to calculate the self-noise produced by a single UAV propeller. It is important to note, however, that the method assumes that the rotor blade sections produce similar levels of self-noise in comparison to those produced by a NACA0012 aerofoil – which is likely to be a poor assumption. Nevertheless, this prediction method provides insight to the prominent broadband noise source mechanisms of UAV propellers. Zawodny et al. were able to use this method to show that the turbulent boundary layer trailing edge noise was the prominent broadband noise source for single UAV propellers at high frequencies.

1.2.2 Noise produced by horizontal-axis contra-rotating propellers
Contra-rotating propellers will also produce interaction tones caused by the periodic unsteady loading on the rotor blades due to their interaction with the flow field from the adjacent propeller. The unsteady loading on the rear propeller is caused by its interaction with the wakes, tip vortex and bound potential field of the front propeller. The unsteady loading on the front propeller is due only to its interaction with the bound potential field of the rear propeller [7].

Hanson [8] and Parry [11] present frequency-domain methods for calculating the sound pressure of particular interaction tones. Parry presents methods for calculating the unsteady loading caused by the viscous wake interaction with the rear propeller and the bound potential field interactions for both propellers. Magijji et al. [9], Kingan and Self [10], and others (e.g., [11–14]) have presented methods for calculating the unsteady loading due to the tip vortex from the front propeller interacting with the rear propeller.

Blandeau and Joseph [15] investigated the broadband noise due to the interaction of the turbulence in the front propeller wake with the rear propeller of a contra-rotating open rotor. They conducted a

parameter study investigating the effect of blade number, rotor-rotor gap and rotor speeds on the broadband noise level. Based on the theoretical model developed by Blandeau and Joseph, Kingan [16] developed an extended model which could be applied to calculate the noise produced by the interaction of the turbulent wake from an upstream pylon with a propeller.

Parry et al. [17] investigated the relative importance of the tonal and broadband noise produced by a model-scale contra-rotating open rotor. They found that the broadband noise was an important contributor to the total noise level for the particular design and operating conditions they investigated. Kingan et al. [18] compared predictions of the noise produced by the same model-scale open rotor with measurements. The predictions were made using an analytical method in which the radiated noise was calculated using a frequency domain method similar to that of Hanson and Parry, with the blade loading calculated using unsteady 2D aerofoil theory. The method required estimates of the steady loading (lift and drag) on the propeller blades and the induced flow (swirl and induced axial velocity) produced by the propellers. These were estimated by both a "strip-theory" method and steady Reynolds-averaged Navier Stokes (RANS) CFD simulations. The predictions showed modest agreement with the measurements. This was attributed to errors in the unsteady loading predictions either due to the accuracy of the steady aerodynamic predictions or inaccuracies of the analytical prediction methods.

Noise can also be predicted by using unsteady CFD simulations to directly predict the periodic unsteady loading on the blades of the propellers and an acoustic analogy approach to calculate the radiated noise field. Such an approach is computationally intensive but has been used by a number of researchers e.g. refs. [19-21]. An intermediate approach is described in ref. [19] in which unsteady CFD is used to calculate the unsteady flow field produced by the front propeller and then analytical methods are used to calculate the resulting unsteady loading on the rear propeller blades and the radiated sound pressure field.

A number of recent theoretical studies [20–24] on the interaction tones produced by large horizontal-axis contra-rotating propeller systems, suggest that significant reductions in noise may be produced by using curved – or 'swept[1]' – blades. For example, Kingan & Parry [22] presented asymptotic formulae for predicting the sound pressure level of the interaction tones produced by the unsteady loading on the downstream propeller due to its interaction with the wake from the upstream propeller (which is assumed to be the dominant noise source for these engines). These formulae are simple algebraic expressions which can be calculated with little computational expense, and which explicitly show the dependence of the radiated noise on the geometry of the propellers and the operating condition. In a subsequent paper, Kingan & Parry [23] used the asymptotic formulae to investigate the effect of sweeping the downstream propeller blades and showed that as the sweep increases past a critical point, the level of an interaction tone decreases very significantly. Kingan & Parry [24] investigated this effect further using a time-domain analysis. They showed that 'sweeping' the downstream propeller blades caused a lag between the times that the wake from an upstream propeller blade impacted on the leading-edge of a downstream propeller blade and that this in turn could produce a lag between the times at which the impulsive noise generated at different radii reached an observer location. This 'de-phasing' could result in a total acoustic pressure impulse of much lower amplitude compared with that produced by a propeller system with straight blades. They noted that in order to obtain noise reductions at all observer locations, the leading-edge sweep must be large enough so that the trace velocity of the wake centreline across the leading edge of the downstream rotor blades is subsonic. This ensures that the peak acoustic pressure of the impulses generated at different radii never occur at the same time at any observer location.

---

[1] Sweep is defined as the distance the mid-chord location of a blade section is offset from the pitch-change axis along the helical path of the blade.

Although the aerodynamics of horizontal contra-rotating propellers for an aircraft differs from a UAV contra-rotating propeller, the noise generation mechanisms described here should be similar. The challenge for the work presented in this thesis was to correctly identify which sources are important for contra-rotating UAV propellers and to develop methods for predicting the unsteady loading caused by them and the resulting interaction tones.

1.2.3 Noise produced by coaxial helicopter rotor systems

In this section, a review of studies investigating the noise produced by coaxial helicopter rotors is presented.

Walsh et al. [25] investigated the noise produced by a coaxial, contra-rotating helicopter rotor system in highspeed forward flight. Loading noise was found to be dominant for observer locations away from the rotor plane. This loading noise included the noise produced by the impulsive loading caused by blade vortex interaction within each rotor, rotor-wake interaction between the two rotors or "aerodynamic interference" caused when the rotors crossed each other.

Kim et al. [26] numerically computed the loading and thickness noise produced by the blades of a contra-rotating helicopter rotor system using Farassat's formulation 1A. They found that the noise level produced by the lower rotor was significantly higher than that from the upper rotor over the entire frequency range. They attributed this to the strong unsteady loading on the blades of the lower rotor due to their interaction with the tip vortices of the upper rotor. In a separate study [27], they investigated the effect of changing the axial gap between the two rotors and found that increasing the gap by 30% resulted in a marginal decrease (3dB) in the noise produced by the rotor system. This was expected as the tip vortex strength remains relatively unchanged as it propagates downstream over the different separation distances investigated. A similar study was reported in Kim et al. [28]. Yoon et al. [29] conducted a URANS simulations of the contra-rotating rotors used on an XV-15 helicopter. They found that the fuselage beneath the rotors distorted the trajectory of the tip vortices from the rotors and that the vortices from the upper rotor convects radially inwards before impinging on the lower rotor. This vortex interaction produced unsteady loading on the lower rotor which produced impulsive noise.

Barbely et al. [30] investigated the aerodynamic interactions of coaxial rotors using CFD simulations. In order to understand the aerodynamic interactions occurring at a particular radius, they also considered a simplified two-dimensional case in which two aerofoils translate past each other in opposite directions. Simulations of the simple case clearly demonstrated the impulsive loading which occurred on each blade as it passed the other. As the distance between the aerofoils increased, the magnitude of this impulsive loading on both rotors decreased significantly – which suggests that bound potential field interactions were the significant cause of this loading.

The studies described above investigating the noise produced by contra-rotating helicopter systems all used numerical approaches to investigate the noise. These investigations typically use Farassat's formulation 1A to calculate the radiated noise source using the unsteady loading from a CFD solution as input. These studies were able to identify the contribution the loading on each rotor made to the total noise level. A similar approach can be used to study the aerodynamics and noise produced by a contra-rotating UAV rotor system. Although, the Mach number and Reynolds number characterising the flow through a UAV rotor system are significantly different to those of a helicopter rotor system, the underlying fundamental aerodynamic characteristics such as the bound potential field and tip-vortex are present for both systems. The importance of the bound potential field interactions could be investigated by considering the simplified 2D aerofoil interaction case similar to that simulated by Barbely et al. [30].

1.2.4 Noise produced by contra-rotating UAV rotor systems

The cause of the periodic unsteady loading on the blades of a contra-rotating UAV rotor system has been investigated by Lakshminarayan and Baeda [31] who report an experimental and numerical study on the aerodynamics of a micro-scale contra-rotating UAV rotor system operating at different rotational speeds and with different rotor spacings. They found that an impulsive force occurred on both rotors when the blades were close to being aligned, but that the impulsive force on the bottom rotor had slightly different characteristics to that acting on the top rotor which they attributed to the impingement of the wake and tip vortex from the top rotor. They also observed that the magnitude of the fluctuating force on the top rotor decreased with increasing rotor spacing. However, the magnitude of the fluctuating force on the bottom rotor initially decreased with increasing rotor spacing, but then increased at larger spacings which was also attributed to the interaction of the bottom rotor with the tip vortex and wake from the top rotor. Shukla and Komerath [32] have experimentally investigated the low Reynolds number coaxial rotor flow field including aerodynamic interactions and their effect on the performance. They used high-speed stereo particle image velocimetry (SPIV) to capture the evolution of the wake. Through this, they found that the wake from the upstream propeller impinges on the downstream propeller.

A recent study by McKay et al. [33] experimentally investigated the noise produced by a contra-rotating UAV rotor system and presented a simple theoretical model for predicting the radiated acoustic pressure (based on previous work by Hanson [8]) which was used to interpret the results obtained from their experiments. It was observed that the amplitude of the interaction tones generally decreased when the spacing between the rotors increased – although the rate of decay was dependent on frequency. The far-field acoustic pressure measured at a position on the axis of rotation of the rotors was used to estimate the total unsteady loading on the rotor blades, the magnitude of which was also observed to generally decrease with increasing rotor spacing. Although the exact causes of this unsteady loading were not investigated in detail, they suggested that the rapid decay of the unsteady loading and tone amplitudes with increasing rotor spacing indicated that the unsteady loading was primarily caused by bound potential field interactions. Chaitanya et al. [34] conducted a study investigating the effect of rotor separation distance on the noise produced by a contra-rotating rotor system. Similar to McKay et al. [33] they found that interaction tones dominated the noise spectrum. Additionally, they showed that the bound potential field interactions are the dominant source of tonal noise when the axial gap between the contra-rotating rotors was small. At much larger spacings, the interaction of the tip vortex and wake with the lower rotor becomes the dominant source of tonal noise. Torija et al.[35] made use of the same experimental data set as that reported in Chaitanya et al. [34] to investigate the variation in various psychoacoustic metrics with rotor spacing. Zhong et al. [36] presented a noise prediction method for contra-rotating UAV rotors. The steady aerodynamics of both rotors was calculated using a blade element and momentum theory approach and this was used as input to an analytical method for calculating the unsteady loading on the rotor blades due to their interaction with the bound potential field produced by the adjacent rotor. This analytical method modelled the bound potential field of each rotor at a given radius using a series of point vortices. A time-domain method was then used to calculate the radiated acoustic pressure. The model produced predictions which compared well with experimental measurements.

1.2.5 Experimental methods

In this section, references which report experimental measurements of the noise from UAV propellers are reviewed. There are three different methods which researchers have used to measure the noise of UAVs: outdoor flight testing, testing the UAV in an anechoic chamber, and testing a single propeller in an anechoic chamber.

Outdoor flight testing of UAV noise has been reported in Cabell et al. [37], Kloet et al. [38] and Hioka et al. [39]. Flight testing outdoors allowed these researchers to measure the sound level emitted by a UAV in operation. Although these studies all used test locations which were well away from residential areas to avoid any disturbances to noise measurements, they found that not all flights produced quality acoustic data [37,38]. Kloet et al. [38] encountered high background noise levels from wildlife (birds made noise with peak levels of approximately 80 dBA) whereas Cabell et al. [37] found that repeatability was an issue due to unsteadiness and errors in the flight path of the UAV (which were operated by a human pilot).

A number of researchers have measured the noise from UAVs either flying in an anechoic chamber or mounted on a pole with multiple rotors operating in an anechoic chamber. Such studies are reported in Intaratep et al. [40], Lu et al. [41], Feight [42] and Tinney et al. [43]. The common motivation of these studies was to investigate the effect of multi-rotor interactions and the relationship between the number of rotors and the noise which was produced. These studies did not solely focus on the fundamental noise sources but rather investigated the characteristics of the overall noise produced from multirotor UAVs and aerodynamic parameters such as thrust. Intaratep et al. [40] observed that as the number of propellers operating at once doubled, the sound pressure level at most observer locations increased more than 3 dB. This non-linear increase suggested that the interactions between the propellers must have been significant.

Researchers have also measured noise from a single UAV propeller mounted in an anechoic chamber. These investigations provide detailed measurements of the noise produced by UAV propellers operating in a hover condition. Zawodny et al. [1], Vieira et al. [44], Stephenson et al. [45], and McKay et al. [46] all present such measurements. Vieira et al. [44] notes that noise from the electric motors which drive their propellers can be dominant at high frequencies. This was also observed by McKay et al. [46]. In order to reduce the noise produced by the electric motor in their tests, McKay et al. enclosed the electric motor in a thick steel enclosure. They verified that the enclosure reduced the electric motor noise to at least 10 dB lower than the propeller noise at most frequencies by measuring the vibration of the enclosure using a laser Doppler vibrometer and then calculating the sound radiation using the boundary element method [47]. Stephenson et al. [45] identified that recirculation effects could produce turbulent inflow noise which could significantly enhance the amplitude of the tones which occur at the harmonics of the blade passing frequency (BPF). These tones increase in level a short time after the propeller is started – which is attributed to the recirculation effect becoming established. McKay et al. [48] conducted similar measurements of the noise produced by a UAV propeller in an anechoic chamber. However, they found that the level of the tones did not significantly change with time. They instead suggested that the high frequency tones could have been produced by the unsteady rotational motion of the propellers driven by the electric motor. Whelchel et al. [49] conducted an experimental study of four commercially available UAV propellers in an anechoic chamber and outdoors in order to assess the recirculation effect. They found that the level of the BPF tones increased slightly with time during testing in the anechoic chamber. However, these tones were still present during testing outdoors and the level of these tones was relatively constant with time. Thus, the cause of these tones which occur at harmonics of the BPF is still unknown, but (given that the level of the tones appears to be affected by recirculation within the anechoic chamber) they are likely to be caused by turbulent inflow onto the propellers. To mitigate recirculation effects within an anechoic chamber, Whelchel et al. [49] investigated the use of upstream turbulence screens. However, the results of these tests were inconclusive. Whelchel et al. [49] showed that there was good agreement between the polar directivity of the overall sound pressure level (OASPL) and sound pressure level (SPL) of the first two blade passing frequency harmonics measured in the indoor and outdoor experiments.

1.2.6 Numerical methods

Glegg et al. [50] states that loading noise can be predicted using an acoustic analogy method with loading on the source integration surface calculated using incompressible CFD simulations, provided that the acoustic wavelength is much larger than the characteristic dimension of the surface. The UAV propellers considered in this thesis have chord-lengths which are typically not larger than 4 cm. Therefore, it should be fine to use data from incompressible CFD simulations to predict aeroacoustic noise at frequencies much lower than 8500 Hz at standard atmospheric conditions. In this project, the frequency range of interest is only up to approximately 2500 Hz (approximately 25 times the BPF of the propeller). This suggests that incompressible CFD combined with an acoustic analogy method is appropriate for modelling the noise produced by UAV propellers.

However, one of the challenges of using CFD to predict the aerodynamics and sound produced by a UAV propeller is related to the capability of predicting the correct transitional turbulent flow behaviour within the boundary layer on the propeller surface. Compared to large horizontal axis propellers, UAV propellers operate at a low Reynolds number, typically less that 10^5 (based on the chord length and local flow speed relative to the blade). In this flow regime, the boundary layer may transition from laminar to turbulent and capturing this behaviour is challenging.

Casalino et al. [51] proposed a benchmark case for low Reynolds number propeller aeroacoustics. They conducted experiments and numerical simulations of low Reynolds number propellers. The rotational tip Mach number was 0.139 and the Reynolds number based on the rotational velocity and the blade chord at 85% of blade tip radius was about 50,000 for the case they investigated. The numerical model predicted transition on the suction side of the propeller blades and not on the pressure side.

There are a number of methods available for calculating the flow around an aerofoil at low Reynolds numbers (and particularly the boundary layer flow). For example, Castelli et al. [52] undertook a numerical investigation of the flow over a NACA 0012 aerofoil at a Reynolds number of 360,000 using Ansys Fluent. Their simulations showed laminar to turbulent transition in the aerofoil boundary layer and their predictions showed good agreement with predictions made using XFOIL. Transition was predicted using the Gamma-theta model [53,54] implemented in FLUENT. This model has been validated for a significant number of test cases for turbomachinery and aerodynamic applications including transition on an aerofoil. Castelli et al. [52] found that the gamma-theta model predicted transition on the suction side of the aerofoil slightly downstream of the location predicted using XFOIL for low angles of attack.

In addition to using an appropriate transition model, to correctly model the flow within the boundary layer, great care needs to be taken to use an appropriately sized mesh. One effective method of doing this for propeller simulations is to utilize an overset/chimera mesh. An overset mesh typically contains the body of interest such as a propeller blade which is superimposed on a background mesh containing the surrounding geometry. A mapping between both meshes is used to generate a composite domain on which the flow is solved. The overset method makes it easy to model objects in relative motion and simplifies the generation of the mesh [55]. Structured meshes are often used for the background mesh which leads to simulations which require less computational cost.

Diaz et al. [56] conducted a high-fidelity simulation of a multi-rotor UAV using a CFD method which employed the overset mesh method. The rotor blade geometry was a T-Motor P15x5 CF blade which is the same used for many of the simulations and experiments reported in this thesis. The overset grid around the propeller blades allows a high-resolution mesh close to the blades with appropriate resolution in the chord-wise direction near the aerofoil's leading and trailing edges and with the first node point adjacent to the blade surfaces having a y+ value of less than one. Lakshiminarayan et al. [57] also used this technique in their simulations of micro-scale coaxial rotors.

Their CFD simulations utilised two overset meshes for the rotors (one for each rotor), two nested contra-rotating background meshes, and two cylindrical outer background meshes.

Chan et al. [58] describe a process for ensuring best practice when using an overset method. Mesh generation can be divided into four main steps: geometry processing, surface-grid generation, volume-grid generation, and domain connectivity. They emphasize the significance of geometry processing. Minor geometric flaws may cause local pressure variations but may not affect integrated forces and moments. Major flaws which include missing geometric features can produce incorrect solutions and have serious problems if they are not detected.

A comparative study has been conducted for different overset grid solvers between Openfoam, Star-CCM+ Ansys-Fluent by Chandar et al. [55]. Results are presented for steady and unsteady flows in 2D and 3D. It was found that all codes were in reasonable agreement for most problems but failed to produce identical results in certain situations – especially for unsteady flows. It is believed that these differences were due to the different interpolation methods used in the various algorithms.

1.2.7 Summary

There has been relatively little research investigating the aeroacoustic noise produced by contra-rotating UAV propellers. However, there is a wide body of literature relating to the aeroacoustics of helicopter and aircraft contra-rotating rotors/propellers which provides insight into the possible noise generation mechanisms and methods for exploring these. This thesis will focus on exploring the physical mechanisms by which the interaction tones produced by these systems are generated. These interaction tones are caused by unsteady loading on the rotor blades due to their interaction with the unsteady periodic flow from the adjacent rotor. The unsteady flow incident on the top rotor is produced by the bound potential field of the bottom rotor, whilst the unsteady flow incident on the bottom rotor can be thought of as consisting of the sum of a bound potential field, tip vortex and viscous wake from the top rotor.

Many of the studies investigating the noise from contra-rotating helicopter rotors were numerical. These employed CFD methods to predict the unsteady blade loads and visualise the flow and FW-H solvers were used to predict the radiated noise. Studies investigating the noise produced by contra-rotating open rotors and contra-rotating UAV rotors used analytical, experimental, and computational methods. Several of the studies of contra-rotating helicopter rotor systems showed that the interaction of the tip vortex from the top rotor with the bottom rotor was an important source of noise for those cases. This was also shown to be important for contra-rotating UAV rotor systems when the spacing between the rotors was large. For contra-rotating rotor systems with a small spacing between the rotors (both UAVs and large open rotors), the bound potential field interactions were shown to be dominant sources of noise. The interaction of the viscous wake from the front rotor with the rear rotor was also shown to be the dominant noise source for contra-rotating open rotors with relatively large spacings between the rotors.

A number of experiments have been conducted in which the noise produced by UAV propellers has been measured in an anechoic chamber. Recirculation in the chamber may cause enhancement of the BPF harmonic tones which these propellers produce. However, this thesis will focus on the interaction tones produced by contra-rotating rotor systems which occur at frequencies corresponding to the sum of integer multiples of the BPFs of each rotor. These tones are also expected to dominate the noise spectrum. Thus, experimental testing of contra-rotating UAV rotor systems in an anechoic chamber is an appropriate method for measuring the noise produced by these systems.

The literature shows that incompressible CFD can be used to accurately model the noise generated by UAV propellers. However, modelling the flow over a low Reynolds number propeller is difficult – with these difficulties related to the ability of the CFD solver to accurately capture the transitional flow within the boundary layers on the rotor blades. Therefore, an appropriate turbulence model and

mesh technique must be used. This literature review has identified that the gamma-theta turbulence model and the overset grid technique are appropriate methods for simulating a contra-rotating UAV rotor system.

1.3 Objectives

The general aims of this thesis are to further the understanding of the physical causes of the interaction tones produced by a contra-rotating UAV rotor system and to use this understanding to reduce the level of these tones. The objectives outlined below contribute towards these goals.

1. Identify the physical mechanisms that generate these interaction tones.

The interaction tones produced by a contra-rotating UAV rotor system are caused by the periodic unsteady loading on the blades. Several studies have identified that the bound potential field interactions and tip vortex interactions are important causes of this loading. The importance of these sources for the rotor systems investigated in this work needs to be established.

2. Develop prediction methods for the interaction tones produced by a contra-rotating UAV rotor system.

This objective first requires the unsteady loading on the blades of a contra-rotating UAV rotor system to be accurately calculated. This is done using computational fluid dynamics simulations and analytical modelling. Both frequency- and time-domain acoustic analogy methods are used to calculate the radiated acoustic field.

3. Explore the use of curved blades to reduce the level of the interaction tones produced by a contra-rotating UAV rotor system.

A number of theoretical studies have shown that blade sweep can be used to reduce the interaction tones produced by a contra-rotating open rotor. In principle, this technique can also be applied to reduce the level of the interaction tones produced by a contra-rotating UAV rotor system. This work will explore the effect of curving, or "skewing", the blades of a contra-rotating UAV rotor system for this purpose. This investigation uses numerical and experimental methods to assess the noise produced by rotor systems with different skewed blades and explores the physical mechanism which produces the noise reduction.

4. Investigate the effect of cropping the lower rotor on the interaction tones produced by a contra-rotating UAV rotor system.

Cropping the downstream propeller of a contra-rotating open rotor system has been shown to reduce the interaction tones produced by tip vortex interactions for that propulsor. The effectiveness of this technique is explored for contra-rotating UAV rotor systems using experimental and numerical methods.

5. Investigate the effect of changing the pitch angle of the bottom rotor on the interaction tones produced by a contra-rotating UAV rotor system.

Bound potential field interactions are a significant contributor to the interaction tones produced by a contra-rotating UAV rotor system. This bound potential field is primarily caused by the loading on the rotor blades – which can be altered by changing the pitch angle of the rotor blades. The effect of varying the pitch angle of the bottom rotor blades on the interaction tones produced by a contra-rotating UAV rotor system is explored using experimental and numerical methods.

1.4 Thesis outline

This thesis comprises five chapters. A brief outline of each chapter is given below.

Chapter 2 describes the steps used to develop a validated 3D CFD model of a contra-rotating UAV rotor system and presents results generated using this method. A semi-analytical model for predicting the loading on the blades of a rotor system due to the bound potential field interactions is also presented. A novel frequency-domain acoustic analogy method is used to make noise predictions using the loading predicted by the CFD simulations and semi-analytical model. The frequency domain method is validated against a time-domain acoustic analogy method. The predicted sound pressure levels of the prominent interaction tones are compared with experimental data for a number of different cases and at different observer positions. The effect of rotor-rotor spacing is also explored.

Chapter 3 explores the effect of blade skew on the noise produced by a contra-rotating UAV rotor system. It uses the methods presented in chapter 2 to predict the interaction tones produced by rotor systems with differently skewed blades and validates these predictions by comparison with experimental measurements. It is shown that blade skew can be used to significantly reduce the level of the interaction tones with little to no reduction in the aerodynamic performance.

Chapter 4 discusses the effect of blade skew and cropping on the sound pressure level of the prominent interaction tones produced by a contra-rotating UAV rotor system. This chapter also uses the prediction and experimental methods presented in chapter 2 to calculate the radiated noise levels. Some rotor systems with the cropped bottom rotors produce interaction tones with generally lower levels which is shown to be due to the reduction of the tip vortex interaction effect. In addition, this chapter explores the effect of changing the pitch angle of the lower rotor blades on the sound pressure level of prominent interaction tones. The pitch angle and the rotational speed of the top rotor was kept constant while these parameters for the bottom rotor were varied such that the total thrust was kept constant. This work was experimental and numerical.

Chapter 5 presents the conclusions and describes recommended future work.

2. Interaction tone noise prediction, measurement, and analysis

This chapter describes an investigation of the interaction tones produced by two different contra-rotating UAV rotor systems operating in a hover condition (i.e. there is no airflow through the rotor systems other than that induced by the rotors). The first system is that considered by McKay et al. [33]. This rotor system consisted of two 15" diameter '15×5' carbon fibre T-motor propellers mounted in a contra-rotating configuration as shown in Fig. 1. For this system, the top rotor rotated at 580 rad/s whilst the bottom rotor rotated in the opposite direction at 440 rad/s. Tests and CFD simulations were conducted for this system with the rotors separated by 40 mm and 60 mm in the axial direction. The second system consisted of two custom-made aluminium hubs with 15" diameter carbon fibre rotors as shown in Fig. 2. The rotors used in the second setup were custom designed and have a constant pitch angle of 8 degrees and chord length of 26.6 mm. The section profile was constant along the blade span with the point of maximum camber located 3.76% of the chord-length at 55% of the chord-length from the leading edge. The maximum thickness was 7.33% of the chord-length. For this system, the top rotor rotated at 500 rad/s and the bottom rotor rotated at the same speed in the opposite direction. These rotors were separated by 40 mm in the axial direction.

Computational Fluid Dynamics (CFD) simulations were used to calculate the periodic unsteady loading on the blades of the rotors and the methods used to produce these simulations are described in section 2.1.1. Semi-analytical methods for predicting the periodic unsteady loading on the rotor blades due to the bound potential field of the adjacent rotor are presented section 2.1.2. These methods are compared with the loading calculated from the CFD simulations in section 2.2 and the primary causes of the unsteady loading are identified. The method for experimentally measuring the noise and thrust produced by the rotor systems is described in section 2.3. A frequency-domain method for calculating the interaction tones radiated from the rotor system is presented in section 2.4. This method is then applied to predict the noise radiated from the two contra-rotating UAV rotor systems using the blade loading calculated from the CFD simulations and the semi-analytical models in section 2.5. These predictions are compared with experimental measurements showing good agreement. The effect of rotor spacing on the amplitude of the interaction tones is also explored. The conclusions of this chapter are presented in section 2.6.

Fig. 1 Photograph of the first contra-rotating UAV rotor system mounted in the anechoic chamber.
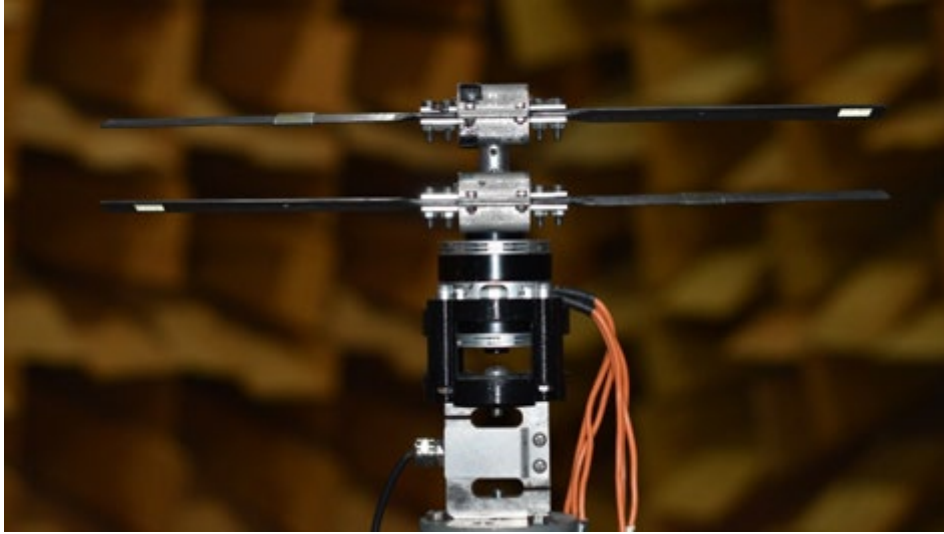
Fig. 2 Photograph of the second contra-rotating UAV rotor system mounted in the anechoic chamber.

2.1 Unsteady loading prediction

In the aerodynamic analysis which follows it will be convenient to introduce a cylindrical coordinate system with its origin at the centre of the top rotor as shown in Fig. 3. The coordinate system has axial coordinate x, with positive x upwards, radial coordinate r and azimuthal angle ϕ. The hub of the top rotor is located in the $x = 0$ plane and the mid-chord of the reference blade on the top rotor is located at $x = x_{c1}(r)$ and $\phi = \phi_{01}(r)$ at time $t = 0$. The top rotor has B_1 blades and rotates at speed Ω_1 rad/s in the negative ϕ direction. The mid-chord of the reference blade of the bottom rotor is located at $x = x_{c2}(r)$ and $\phi = \phi_{02}(r)$ at time $t = 0$. The bottom rotor has B_2 blades and rotates at speed Ω_2 rad/s in the positive ϕ direction. This naming convention is used throughout the thesis where other quantities associated with the top rotor are denoted by a subscript 1, whereas quantities associated with the bottom rotor are denoted by a subscript 2. The tip of both rotors is located at radius $r = r_t$.
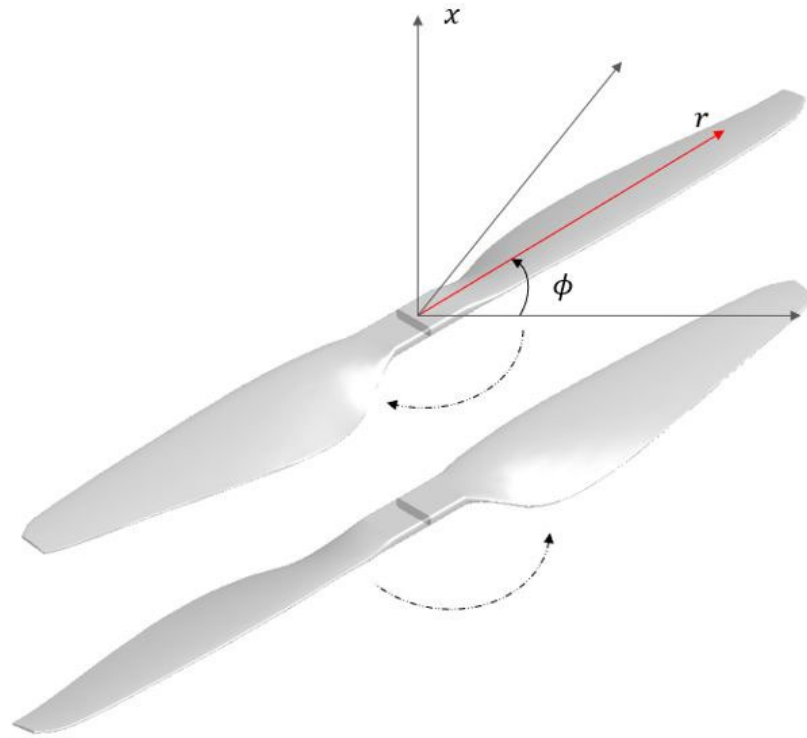
Fig. 3 Schematic showing the direction of rotation of both rotors and the cylindrical coordinate system utilised in this chapter.

CFD simulations of the contra-rotating UAV rotor systems were undertaken in order to accurately calculate the periodic unsteady forces acting on the rotor blades during operation. For the first rotor system, two cases were simulated: one with the rotor hubs separated by 40 mm in the axial direction, and the other with the hubs separated by 60 mm. This section presents a detailed analysis of the flow and loading calculated from the simulation with the hubs separated by 40 mm. CFD simulations were also conducted of the second rotor system with the custom-built blades.

2.1.1 Numerical simulation method and data processing
The simulations did not include the geometry of the electric motor or shafts which drove the rotors. This is warranted here as these features have little effect on the flow through the rotor system – particularly the periodic loading on the outer sections of the rotor blades – which is primarily responsible for producing the interaction tones. The simulations utilised the overset mesh method [59] in which a region around the complex geometry of the rotor blades is meshed using a hexacore mesh which is then surrounded by a structured background mesh. The component mesh surrounding each rotor occupied a cuboid shaped region and the mesh was refined such that the y^+ values of the closest mesh nodes to the blade surfaces was less than one. Each component mesh was superimposed onto a cylinder-shaped background mesh which rotated with the component mesh, and which had a diameter which was slightly larger than the rotor diameter. The rotating domain surrounding each rotor comprised a component mesh and a background mesh. The top and bottom rotating domains were separated by a sliding mesh interface. The rotating domains were enclosed within a cylinder-shaped static domain and the static and rotating domains were separated by a sliding mesh interface. The static domain had a diameter and height equal to two and three times the diameter of the rotors, respectively. The top and side surfaces of the static domain were set as a pressure inlet, whilst the bottom surface was set as pressure outlets.

The simulations were conducted using Ansys Fluent and solved the incompressible, unsteady Reynolds-averaged Navier Stokes (URANS) equations utilising the k-ω SST turbulence model. The pressure-based solver was used with the semi-implicit method for pressure-linked equations (SIMPLE) algorithm [59]. The transient simulation was initialized using the solution obtained from a steady calculation which used the multiple reference frame model. The time-step size in the transient simulation was set so that the top rotor rotated 1° per time step. The transient simulation was run until the total force acting on both rotors was observed to be periodic. The CFD simulations were run on 36 CPUs and each simulation took approximately 30 hours to simulate three full revolutions of the top rotor.

Fig. 4 presents a visualisation of the flow calculated for the first contra-rotating rotor system with a 40 mm gap between the rotors. This image plots isosurfaces of constant λ_2 criterion coloured by vorticity magnitude and clearly shows the tip vortices shed from the rotor tips. Note that these vortices convect downstream in a helical shape with a small pitch and migrate radially inwards due to the streamtube contraction through the rotor system.
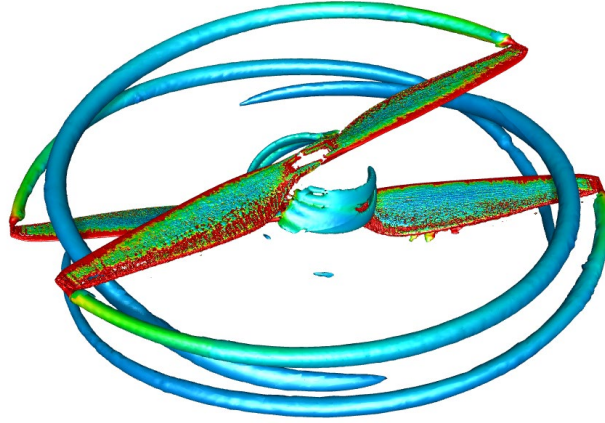
Fig. 4 Isosurfaces of constant λ_2 criterion coloured by vorticity magnitude calculated from the CFD simulation of the rotor system with a 40 mm gap between the rotors.

The periodic unsteady loading on the downstream rotor blades is produced by the interaction of these blades with the bound potential field, viscous wakes and tip vortices shed from the top rotor. In order to visualise these sources, the fluid velocity on a disc which lay midway between the rotors was extracted from the CFD simulation of the first rotor system with the rotors separated by 40 mm over a period corresponding to one revolution of the bottom rotor. The effect of the bound potential field of the bottom rotor was removed from the simulations using the technique described by Carazo et al. [60] in which the velocity field is time-averaged in a frame of reference moving with the top rotor. i.e. the time-average axial velocity in a frame of reference rotating with the top rotor is given by

$$\bar{u}_x(r, \phi_1) = \frac{1}{T} \int_0^T u_x(r, \phi_1, t)\mathrm{d}t, \tag{1}$$

where $\phi_1 = \phi + \Omega_1 t$ is the azimuthal angle rotating with the top rotor and $T = 2\pi/B_2(\Omega_1 + \Omega_2)$ is the time taken for one passage of the bottom rotor in the rotating frame of reference. The function

$u_x(r, \phi_1, t)$ was calculated from the discrete CFD data using Matlab's interpolation routines. A similar expression was used to deduce the average tangential velocity in a frame of reference rotating with the top rotor, $\bar{u}_\phi(r, \phi_1)$.

The time-average axial velocity perturbation in a frame of reference rotating with the top rotor was then calculated as

$$\bar{u}_x'(r, \phi_1) = \bar{u}_x(r, \phi_1) - U_x(r), \tag{2}$$

where

$$U_x(r) = \frac{1}{2\pi} \int_0^{2\pi} \bar{u}_x(r, \phi_1) \mathrm{d}\phi_1, \tag{3}$$

is the time- and azimuthal-average mean-flow velocity in the axial direction. Equivalent expressions were used to deduce values for $\bar{u}_\phi'(r, \phi_1)$ (the time-average tangential velocity perturbation in a frame of reference rotating with the top rotor) and $U_\phi(r)$ (the time- and azimuthal-average mean-flow velocity in the tangential direction).

Fig. 5 plots contours of $\bar{u}_\phi'$ and $\bar{u}_x'$ on the extraction plane calculated from the CFD data using these methods. These results show that the tip vortex produces a strong velocity perturbation in the axial direction which is evident as the intense blue and yellow spirals close to the blade tip radius. The tip vortex produces only a relatively minor tangential velocity perturbation. This is expected for a tip vortex with a small pitch which is the case here. Conversely, the viscous wakes produce a relatively strong tangential velocity perturbation but a relatively weak perturbation in the axial direction. This is likely due to the low mean velocity through the rotor system in the axial direction which produces a wake deficit velocity aligned more closely to the tangential direction than the axial direction. The bound potential field from the top rotor produces a relatively strong velocity perturbation in both the axial and tangential directions at azimuthal angles close to the location of the top rotor blades.

16
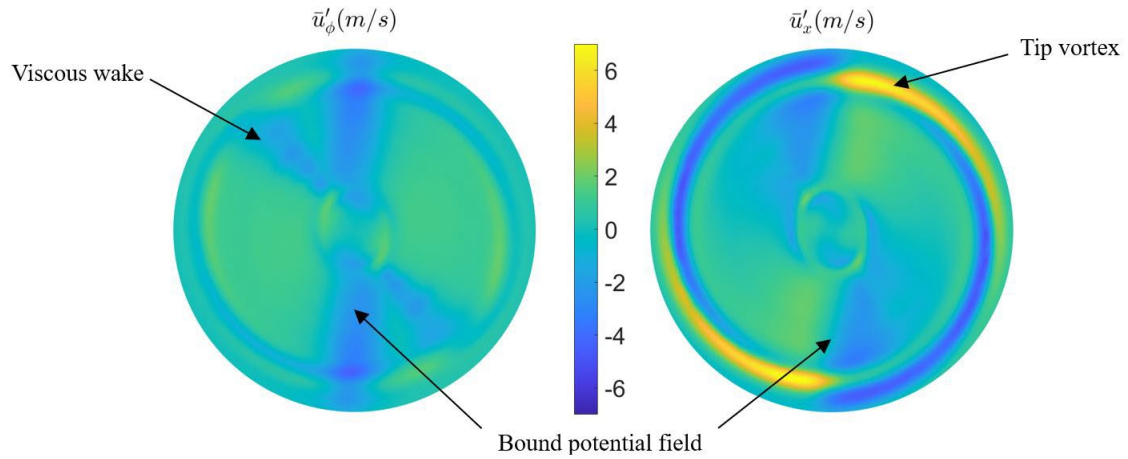
Fig. 5 Contours of $\bar{u}'_\phi$ (left) and $\bar{u}'_x$ (right) on a disc mid-way between the two rotors calculated from the CFD simulation. The disc diameter is equal to the rotor diameter.

2.1.2 Semi-analytical prediction method

In this section, semi-analytical models for predicting the unsteady loading on the top and bottom rotor blades due to their interaction with the bound potential field of the adjacent rotor are presented. The purpose of this modelling work is to deduce the contribution of the bound potential field interaction source to the periodic unsteady loading on the rotor blades and thus the interaction tones produced by the contra-rotating rotor system.

2.1.2.1 Bound potential field due to blade loading

The bound potential field model relies on the assumption that the aerodynamic interaction between two blades at a given radius r is well approximated by an equivalent 'unwrapped' two-dimensional problem in which two cascades of aerofoils immersed in a uniform flow translate past each other. The situation is shown in Fig. 6. The top aerofoils have a section profile identical to that of the blades on the top rotor at that radius whilst the bottom aerofoils have a section profile identical to that of blades on the bottom rotor at the same radius. The horizontal ξ-axis corresponds to the circumferential direction $(r\phi)$ whilst the vertical η-axis corresponds to the rotor (x) axis.

The top cascade translates in the negative ξ-direction at velocity $\Omega_1 r$, whilst the bottom cascade translates in the positive ξ-direction at velocity $\Omega_2 r$. The free-stream velocity is in the negative η-direction and has magnitude V which was estimated from the CFD simulations.
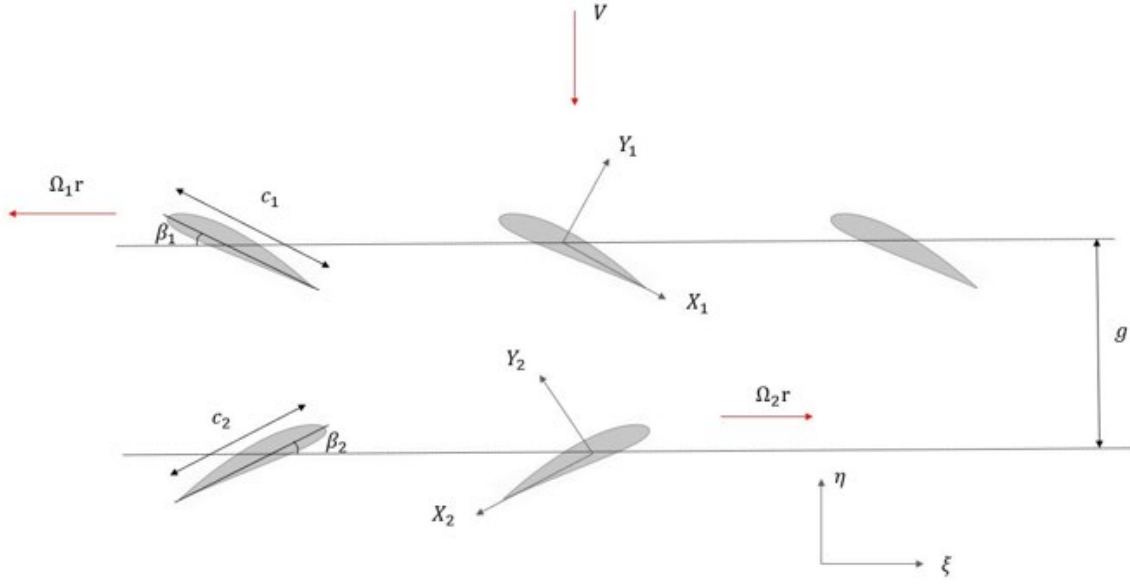
Fig. 6 Equivalent two-dimensional problem used to model the bound potential field interaction at a given radius.

The bound potential field produced by the lift forces exerted by each aerofoil on the surrounding air is modelled using thin aerofoil theory [61] in which a vortex sheet is distributed along the aerofoil chord-line. This requires the introduction of a chord-wise/chord-normal coordinate system, which for the reference blade of the top cascade is related to the global coordinates by

$$(\xi - \xi_{c1}) = X_1 \cos \beta_1 + Y_1 \sin \beta_1, \qquad (\eta - \eta_{c1}) = -X_1 \sin \beta_1 + Y_1 \cos \beta_1, \qquad \text{(4 a, b)}$$

where ξ_{c1} and η_{c1} are the ξ- and η- coordinates of the mid-chord of the top reference blade and β_1 is the pitch angle of the top blades, which is taken to be aligned with the local mean-flow i.e. $\tan(\beta_1) = \frac{V}{\Omega_1 r}$. The corresponding expressions for the reference blade on the bottom cascade are

$$(\xi - \xi_{c2}) = -X_2 \cos \beta_2 - Y_2 \sin \beta_2, \qquad (\eta - \eta_{c2}) = -X_2 \sin \beta_2 + Y_2 \cos \beta_2, \qquad \text{(5 a, b)}$$

where, similar to the assumption made for the top blades, $\tan(\beta_2) = \frac{V}{\Omega_2 r}$.

The mid-chord of the top reference blade is located at

$$\xi = \xi_{c1} = -\Omega_1 rt + \xi_{01}, \qquad \eta = \eta_{c1}, \qquad \text{(6)}$$

where $\xi_{01} = r\phi_{01}$ and $\eta_{c1} = x_{c1}$, whilst the mid-chord of the bottom reference blade is located at

$$\xi = \xi_{c2} = \Omega_2 rt + \xi_{02}, \qquad \eta = \eta_{c2}, \qquad \text{(7)}$$

where $\xi_{02} = r\phi_{02}$ and $\eta_{c2} = x_{c2}$. The separation between the mid-chord positions in the η-direction is denoted g i.e. $g = \eta_{c1} - \eta_{c2}$ and corresponds to the axial separation between the mid-chord positions of the top and bottom rotor reference blades at radius r i.e. $g = x_{c1} - x_{c2}$.

Parry [62] considers the potential field produced by an array of equally-spaced line vortices. These vortices each have circulation Γ (positive in the anti-clockwise direction) and are separated by a distance s in the ξ-direction with the nth ($n \in \mathbb{Z}$) vortex located at $\xi = \xi_s + ns$ and $\eta = \eta_s$, where ξ_s

and η_s are the ξ and η locations of the $n = 0$ vortex. Eq. 6.3.4 in [62] can be used to deduce the following expression for the stream-function for such a flow which takes the form

$$\psi = \sum_{n=-\infty}^{\infty} \psi_n, \tag{8}$$

where, for $n > 0$,

$$\psi_n = \frac{\Gamma}{4\pi n} \exp\left\{-i\frac{2\pi n}{s}(\xi - \xi_s) - \frac{2\pi n}{s}|\eta - \eta_s|\right\}. \tag{9}$$

Note that $\psi_{-n} = \psi_n^*$. An expression for ψ_0 can also be deduced from the expressions given in [62], however, this term is not required for the analysis which is presented here.

Thus, the stream-function produced by a cascade of vortex sheets of strength $\gamma(X_2)$ distributed along the chord-lines of the lower cascade blades is given by Eq. (8) with Eq. (9) modified by setting $s = \frac{2\pi r}{B_2}$, replacing Γ by $\gamma(X_2)$ and then integrating the resulting expression along the blade chord-line such that Eq. (9) becomes

$$\psi_n = \frac{1}{4\pi n} \int_{-\frac{c_2}{2}}^{\frac{c_2}{2}} \gamma(X_2) \exp\left\{-i\frac{nB_2}{r}(\xi - \xi_s) - \frac{nB_2}{r}|\eta - \eta_s|\right\} dX_2, \tag{10}$$

where Eqs. (5) and (7) can be used to deduce that $\xi_s = \Omega_2 rt + \xi_{02} - X_2 \cos\beta_2$ and $\eta_s = \eta_{c2} - X_2 \sin\beta_2$ and $c_1(r)$ and $c_2(r)$ are the chord-lengths of the top and bottom aerofoils.

The upwash velocity incident on the chordlines of the blades on the top cascade is given by

$$v_{L,1} = \sin\beta_1 \frac{\partial\psi}{\partial\eta} - \cos\beta_1 \frac{\partial\psi}{\partial\xi}. \tag{11}$$

Thus, the upwash velocity is given by

$$v_{L,1} = \sum_{n=-\infty}^{\infty} v_{L,1,n}, \tag{12}$$

where each term in the series has the form of a harmonic velocity perturbation

$$v_{L,1,n} = \hat{v}_{L,1,n} \exp\{i\omega_{n,1}t - i\bar{\mu}_1\bar{X}_1\}, \tag{13}$$

where, for $n > 0$,

$$\hat{v}_{L,1,n} = \frac{i}{4\pi} \frac{c_2}{2} \frac{B_2}{r} \exp\left\{i\beta_1 + inB_2(\phi_{02} - \phi_{01}) - \frac{nB_2}{r}g\right\} \int_{-1}^{1} \gamma_2(X_2) \exp\{-i\bar{\mu}_2\bar{X}_2\} d\bar{X}_2, \tag{14}$$

is the harmonic velocity perturbation amplitude,

$$\bar{\mu}_1 = \frac{nB_2}{r} e^{i\beta_1} \frac{c_1}{2}, \qquad \bar{\mu}_2 = \frac{nB_2}{r} e^{-i\beta_2} \frac{c_2}{2}, \tag{15 a, b}$$

are dimensionless wavenumbers,

$$\omega_{n,1} = nB_2(\Omega_1 + \Omega_2), \tag{16}$$

19

is the frequency of the harmonic velocity perturbation, and $\bar{X}_1 = \frac{2X_1}{c_1}$ and $\bar{X}_2 = \frac{2X_2}{c_2}$ are dimensionless chordwise coordinates.

Any vortex sheet distribution can be used in the method. However, for a thin flat-plate aerofoil,

$$\gamma_2(X_2) = \frac{C_{l,2}}{\pi} U_{r_2} \sqrt{\frac{1 - \bar{X}_2}{1 + \bar{X}_2}}, \tag{17}$$

where $C_{l,2}$ is the section lift coefficient for the bottom aerofoil and $U_{r_2} = \sqrt{(\Omega_2 r)^2 + V^2}$ is the mean flow speed of the bottom aerofoil relative to the air.

Substituting Eq. (17) into Eq. (14) and evaluating the integral (making use of the identity given by Eq. A7.4.3 in [62]) yields

$$\hat{v}_{L,1,n} = \frac{\mathrm{i}}{4\pi} C_{l,2} U_{r_2} \frac{c_2}{2} \frac{B_2}{r} [J_0(\bar{\mu}_2) + \mathrm{i}J_1(\bar{\mu}_2)] \exp\left\{\mathrm{i}\beta_1 + \mathrm{i}nB_2(\phi_{02} - \phi_{01}) - \frac{nB_2}{r}g\right\}. \tag{18}$$

Parry [62] utilised Kemp's incompressible blade response function [63] and showed that the unsteady lift force per unit span acting on a flat-plate aerofoil due to a harmonic velocity perturbation of the form given by Eq. (10) is

$$L_{L,1,n} \exp\{\mathrm{i}\omega_{n,1}t\} = \pi\rho_0 c_1 U_{r_1} \hat{v}_{L,1,n} \exp\{\mathrm{i}\omega_{n,1}t\} \left[C(\sigma_1)[J_0(\bar{\mu}_1) - \mathrm{i}J_1(\bar{\mu}_1)] + \mathrm{i}\frac{\sigma_1}{\bar{\mu}_1}J_1(\bar{\mu}_1)\right], \tag{19}$$

where $U_{r_1} = \sqrt{(\Omega_1 r)^2 + V^2}$ is the speed of the top aerofoils relative to the mean-flow,

$$C(\sigma_1) = \frac{H_1^{(2)}(\sigma_1)}{H_1^{(2)}(\sigma_1) + \mathrm{i}H_0^{(2)}(\sigma_1)}, \tag{20}$$

is the Theodorsen function, and $\sigma_1 = \frac{\omega_n c_1}{2U_{r_1}}$ is the reduced frequency.

Parry [62] suggests that the incompressible blade response function is accurate when $\frac{\sigma_1 M_{r_1}}{(1 - M_{r_1})} < 1$. For the cases considered in this chapter this is valid for $n < 10$ at $r = 0.7R_t$.

The same procedure can be used to derive the following expression for the unsteady lift on the reference blade of the bottom cascade due to its interaction with the potential field produced by the lift force acting on the aerofoils in the top cascade. The expression for a single harmonic is given by

$$L_{L,2,n} \exp\{\mathrm{i}\omega_{n,2}t\} = \pi\rho_0 c_2 U_{r_2} \hat{v}_{L,2,n} \exp\{\mathrm{i}\omega_{n,2}t\} \left[C(\sigma_2)[J_0(\bar{\bar{\mu}}_2) - \mathrm{i}J_1(\bar{\bar{\mu}}_2)] + \mathrm{i}\frac{\sigma_2}{\bar{\bar{\mu}}_2}J_1(\bar{\bar{\mu}}_2)\right], \tag{21}$$

where $\omega_{n,2} = nB_1(\Omega_1 + \Omega_2)$ is the frequency of the harmonic velocity perturbation, $U_{r_2} = \sqrt{(\Omega_2 r)^2 + V^2}$ is the speed of the bottom aerofoils relative to the mean-flow, $\hat{v}_{L,2,n}$ is the amplitude of the harmonic velocity perturbation which for $n > 0$ is given by

$$\hat{v}_{L,2,n} = \frac{\mathrm{i}}{4\pi} \frac{c_1}{2} \frac{B_1}{r} C_{l,1} U_{r_1} \exp\left\{-\mathrm{i}\beta_2 + \mathrm{i}nB_1(\phi_{02} - \phi_{01}) - \frac{nB_1}{r}g\right\} [J_0(\bar{\mu}_1) + \mathrm{i}J_1(\bar{\mu}_1)], \tag{22}$$

$\sigma_2 = \frac{\omega_{n,2} c_2}{2U_{r_2}}$ is the reduced frequency, $C_{l,1}$ is the section lift coefficient of the top aerofoils, and $\bar{\mu}_1$ and $\bar{\bar{\mu}}_2$ are dimensionless wavenumbers which are defined as before but with B_2 replaced by B_1, i.e.

$$\bar{\bar{\mu}}_1 = \frac{nB_1}{r} e^{i\beta_1} \frac{c_1}{2}, \qquad \bar{\bar{\mu}}_2 = \frac{nB_1}{r} e^{-i\beta_2} \frac{c_2}{2}. \tag{23a, b}$$

The method presented in this section is similar to that presented in chapter 6 of Parry [62], except extended to include the effect of the vortex sheet distributed along the blade chord-line (rather than modelling this effect using a single vortex). A similar approach was also adopted by Ekoule et al. [19] who present a method for calculating the unsteady response of a blade of a contra-rotating open rotor which takes into account compressibility effects and distributed sources. Note that for the cases considered in this chapter, this extension produces very similar results to those made using Parry's method.

2.1.2.2 Bound potential field due to blade thickness

Katz and Plotkin ([64], Eq. 5.12) show that the potential field produced by the thickness effect of a thin aerofoil can be represented by a distribution of sources along the chordline of the blade. Utilising their analysis, the velocity potential produced by the thickness effect of the reference blade on the lower cascade is given by

$$\hat{\phi}(\xi, \eta) = \frac{U_{r2}}{\pi} \int_{-\frac{c_2}{2}}^{\frac{c_2}{2}} \tau_2'(X_2) \ln \left[\sqrt{\left(\xi - \xi_s(X_2)\right)^2 + \left(\eta - \eta_s(X_2)\right)^2} \right] dX_2, \tag{24}$$

where $\tau_2(X_2)$ is the thickness distribution of the lower aerofoil (which describes the displacement of the top and bottom surfaces of a blade from its camber-line) and ξ_s and η_s denote the ξ- and η-coordinates of the sources on the blade chord-line – which can be determined using Eqs. (4a-b).

The velocity potential produced by the lower cascade of blades can be determined straightforwardly from Eq. (24) as

$$\phi(x, y) = \sum_{n=-\infty}^{\infty} \hat{\phi}\left(\xi + \frac{2\pi r}{B_2} n, \eta\right). \tag{25}$$

Expressing Eq. (25) as a Fourier series, yields

$$\phi(\xi, \eta) = \sum_{n=-\infty}^{\infty} \phi_n, \tag{26}$$

where, for $n > 0$,

$$\phi_n = -\frac{U_{r_2}}{2\pi n} \int_{-\frac{c_2}{2}}^{\frac{c_2}{2}} \tau_2'(X_2) \exp\left\{-i\frac{nB_2}{r}(\xi - \xi_s) - \frac{nB_2}{r}|\eta - \eta_s|\right\} dX_2. \tag{27}$$

The upwash velocity incident on the upper blades is given by

$$v_{T,1} = \sin\beta_1 \frac{\partial\phi}{\partial\xi} + \cos\beta_1 \frac{\partial\phi}{\partial\eta}. \tag{28}$$

Following the same procedure used in the previous section, the upwash velocity is given by

$$v_{T,1} = \sum_{n=-\infty}^{\infty} v_{T,1,n}, \tag{29}$$

where each term in the series has the form of a harmonic velocity perturbation

$$v_{T,1,n} = \hat{v}_{T,1,n} \exp\{i\omega_{n,1}t - i\bar{\mu}_1\bar{X}_1\}, \tag{30}$$

where, for $n > 0$,

$$\hat{v}_{T,1,n} = \frac{U_{r_2}}{2\pi} \frac{c_2}{2} \frac{B_2}{r} \exp\left\{i\beta_1 + inB_2(\phi_{02} - \phi_{01}) - \frac{nB_2}{r}g\right\} \int_{-1}^{1} \tau_2'(X_2) \exp\{-i\bar{\mu}_2\bar{X}_2\} \, d\bar{X}_2. \tag{31}$$

The unsteady lift response to each harmonic gust is then calculated using the equivalent form of Eq. (19). i.e.

$$L_{T,1,n} \exp\{i\omega_{n,1}t\} = \pi\rho_0 c_1 U_{r_1} \hat{v}_{T,1,n} \exp\{i\omega_{n,1}t\} \left[C(\sigma_1)[J_0(\bar{\mu}_1) - iJ_1(\bar{\mu}_1)] + i\frac{\sigma_1}{\bar{\mu}_1}J_1(\bar{\mu}_1)\right]. \tag{32}$$

Following the same procedure to calculate the loading on the bottom aerofoil yields the following expression which is equivalent to Eq. (21)

$$L_{T,2,n} \exp\{i\omega_{n,2}t\} = \pi\rho_0 c_2 U_{r_2} \hat{v}_{T,2,n} \exp\{i\omega_{n,2}t\} \left[C(\sigma_2)[J_0(\bar{\mu}_2) - iJ_1(\bar{\mu}_2)] + i\frac{\sigma_2}{\bar{\mu}_2}J_1(\bar{\mu}_2)\right], \tag{33}$$

but with

$$\hat{v}_{T,2,n} = -\frac{B_1 U_{r_1}}{2\pi r} \frac{c_1}{2} \exp\left\{-i\beta_2 + inB(\phi_{02} - \phi_{01}) - \frac{nB_1}{r}g\right\} \int_{-1}^{1} \tau_1'(X_1) \exp\{-i\bar{\mu}_1\bar{X}_1\} \, d\bar{X}_1. \tag{34}$$

The method presented in this section is similar to that presented in chapter 6 of Parry [62], except thin aerofoil theory has been used to model the thickness effect of the rotor blades rather than modelling the blades using the potential flow solution for flow over an ellipse. A similar approach was also adopted by Ekoule et al. [19] who present a method for calculating the unsteady response of a blade of a contra-rotating open rotor which takes into account compressibility effects and distributed sources. Note that although the method proposed in this paper for modelling the thickness effect incorporates the exact thickness distribution of the rotor blades (unlike Parry's method which approximates the section profile of the blade as an ellipse), for the cases considered in this paper, the method produces very similar predictions to those made using Parry's method.

2.1.2.3 Calculation of velocity perturbation components
These models are used to make predictions of the axial and tangential velocity perturbations produced by the bound potential field of the top rotor to compare with the velocity perturbations calculated from the CFD simulation results. Recalling that the ξ- and η directions correspond respectively to the tangential and axial directions, the expressions presented above can be used to deduce equations for the axial and tangential velocity perturbations produced by the bound potential field of the top rotor. The axial and tangential velocity perturbations on a plane located at axial position $x = x_m$ are given by

$$\bar{u}'_{x,BP} = \sum_{n=-\infty}^{\infty} [\bar{u}'_{x,L,n} + \bar{u}'_{x,T,n}] \exp\{inB\phi_1\}, \qquad \bar{u}'_{\phi,BP} = \sum_{n=-\infty}^{\infty} [\bar{u}'_{\phi,L,n} + \bar{u}'_{\phi,T,n}] \exp\{inB\phi_1\}, \tag{35a,b}$$

where, for $n > 0$,

$$\bar{u}'_{x,L,n} = \frac{iB_1}{4\pi r} \frac{c_1}{2} C_{l,1} U_{r_1} [J_0(\bar{\mu}_1) + iJ_1(\bar{\mu}_1)] \exp\left\{-inB\phi_{01} - \frac{nB_1}{r}(x_{c1} - x_m)\right\}, \tag{36}$$

$$\bar{u}'_{x,\mathrm{T},n} = -\frac{B_1 U_{r_1}}{2\pi r}\frac{c_1}{2}\int_{-1}^{1}\tau'_1(X_1)\exp\{-i\bar{\mu}_1\bar{X}_1\}\,d\bar{X}_1\exp\left\{-inB\phi_{01}-\frac{nB_1}{r}(x_{c1}-x_m)\right\}, \tag{37}$$

$\bar{u}'_{\phi,\mathrm{L},n} = i\bar{u}'_{x,\mathrm{L},n}$, and $\bar{u}'_{\phi,\mathrm{T},n} = i\bar{u}'_{x,\mathrm{T},n}$.

The lift coefficient distributions along the span of the both rotors were calculated from the time-average loading due to the pressure stress acting on the rotor blades calculated in the CFD simulations.

Fig. 7 below plots the axial and tangential velocity perturbations produced by the bound potential field of the top rotor on a disc located mid-way between the two rotors. This plot is similar to Fig. 6 and comparison between the two figures demonstrates the contribution of the bound potential field to the flow perturbations shown in Fig. 6.
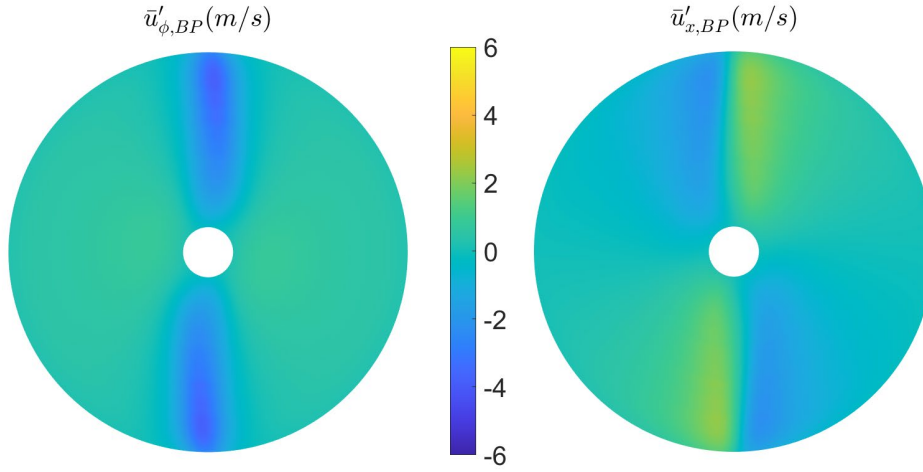
Fig. 7 Contours of $\bar{u}'_{\phi,\mathrm{BP}}$ and $\bar{u}'_{x,\mathrm{BP}}$ on a disc midway between the two rotors calculated using the semi-analytical models for the bound potential field produced by the top rotor. The disc diameter is equal to the rotor diameter.

2.1.2.4 General calculation procedure

The general calculation procedure is shown in Fig. 8. Firstly, the geometry and rotational speeds of the top and bottom rotors are specified. The geometry parameters for each rotor include the number of blades, the tip radius, and the chord-length, thickness, and axial and tangential locations of the mid-chord along the blade radius. The parameters which vary along the blade span are specified at a number of radial stations (e.g. 10). The number of Fourier harmonics used in the analysis is also selected. In the examples considered in this thesis, 10 harmonics is more than sufficient to calculate the significant interaction tones. The next step is to calculate the steady aerodynamic forces acting on the top and bottom propellers (and from those the section lift coefficients) and to estimate the average axial flow velocity through the propeller. In this paper, these are calculated using CFD simulations, however, a lower fidelity method such as the blade element and momentum method could also be used instead. Next the amplitude of the harmonic velocity perturbations incident on the reference blade of each rotor due to the loading on the adjacent rotor are calculated using Eqs. (18) and (21). Note that these expressions assume that the chordwise steady-loading distribution along the blades is equal to that predicted using thin-aerofoil theory for a flat aerofoil. Alternative loading distributions could be calculated for different loading distributions using eq. (14) and an equivalent expression for the bottom rotor. Equivalent calculations are performed to calculate the unsteady loading on the

reference blades of each rotor due to the thickness sources on the adjacent rotor and then the total loading is calculated by summing the contributions due to the loading and thickness sources.

Specify the geometry and rotational speeds of the top and bottom rotors. The blade geometry should be specified at several radial stations along the span. The number of Fourier harmonics to be used in the calculation is set.

Calculate the time-average force-per-unit-span acting and the average axial velocity at each radial station for each rotor.

For each harmonic, at each radial station, calculate the amplitude of the harmonic velocity perturbation due to loading sources ($\hat{v}_{L,1,n}$ and $\hat{v}_{L,2,n}$) using Eqs. (18 or 14) and (22).

For each harmonic, at each radial station, calculate the amplitude of the harmonic velocity perturbation due to thickness sources ($\hat{v}_{T,1,n}$ and $\hat{v}_{T,2,n}$) using Eqs. (31) and (34).

For each harmonic, at each radial station, calculate the amplitude of the unsteady loading on the reference blade due to loading sources using Eqs. (19) and (21).

For each harmonic, at each radial station, calculate the amplitude of the unsteady loading on the reference blade due to thickness sources using Eqs. (32) and (33).

For each harmonic, add the amplitudes of the unsteady loading on the reference blade due to the loading and thickness sources to give total amplitude of the unsteady

Fig. 8 Schematic showing the calculation procedure for determining the semi-analytical models.

2.2 Comparison of the unsteady loading predicted using the CFD and analytical methods

To analyse the unsteady loading on the rotor blades, the reference blade of each rotor of the first rotor system was divided into segments along the blade span and the unsteady force acting on each segment was calculated using data from the CFD simulation of the rotor system with the rotors separated by 40 mm. The average unsteady force per-unit-span was then calculated by dividing this force by the segment length. This can be compared with the force-per-unit-span distribution calculated using the semi-analytical models. The thrust and tangential force-per-unit-span exerted by the top rotor reference blade on the air is calculated as

$$F_x(r,t) = \sum_{n=-\infty}^{\infty} \hat{F}_x^{(n)}(r) \exp\{i\omega_n t\}, \qquad F_\phi(r,t) = \sum_{n=-\infty}^{\infty} \hat{F}_\phi^{(n)}(r) \exp\{i\omega_n t\}, \qquad (38)$$

where $\omega_n = nB_2(\Omega_1 + \Omega_2)$, $\hat{F}_x^{(n)}(r) = -L_{1,n}\cos\beta_1$, and $\hat{F}_\phi^{(n)}(r) = -L_{1,n}\sin\beta_1$. The lift force-per-unit-span L_n is calculated by summing the contributions from the bound potential field due to the thickness and loading sources on the bottom propeller calculated using Eqs. (19) and (32).

The components of the force-per-unit-span exerted by the bottom propeller reference blade on the air is also calculated using Eq. (38), but with $\omega_n = nB_1(\Omega_1 + \Omega_2)$, $\hat{F}_x^{(n)}(r) = -L_{2,n}\cos\beta_2$, and $\hat{F}_\phi^{(n)}(r) = L_{2,n}\sin\beta_2$. Here, the lift force-per-unit-span L_n is calculated by summing the contributions from the bound potential field due to the thickness and loading sources on the bottom propeller calculated using Eqs. (21) and (33).

Fig. 9 plots contours of $F_x(r,t)$ for the top rotor reference blade plotted against dimensionless radius (vertical axis) and dimensionless time (horizontal axis) over a period corresponding to one rotation of the top rotor. As expected, there are impulses produced by the interaction of the top rotor reference blade as it passes over each of the blades of the bottom rotor. There is reasonable agreement between the results predicted by the semi-analytical models and the CFD data.
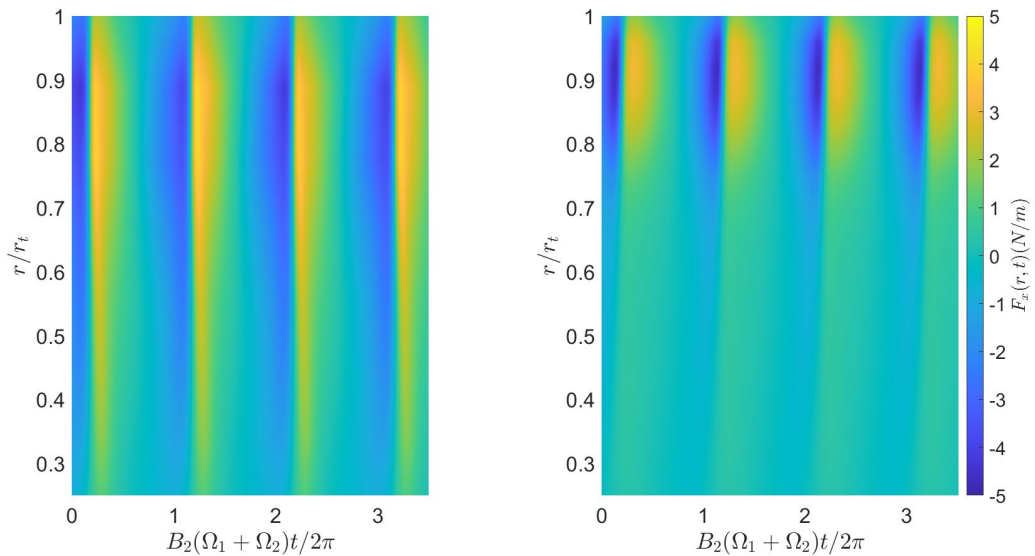
Fig. 9 Contour plot of $F_x(r,t)$ for the top rotor reference blade plotted against dimensionless radius (vertical axis) and dimensionless time (horizontal axis). CFD simulation (left), semi-analytical model (right).

Fig. 10 presents similar results to Fig. 9, but for the bottom rotor. The tip vortex significantly affects the CFD results on the outer portion of the blade which is not captured by the semi-analytical model.
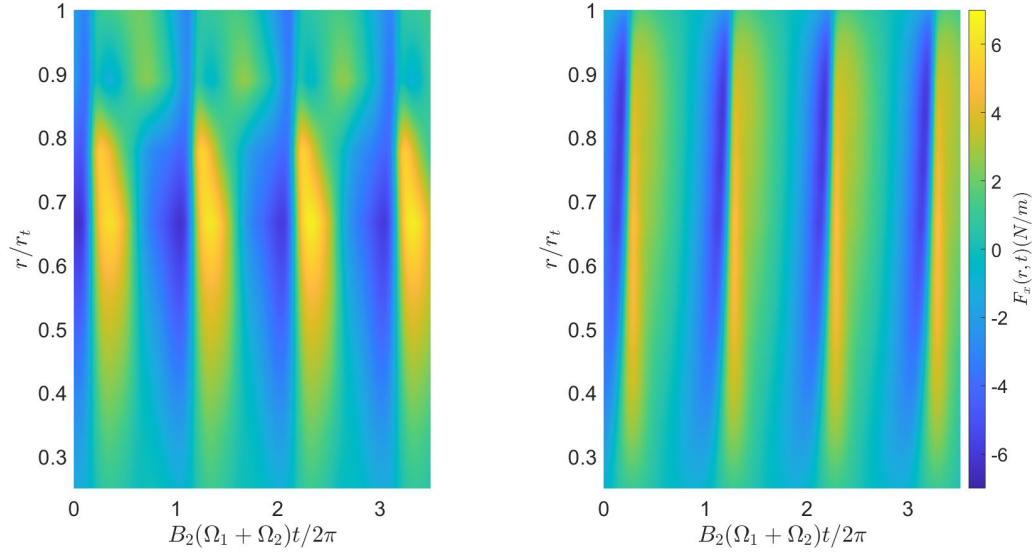
Fig. 10 Contour plot of $F_x(r, t)$ for the bottom rotor reference blade plotted against dimensionless radius (vertical axis) and dimensionless time (horizontal axis). CFD simulation (left), semi-analytical model (right).

Fig. 11 and Fig. 12 present 'pseudocolor' plots showing the magnitude of $\hat{F}_x^{(n)}(r)$ plotted against dimensionless radius (vertical axis) and harmonic number (horizontal axis) for the reference blades of the top and bottom rotors respectively. These results show that most of the unsteady loading is produced by the first few (low frequency) upwash harmonics and the unsteady loading due to the bound potential field is strongest close to the tip region where the lift on the adjacent blade is highest.
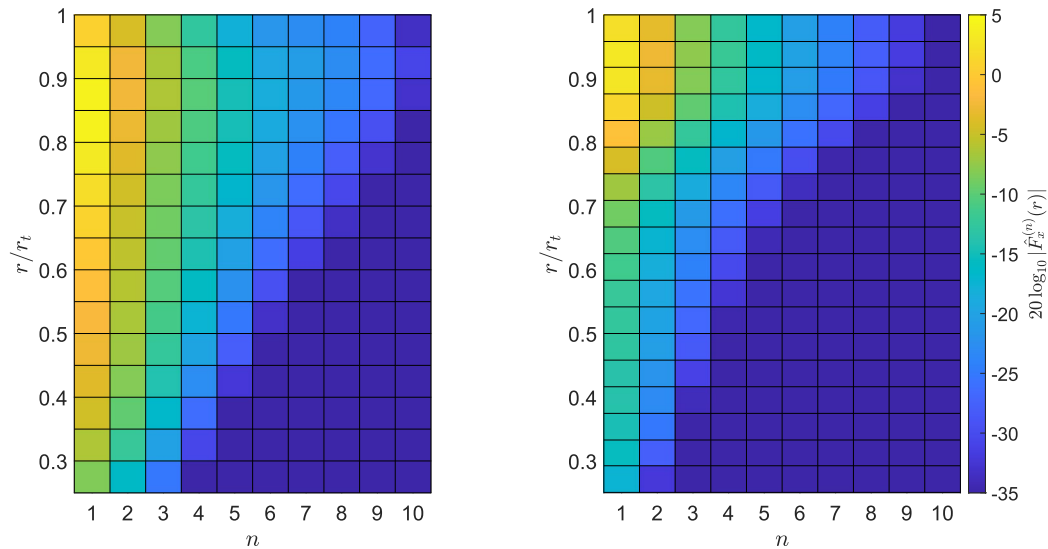
Fig. 11 Pseudocolor plot of $20 \log_{10} \left| \hat{F}_x^{(n)}(r) \right|$ plotted against dimensionless radius (vertical axis) and harmonic number (horizontal axis) for the top rotor. CFD results (left), semi-analytical results (right).
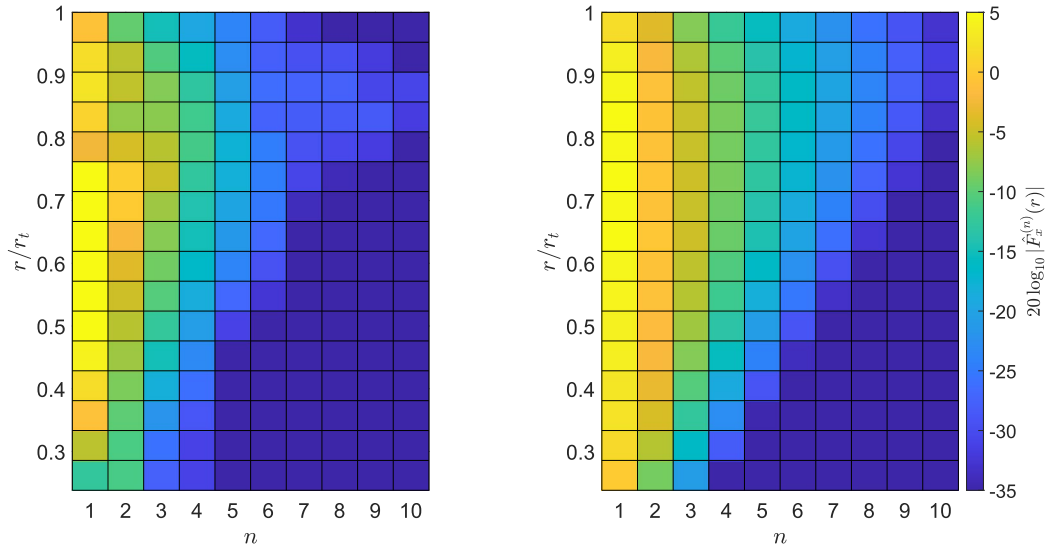
Fig. 12 Pseudocolor plot of $20 \log_{10} \left| \hat{F}_x^{(n)}(r) \right|$ plotted against dimensionless radius (vertical axis) and harmonic number (horizontal axis) for the bottom rotor. CFD results (left), semi-analytical results (right).

2.3 Experiments

Experiments were undertaken in the anechoic chamber at the University of Auckland to measure the noise produced by the contra-rotating UAV rotor system considered in this paper. The contra-rotating rotor systems were each mounted on a Honeywell Model 151 S-type load cell which was used to measure the thrust. The rotors were driven by a custom-made contra-rotating motor unit which consisted of two T-Motor MN501 motors. The motors were controlled using two T-Motor Alpha electronic speed controllers (ESCs) powered by a 48V power supply.

The anechoic chamber at the University of Auckland has internal dimensions of 5.3 m × 5.3 m × 5.3 m and has a cut off frequency below 80 Hz. Acoustic measurements were made using 11 G.R.A.S 46AE ½" microphones which were mounted on a C-shaped support structure as shown in Fig. 13. The microphones were located at polar angles from 0° to 165° in 15° increments. The signals from each microphone were acquired using a National Instruments data acquisition system (which comprised of NI9234 modules in an NI cDAQ-9178 chassis). Measurements were taken over a period of 30 s at a sampling rate of 51.2 kHz
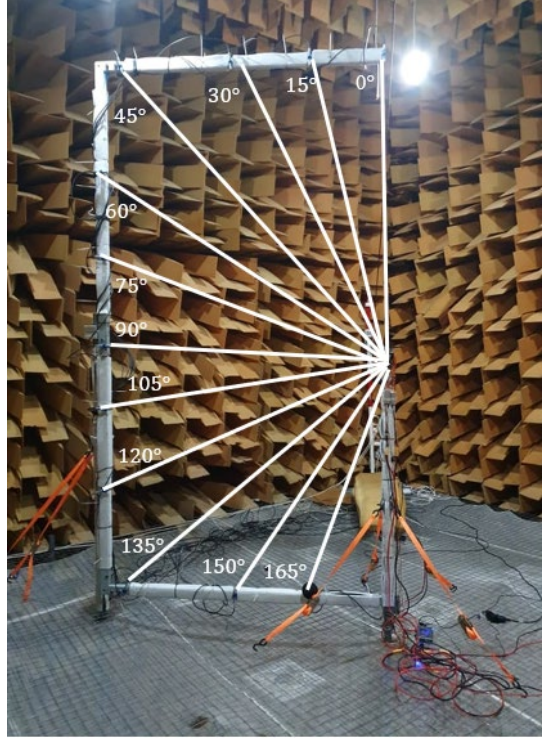
Fig. 13 Experimental setup showing the rotor system mounted in the anechoic chamber surrounded by G.R.A.S. 46AE ½" microphones mounted on a C-Shaped support structure. The annotations indicate the polar angles of the microphones.

For the first rotor system, experiments were performed for rotor systems with 28 different rotor-rotor spacings ranging from 17 mm to 70 mm. The upstream and downstream rotors rotated at constant speeds of 580 rad/s and 440 rad/s respectively for all tests during which the total thrust produced by the rotor system ranged from 18.6 N to 19.6 N. These experiments included the cases modelled using the two CFD simulations with the rotors separated by 40 mm and 60 mm. The experiments for the second rotor system were performed at one rotor-rotor spacing which was at 40mm and both upstream and downstream rotors rotated at the same speeds of 500 rad/s. The total thrust produced measured was approximately 17.6 N. This experiment was also modelled using CFD simulations.

The acoustic pressure measurements were normalised to a distance of 1.5 m from the centre of the rotor system assuming spherical spreading. The results of these measurements were reported previously in McKay et al. [33].

2.4. Frequency-domain noise prediction method

Hanson and Parzych [65] show how Goldstein's acoustic analogy [66] can be used to derive an expression for the sound pressure produced by the loading sources on the surface of a rotating propeller. Following their analysis, the acoustic pressure disturbance, p', at location $\mathbf{x}$ and time t, produced by the unsteady loading exerted by the outer surface of the B_2 (evenly-spaced and identical) blades of the bottom rotor on the air is given by

$$p'(\mathbf{x},t) = \sum_{b=0}^{B_2-1} \int_{-\infty}^{\infty} \int_{A^{(b)}} \mathbf{f}^{(b)}(\mathbf{y},\tau) \cdot \nabla G(\mathbf{y},\tau|\mathbf{x},t) \mathrm{d}A(\mathbf{y})\mathrm{d}\tau, \tag{39}$$

where $\mathbf{f}^{(b)}$ is the stress exerted by the bth blade on the air, $A^{(b)}$ is the outer surface of the bth blade, and G is a Green's function. Note that the observer at $\mathbf{x}$ is assumed to be well away from the propeller blades such that the acoustic pressure is equal to the density fluctuation times the speed of sound in the ambient air. The Green's function is given by

$$G(\mathbf{y}, \tau | \mathbf{x}, t) = \frac{\delta\left(t - \tau - \frac{R}{c_0}\right)}{4\pi R}, \tag{40}$$

where $R = \|\mathbf{x} - \mathbf{y}\|$. This Green's function neglects the effect of any airflow generated by the propeller or due to a mean flow. As this study investigates the noise produced by a rotor system operating in hover, and the airflow speeds generated by the rotor system itself are very low, this is an acceptable assumption for the situation considered here.

For the acoustic analysis, it is most convenient to use coordinate systems with their origins located at the centre of the rotor being considered – which is the approach adopted here. The observer position $\mathbf{x}$ is expressed in spherical coordinates such that

$$\mathbf{x} = \hat{\mathbf{e}}_x R_{\mathbf{x}} \cos\theta_{\mathbf{x}} + \hat{\mathbf{e}}_y R_{\mathbf{x}} \sin\theta_{\mathbf{x}} \cos\phi_{\mathbf{x}} + \hat{\mathbf{e}}_z R_{\mathbf{x}} \sin\theta_{\mathbf{x}} \sin\phi_{\mathbf{x}}, \tag{41}$$

where $R_{\mathbf{x}}$ is the distance from the origin to the observer position, $\theta_{\mathbf{x}}$ and $\phi_{\mathbf{x}}$ are, respectively, the polar and azimuthal angles of the observer and $\hat{\mathbf{e}}_x$, $\hat{\mathbf{e}}_y$, and $\hat{\mathbf{e}}_z$ are the unit vectors in the x, y, and z directions. The axial coordinate (x) is colinear with the rotor axis and is defined positive upwards. The polar coordinate is the angle between the positive x axis and a line between the origin and observer. The azimuthal angle is measured from the y-axis towards the z-axis. The source location, $\mathbf{y}$, is expressed in cylindrical coordinates

$$\mathbf{y} = \hat{\mathbf{e}}_x x_{\mathbf{y}} + \hat{\mathbf{e}}_y r_{\mathbf{y}} \cos\phi_{\mathbf{y}} + \hat{\mathbf{e}}_z r_{\mathbf{y}} \sin\phi_{\mathbf{y}}, \tag{42}$$

where $x_{\mathbf{y}}$ is the axial (x) coordinate of the source location, $r_{\mathbf{y}}$ is the shortest distance between $\mathbf{y}$ and the rotor axis (i.e. the cylindrical radius of the source location), and $\phi_{\mathbf{y}}$ is the azimuthal angle of the source location. Note that the bottom rotor rotates in the positive $\phi_{\mathbf{y}}$ direction.

It will be convenient to utilise a coordinate system, $\mathbf{y}'$, which rotates with the rotor blades and which is defined by an expression which is identical to Eq. (42), but with $\phi_{\mathbf{y}}$ replaced by $\phi_{\mathbf{y}}'$ where

$$\phi_{\mathbf{y}} = \Omega_2 \tau + \phi_{\mathbf{y}}' - \frac{2\pi b}{B_2} \text{ (modulo } 2\pi), \tag{43}$$

where $\phi_{\mathbf{y}}'$ is the azimuthal angle of the corresponding point on the reference blade (for which $b = 0$) at time $\tau = 0$.

The loading on the reference blade of the bottom rotor will be periodic with period $T = \frac{2\pi}{B_1(\Omega_1 + \Omega_2)}$. The loading can thus be written as a Fourier series

$$\mathbf{f}^{(0)}(\mathbf{y}, \tau) = \sum_{n_1 = -\infty}^{\infty} \hat{\mathbf{f}}^{(n_1)}(\mathbf{y}') \exp\{i n_1 B_1 (\Omega_1 + \Omega_2) \tau\}. \tag{44}$$

A point on the bth blade on the lower rotor is offset from a corresponding point on the reference blade by an azimuthal angle of magnitude $\frac{2\pi b}{B_2}$. Because this blade is interacting with a counter-rotating disturbance which rotates relative to the bottom rotor blades at a rotational speed equal to $\Omega_1 + \Omega_2$,

the loading on the bth blade is therefore offset in time from the loading on the reference blade by a period of $\dfrac{2\pi b}{B_2(\Omega_1+\Omega_2)}$ and thus

$$\mathbf{f}^{(b)}(\mathbf{y},\tau) = \sum_{n_1=-\infty}^{\infty} \hat{\mathbf{f}}^{(n_1)}(\mathbf{y}') \exp\left\{in_1 B_1(\Omega_1+\Omega_2)\tau - i2\pi n_1 b\frac{B_1}{B_2}\right\}. \tag{45}$$

It will be useful to define a temporal Fourier transform

$$\tilde{p}(\mathbf{x},\omega) = \frac{1}{2\pi}\int_{-\infty}^{\infty} p'(\mathbf{x},t)\exp\{-i\omega t\}\,dt. \tag{46}$$

Substituting Eqs. (40) and (45) into Eq. (39) and applying Eq. (46) to the result yields

$$\tilde{p}(\mathbf{x},\omega) = \frac{1}{2\pi}\sum_{n_1=-\infty}^{\infty}\sum_{b=0}^{B_2-1}\exp\left\{-i2\pi n_1 b\frac{B_1}{B_2}\right\}\int_{-\infty}^{\infty}\int_{A^{(b)}} \hat{\mathbf{f}}^{(n_1)}(\mathbf{y}')\cdot\nabla G_\omega(\mathbf{y}|\mathbf{x})\exp\{i[n_1 B_1(\Omega_1+\Omega_2)-\omega]\tau\}\,dA\,d\tau, \tag{47}$$

where

$$G_\omega(\mathbf{y}|\mathbf{x}) = \frac{\exp\{-i\kappa R\}}{4\pi R}, \tag{48}$$

and $\kappa = \dfrac{\omega}{c_0}$ is the acoustic wavenumber.

In the acoustic far-field, as $R_{\mathbf{x}}\to\infty$, G_ω can be approximated as (see Hanson and Parzyck)

$$G_\omega \approx \frac{\exp\{-i\kappa R_{\mathbf{x}} + i\kappa x_{\mathbf{y}}\cos\theta_{\mathbf{x}} + i\kappa r_{\mathbf{y}}\sin\theta_{\mathbf{x}}\cos(\phi_{\mathbf{y}}-\phi_{\mathbf{x}})\}}{4\pi R_{\mathbf{x}}}. \tag{49}$$

The Jacobi-Anger expansion can be used to rewrite Eq. (49) as

$$G_\omega \approx \frac{\exp\{-i\kappa R_{\mathbf{x}} + i\kappa x_{\mathbf{y}}\cos\theta_{\mathbf{x}}\}}{4\pi R_{\mathbf{x}}}\sum_{n=-\infty}^{\infty} J_n\left(\kappa r_{\mathbf{y}}\sin\theta_{\mathbf{x}}\right)\exp\left\{in\left(\phi_{\mathbf{y}}-\phi_{\mathbf{x}}+\frac{\pi}{2}\right)\right\}, \tag{50}$$

where $J_n(\cdot)$ is the Bessel function of the first kind.

Substituting Eq. (50) into Eq. (47), making use of Eq. (43), evaluating the integral over τ, setting $n \to B_2 n_2 - n_1 B_1$, and taking the inverse Fourier transform yields

$$p'(\mathbf{x},t) = \sum_{n_1=-\infty}^{\infty}\sum_{n_2=-\infty}^{\infty}\frac{\exp\left\{i\omega\left(t-\dfrac{R_{\mathbf{x}}}{c_0}\right) - i\nu\left(\phi_{\mathbf{x}}-\dfrac{\pi}{2}\right)\right\}}{4\pi R_{\mathbf{x}}} I, \tag{51}$$

where

$$\omega = n_1 B_1\Omega_1 + n_2 B_2\Omega_2, \tag{52}$$

is the frequency of each term in the double summation,

$$\nu = n_2 B_2 - n_1 B_1, \tag{53}$$

is the azimuthal wave number of each term in the double summation and

$$I = B_2 \int\limits_{A^{(0)}} \left[i\kappa \cos\theta_\mathbf{x} J_\nu(\kappa r_\mathbf{y} \sin\theta_\mathbf{x}) \hat{f}_x^{(n_1)} + \kappa \sin\theta_\mathbf{x} J_\nu'(\kappa r_\mathbf{y} \sin\theta_\mathbf{x}) \hat{f}_r^{(n_1)} + \frac{i\nu}{r_\mathbf{y}} J_\nu(\kappa r_\mathbf{y} \sin\theta_\mathbf{x}) \hat{f}_\phi^{(n_1)} \right]$$

$$\times \exp\{i\kappa x_\mathbf{y} \cos\theta_\mathbf{x} + i\nu\phi_\mathbf{y}'\} \, \mathrm{d}A, \tag{54}$$

is an integral of 'source terms' over the outer surface of the reference blade ($A^{(0)}$), and where $\hat{f}_x^{(n_1)}$, $\hat{f}_r^{(n_1)}$, and $\hat{f}_\phi^{(n_1)}$ are the axial, radial and azimuthal components of $\hat{\mathbf{f}}^{(n_1)}$.

Assuming that the phase difference due to sources at different points at the same radius can be neglected, and that the radial loading terms are sufficiently small that they can also be neglected, the integral can be written as

$$I = B_2 \int\limits_{r_h}^{r_t} \left[i\kappa \cos\theta_\mathbf{x} \hat{F}_x^{(n_1)}(r_\mathbf{y}) + \frac{i\nu}{r_\mathbf{y}} \hat{F}_\phi^{(n_1)}(r_\mathbf{y}) \right] J_\nu(\kappa r_\mathbf{y} \sin\theta_\mathbf{x}) \exp\{i\kappa x_{\mathbf{y},0} \cos\theta_\mathbf{x} + i\nu\phi_{\mathbf{y},0}'\} \, \mathrm{d}r_\mathbf{y}, \tag{55}$$

where $\hat{F}_x^{(n_1)}$, and $\hat{F}_\phi^{(n_1)}$ are the Fourier harmonics of the force-per-unit length exerted by the reference blade on the air, r_h is the hub radius, and $x_{\mathbf{y},0}$ and $\phi_{\mathbf{y},0}'$ are the values of $x_\mathbf{y}$ and $\phi_\mathbf{y}'$ at the blade mid-chord where the 'acoustic sources' are assumed to be located.

Note that on-axis ($\theta_\mathbf{x} = 0°$ or $180°$), for the cases considered in this paper where $B_1 = B_2$, only tones for which $n_2 = n_1$ will radiate. It is also assumed that the propeller blades are thin and do not deform significantly from the $x = 0$ plane. For that case, the summation over n_2 is eliminated, and the expression for the radiated acoustic pressure reduces to

$$p'(\mathbf{x}, t) = \sum_{n_1=-\infty}^{\infty} iB_2 n_1 B_1 (\Omega_1 + \Omega_2) \frac{\exp\left\{ in_1 B_1 (\Omega_1 + \Omega_2) \left(t - \frac{R_\mathbf{x}}{c_0} \right) \right\}}{4\pi R_\mathbf{x} c_0} \int\limits_{A^{(0)}} \hat{f}_x^{(n_1)} \, \mathrm{d}A, \tag{56}$$

where the integral is equal to the Fourier harmonic of the total axial force acting on the reference blade.

Equivalent expressions can also be derived for the acoustic field radiated from the top rotor. In this case, the far-field acoustic pressure is given by Eq. (51), but with the coordinates adjusted so that the origin lies at the centre of the top rotor, and with I defined as

$$I = B_1 \int\limits_{A^{(0)}} \left[i\kappa \cos\theta_\mathbf{x} J_\nu(\kappa r_\mathbf{y} \sin\theta_\mathbf{x}) \hat{f}_x^{(n_2)} + \kappa \sin\theta_\mathbf{x} J_\nu'(\kappa r_\mathbf{y} \sin\theta_\mathbf{x}) \hat{f}_r^{(n_2)} + \frac{i\nu}{r_\mathbf{y}} J_\nu(\kappa r_\mathbf{y} \sin\theta_\mathbf{x}) \hat{f}_\phi^{(n_2)} \right]$$

$$\times \exp\{i\kappa x_\mathbf{y} \cos\theta_\mathbf{x} + i\nu\phi_\mathbf{y}'\} \, \mathrm{d}A, \tag{57}$$

where the integration is over the outer surface of the reference blade of the top rotor ($A^{(0)}$), and where $\hat{f}_x^{(n_2)}$, $\hat{f}_r^{(n_2)}$, and $\hat{f}_\phi^{(n_2)}$ are the axial, radial and azimuthal components of $\hat{\mathbf{f}}^{(n_2)}$, which is the n_2^{th} Fourier harmonic of the periodic stress on $A^{(0)}$.

Assuming that the phase difference due to sources at different points at the same radius can be neglected, and that the radial loading terms are sufficiently small that they can also be neglected, Eq. (57) can also be written as

$$I = B_1 \int_{r_h}^{r_t} \left[i\kappa \cos\theta_{\mathbf{x}} \hat{F}_x^{(n_2)}(r_{\mathbf{y}}) + \frac{i\nu}{r_{\mathbf{y}}} \hat{F}_\phi^{(n_2)}(r_{\mathbf{y}}) \right] J_\nu(\kappa r_{\mathbf{y}} \sin\theta_{\mathbf{x}}) \exp\{i\kappa x_{\mathbf{y},0} \cos\theta_{\mathbf{x}} + i\nu\phi'_{\mathbf{y},0}\} \, dr_{\mathbf{y}}, \qquad (58)$$

where, similar to before, $x_{\mathbf{y},0}$ and $\phi'_{\mathbf{y},0}$ are the values of $x_{\mathbf{y}}$ and $\phi'_{\mathbf{y}}$ at the blade mid-chord (this time of the top rotor) where the 'acoustic sources' are assumed to be located.

Eqs. (54) and (57) were used to calculate the radiated noise field using the CFD loading data. Eqs. (55) and (58) were used to calculate the radiated noise field using the loading calculated from the semi-analytical models.

For the case where the observer is on-axis and the rotor blades can be assumed to be thin and do not deform significantly from the $x = 0$ plane, for the case considered here where $B_2 = B_1$, the acoustic pressure radiated from the top propeller is given by

$$p'(\mathbf{x}, t) = \sum_{n_2=-\infty}^{\infty} iB_1 n_2 B_2 (\Omega_1 + \Omega_2) \frac{\exp\left\{ in_2 B_2 (\Omega_1 + \Omega_2) \left(t - \frac{R_{\mathbf{x}}}{c_0} \right) \right\}}{4\pi R_{\mathbf{x}} c_0} \int_{A^{(0)}} \hat{f}_x^{(n_2)} \, dA. \qquad (59)$$

Equations (22), and (25) are similar to those presented in McKay et al. [33], but include the effect of the source being offset from the pitch-change axis (i.e. the expressions are generalised to be able to be applied to blades which are not straight). Note that McKay et al. defined the azimuthal loading component as being positive in the direction opposite to the direction of rotation of the rotor, whereas here the tangential force is defined positive in the positive ϕ direction regardless of the direction of rotation of the rotor. These expressions and their numerical implementation were validated by comparison of pressure time-histories calculated using them with time-histories calculated using an implementation of Farassat's formulation 1A [67–69]. These comparisons were performed at many different observer locations for several different operating conditions and there was excellent agreement between the results calculated using both methods for all cases. The advantage of the frequency-domain method is that it can rapidly predict the noise level for a single tone and only requires one period of loading data.

2.5 Comparison between measurements, prediction from CFD and analytical models

Fig. 14 and Fig. 15 plot the measured and predicted sound pressure level directivity for seven different interaction tones produced by the first rotor system. Similarly, Fig. 16 and Fig. 17 plot the measured and predicted sound pressure level directivity for identical interaction tones produced by the second setup. Two sets of predictions were made: the first used the loading data calculated from the semi-analytical models described in § 2.1.2 with the radiated acoustic pressure calculated using the simple acoustic radiation formulae; whilst the second set of predictions was made using the loading data from the CFD simulations with the radiated acoustic pressure calculated using the exact acoustic radiation formulae. The agreement between both sets of predictions and the measurements is very good for both setups. This indicates that the unsteady loading on the rotor blades is well-predicted by both the CFD and semi-analytical methods and that the bound potential field interactions are a significant contributor to this loading. It is observed that the tones for which $n_1 = n_2$ radiate strongly along the rotor axis (i.e. at polar angles 0° and 180°) as expected. The $\{n_1 = 4, n_2 = 3\}$ interaction tone has a different directivity pattern from the other three interaction tones plotted in Fig. 12. This term has a non-zero azimuthal wavenumber (ν) and thus the Bessel function terms in the acoustic radiation formulae have a non-zero order which significantly alters the directivity of these tones.
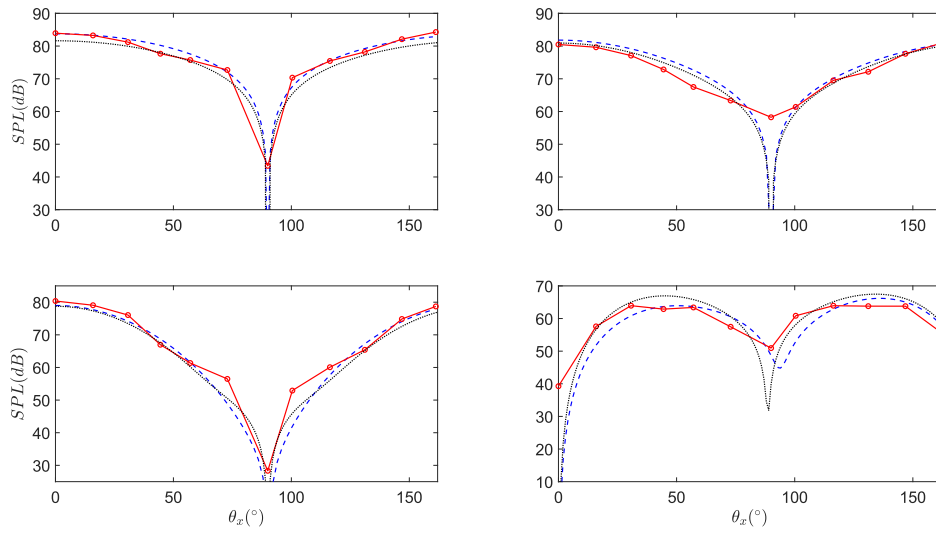
Fig. 14 Sound pressure level polar directivity for four different interaction tones. Experimental measurements (red curve with circle markers). Numerical prediction (dashed blue curve). Semi-analytical predictions (dotted black curve). $\{n_1 = 1, n_2 = 1\}$ **tone (top left),** $\{n_1 = 2, n_2 = 2\}$ **tone (top right),** $\{n_1 = 3, n_2 = 3\}$ **tone (bottom left),** $\{n_1 = 4, n_2 = 3\}$ **tone (bottom right). In this case, the top rotor rotated at 580 rad/s and the bottom rotor rotated at 440 rad/s.**
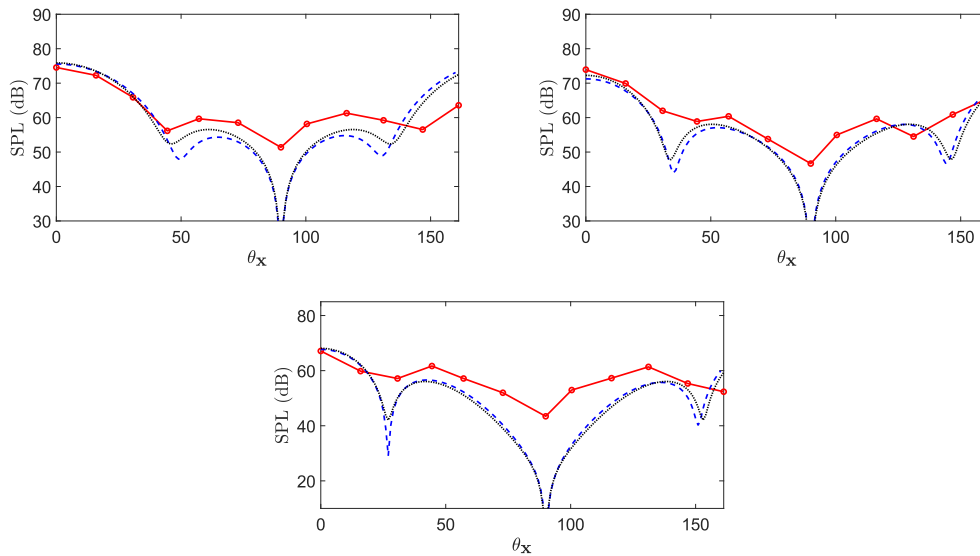
Fig. 15 Sound pressure level polar directivity for three different interaction tones. Experimental measurements (red curve with circle markers). Numerical prediction (dashed blue curve). Semi-analytical predictions (dotted black curve). $\{n_1 = 4, n_2 = 4\}$ **tone (top left),** $\{n_1 = 5, n_2 = 5\}$ **tone (top right),** $\{n_1 = 6, n_2 = 6\}$ **tone (bottom centre). In this case, the top rotor rotated at 580 rad/s and the bottom rotor rotated at 440 rad/s.**

33
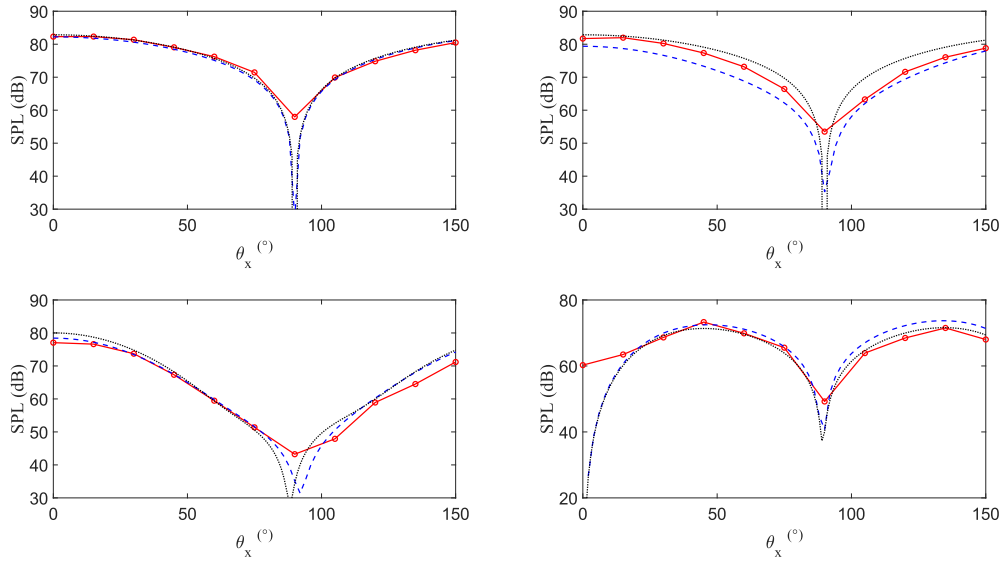
Fig. 16 Sound pressure level polar directivity for three different interaction tones. Experimental measurements (red curve with circle markers). Numerical prediction (dashed blue curve). Semi-analytical predictions (dotted black curve).$\{n_1 = 1, n_2 = 1\}$ tone (top left), $\{n_1 = 2, n_2 = 2\}$ tone (top right), $\{n_1 = 3, n_2 = 3\}$ tone (bottom left) and $\{n_1 = 4, n_2 = 3\}$ tone (bottom right). In this case, the top and bottom rotor rotated at 500 rad/s.
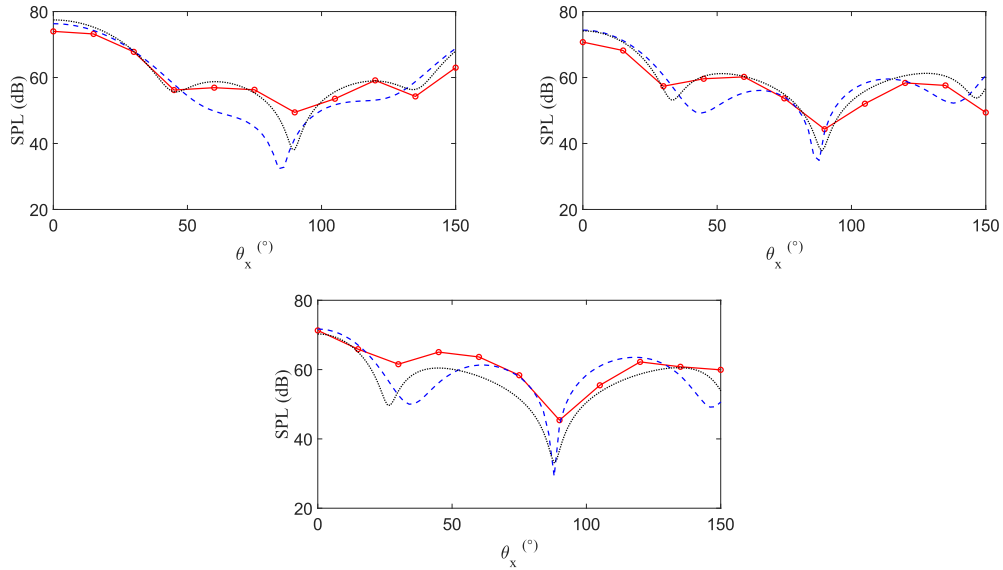
Fig. 17 Sound pressure level polar directivity for three different interaction tones. Experimental measurements (red curve with circle markers). Numerical prediction (dashed blue curve). Semi-analytical predictions (dotted black curve).$\{n_1 = 4, n_2 = 4\}$ tone (top left), $\{n_1 = 5, n_2 = 5\}$ tone (top right), $\{n_1 = 6, n_2 = 6\}$ tone (bottom centre). In this case, the top and bottom rotor rotated at 500 rad/s.

Fig. 18 and Fig. 19 plot the measured spectra and predicted sound pressure levels of prominent interaction tones produced by the first rotor system at observer polar angles of $\theta_x = 0°$ and $45°$ respectively. Similarly, Fig. 20 and Fig. 21 presents the measured spectra and predicted sound pressure level of interaction tones produced by the second rotor system at the corresponding observer locations. For both rotor systems, two sets of predictions are made; one using the semi-analytical model and the other using the loading calculated by the CFD simulations. For most interaction tones, the agreement between the measured spectra and predicted sound pressure level is very good. It is also

observed that interaction tones with zero azimuthal order (i.e., interaction tones for which $n_1 = n_2$) dominate the spectra at $\theta_x = 0°$. The sound pressure level of these interaction tones decreases as the observer's location moves away from the axis. For the spectra produced by the second rotor system, the amplitude of the interaction tones with zero azimuthal order has contributions from a multiple of interaction tones. This is because both rotors are rotating at the same speed and interaction tones occur at the same frequency. For example, the {2,2} interaction tone occurs at a frequency of 640 Hz. Additionally, the {3,1} and {1,3} interaction tones also occur at the same frequency. Therefore, predictions were made by summing the contributions from all interaction tones which occurred at that frequency.

Fig. 18 Sound pressure level spectrum produced by the first rotor system at $\theta_x = 0°$. The numbers in the curly brackets indicate the values of $\{n_1, n_2\}$ for each tone. The measured narrow-band spectrum is shown in blue. The experimentally determined tone level is denoted by red circle markers, numerical predictions are shown in blue triangles and semi-analytical predictions are shown with black pentagrams. In this case, the top rotor rotated at 580 rad/s and the bottom rotor rotated at 440 rad/s.
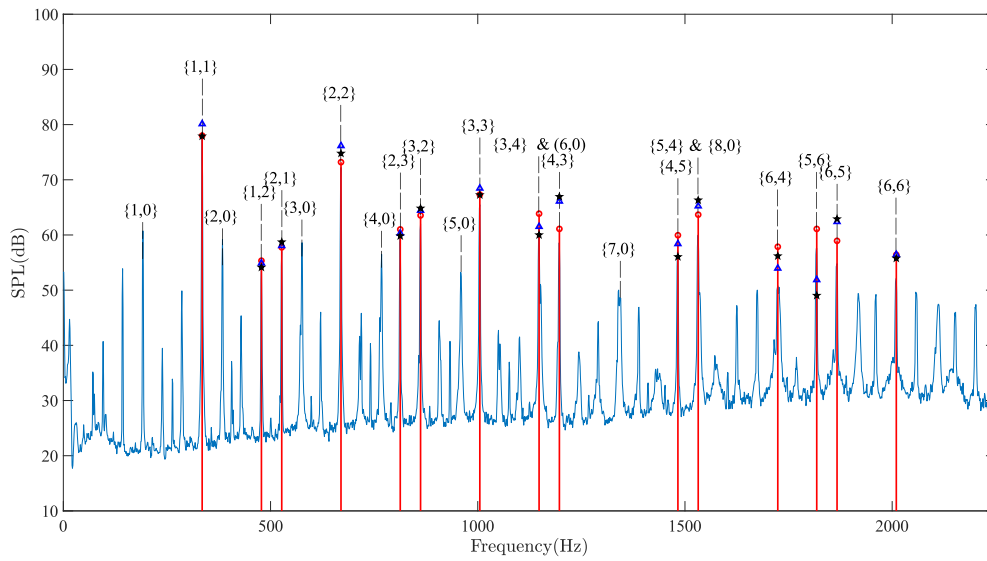
Fig. 19 Sound pressure level spectrum produced by the first rotor system at $\theta_x = 45°$. The numbers in the curly brackets indicate the values of $\{n_1, n_2\}$ for each tone. The measured narrow-band spectrum is shown in blue. The experimentally determined tone level is denoted by red circle markers, numerical predictions are shown in blue triangles and semi-analytical predictions are shown with black pentagrams. In this case, the top rotor rotated at 580 rad/s and the bottom rotor rotated at 440 rad/s.
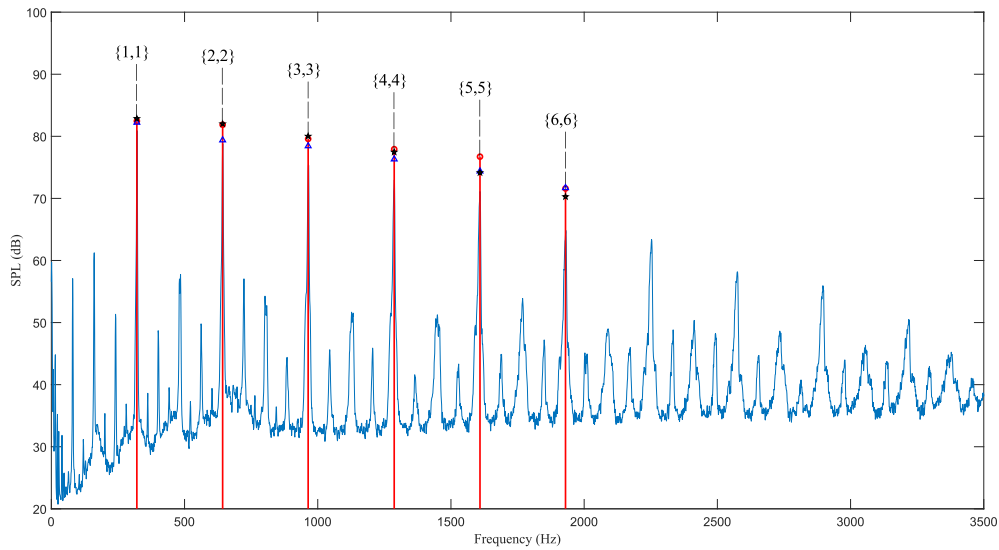
Fig. 20 Sound pressure level spectrum produced by the second rotor system at $\theta_x = 0°$. The numbers in the curly brackets indicate the values of $\{n_1, n_2\}$ for each tone. The measured narrow-band spectrum is shown in blue. The experimentally determined tone level is denoted by red circle markers, numerical predictions are shown in blue triangles and semi-analytical predictions are shown with black pentagrams. In this case, the top and bottom rotor rotated at 500 rad/s.
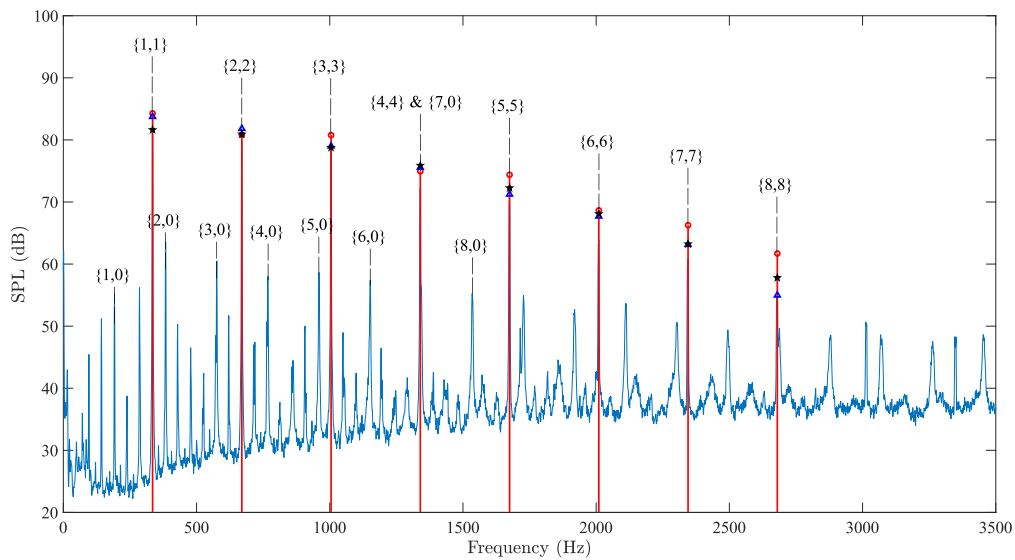
36
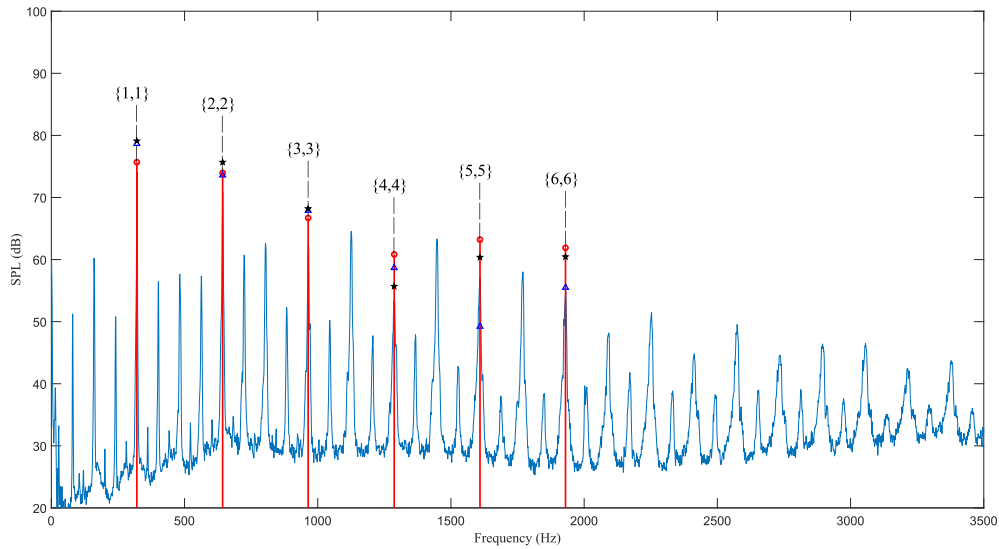
Fig. 21 Sound pressure level spectrum produced by the second rotor system at $\theta_x = 45°$. The numbers in the curly brackets indicate the values of $\{n_1, n_2\}$ for each tone. The measured narrow-band spectrum is shown in blue. The experimentally determined tone level is denoted by red circle markers, numerical predictions are shown in blue triangles and semi-analytical predictions are shown with black pentagrams. In this case, the top and bottom rotor rotated at 500 rad/s.

Fig. 22 plots the measured and predicted sound pressure level for three different interaction tones measured on the rotor axis at $\theta_x = 0$ produced by the first rotor system. It is observed that the sound pressure level decreases with increasing rotor spacing. Predictions were made using the CFD simulations for rotor spacings of 40 mm and 60 mm. The steady loading data from the 40 mm separation case was used as input to the semi-analytical models for calculating unsteady blade loading and then the simple acoustic radiation formula was used to make predictions at all rotor spacings. The predictions are in modest agreement with the measurements, but the predictions made using the semi-analytical models capture the general decrease in the sound pressure level with increasing rotor spacing which strongly supports the hypothesis that the bound potential field interactions are the primary cause of these tones. The rate of decrease observed in the measurements and predicted using the semi-analytical models is consistent with the findings of Parry [62], Parry et al. [70] and Chaitanya et al. [34] who show that the magnitude of the velocity perturbations and thus the unsteady loading and radiated acoustic pressure decay exponentially as the rotor spacing increases.
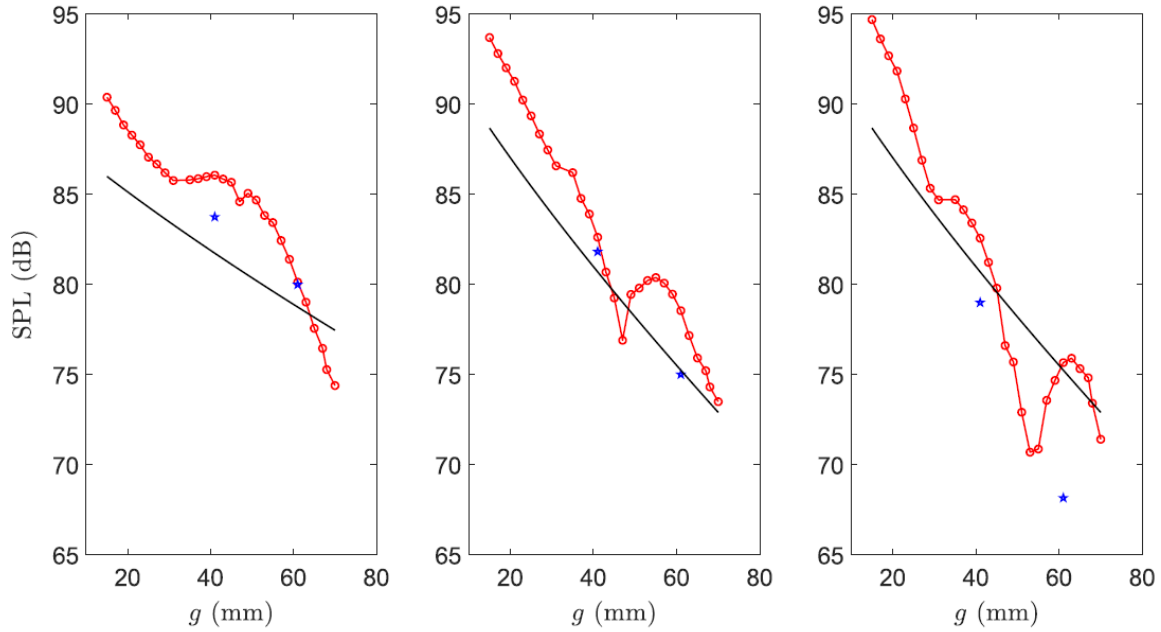
Fig. 22 Sound pressure level versus rotor spacing, g, for three different interaction tones at $\theta_x = 0$. Experimental measurements (red curve with circle markers). Numerical predictions (blue pentagrams). Semi-analytical predictions (solid black curve).$\{n_1 = 1, n_2 = 1\}$ tone (left), $\{n_1 = 2, n_2 = 2\}$ tone (middle), $\{n_1 = 3, n_2 = 3\}$ tone (right). In this case, the top rotor rotated at 580 rad/s and the bottom rotor rotated at 440 rad/s.

2.6 Chapter summary

This chapter has investigated the interaction tones produced by two sets of contra-rotating UAV rotor systems. These tones are caused by the periodic unsteady loading on the rotor blades. CFD simulations were used to calculate this loading. In addition to this, a semi-analytical model was used to estimate the loading on the rotor blades due to their interaction with the bound potential field of the adjacent rotor.

It was shown that there was reasonable agreement between the periodic unsteady loading on the top rotor blades predicted using the semi-analytical model and the CFD simulations. The periodic unsteady loading on the bottom rotor blades is caused by their interaction with the bound potential field, viscous wakes and tip vortices from the top rotor. Although the bound potential field appears to contribute significantly to the loading on the lower rotor blades, unsteady loading close to the rotor tip caused by its interaction with the tip vortices from the top rotor seems to dominate in this region.

A frequency domain method, similar to that developed by Hanson [8], was presented for predicting the interaction tones produced by the periodic loading on the rotor blades. This method was used to predict the sound pressure level directivity for a number of different interaction tones produced by two rotor systems with a 40 mm spacing between the rotors using loading data taken from the CFD simulations. These predictions were in generally good agreement with measurements. Predictions were also made using blade loadings calculated using the semi-analytical models and a simplified radiation formulation. These predictions were also in good agreement with the full numerical predictions and measurements indicating the importance of the bound potential field interaction noise source for this particular case. The effect of rotor spacing was also investigated using data from two CFD simulations and also the semi-analytical models. There was modest agreement between the predictions and the measurements, however the predictions captured the strong decay of the level of these tones as rotor spacing increased.

Appendix 2.1. Frequency-domain noise prediction method validation

This appendix presents a validation of the frequency-domain method by comparing predictions made using it with predictions made using an implementation of Farassat's formulation 1A [71] time-domain prediction method. The implementation of Farassat's formulation 1A was provided by Dr Ryan McKay and its validation is presented in ref. [67].

The first validation case considered here is for a rotating point force which rotates about the x-axis in the $x = 0$ plane. The point force has magnitude given by

$$F(t) = A \cos\big((\Omega_1 + \Omega_2)t\big) \tag{A2 1}$$

where A is an arbitrary constant force amplitude and Ω_1 and Ω_2 are the rotational speeds of the top and bottom propellers. Note that Eq. (A2 1) specifies a force which is periodic with period $2\pi/(\Omega_1 + \Omega_2)$ and thus has the form required for the frequency domain prediction method for the case where $B_1 = B_2 = 1$.

The validation was done for a number of different cases in which the following parameters were varied: the radius of the force; the rotational speed and direction of rotation of the force; the force orientation (purely axial, radial, or tangential); and the polar angle of the observer.

In order to assess whether the frequency domain method correctly simulated the noise produced by the stresses acting on the top propeller, a case was considered where the force rotated in the negative ϕ direction. The radius of the force and its rotational speed was varied to give Mach numbers of approximately 0.3, 0.6 or 0.9. Fig. A2. 1, Fig. A2. 2 and Fig. A2. 3 show the results obtained for an axial point force at two different observer polar angles for a number of different Mach numbers (the parameters used in the calculations are given in the captions). The observer azimuthal angle was $\phi_x = 0$ for all cases. The agreement between the predictions made using the time- and frequency-domain methods is excellent.

Fig. A2. 1 Comparison of the far-field pressure predicted using the time- and frequency-domain methods. For this case the force is purely axial, rotates in the negative ϕ-direction, $\Omega_1 = 580$ rad/s, $\Omega_2 = 440$ rad/s, the force radius is 0.1905 m, $A = 5$ N, and $R_x = 100$ m. The Mach number of the rotating force is 0.3. The time domain method predictions are shown using the red curve frequency domain method predictions are shown using blue stars.

Fig. A2. 2 Comparison of the far-field pressure predicted using the time- and frequency-domain methods. For this case the force is purely axial, rotates in the negative ϕ-direction, $\Omega_1 = 680$ rad/s, $\Omega_2 = 500$ rad/s, the force radius is 0.3 m, $A = 5$ N, and $R_x = 100$ m. The Mach number of the rotating force is 0.6. The time domain method predictions are shown using the red curve frequency domain method predictions are shown using blue stars.

Fig. A2. 3 Comparison of the far-field pressure predicted using the time- and frequency-domain methods. For this case the force is purely axial, rotates in the negative ϕ-direction, $\Omega_1 = 780$ rad/s, $\Omega_2 = 600$ rad/s, the force radius is 0.395 m, $A = 5$ N, and $R_x = 100$ m. The Mach number of the rotating force is 0.9. The time domain method predictions are shown using the red curve frequency domain method predictions are shown using blue stars.

Fig. A2. 4 and Fig. A2. 5 plot the acoustic pressure vs time at two different observer locations for a radial (Fig. A2. 4) and a tangential (Fig. A2. 5) point force rotating in the negative ϕ-direction. Aside from the orientation of the point force, the parameters used in these simulations are identical to those used to generate the results shown in Fig. A2. 1. Once again, the agreement is excellent.

41

Fig. A2. 4 Comparison of the far-field pressure predicted using the time- and frequency-domain methods. For this case the force is purely radial, rotates in the negative ϕ-direction, Ω_1 = 580 rad/s, Ω_2= 440 rad/s, the force radius is 0.1905 m, A = 5 N, and R_x = 100 m. The Mach number of the rotating force is 0.3. The time domain method predictions are shown using the red curve frequency domain method predictions are shown using blue stars.

Fig. A2. 5 Comparison of the far-field pressure predicted using the time- and frequency-domain methods. For this case the force is purely tangential, rotates in the negative ϕ-direction, Ω_1 = 580 rad/s, Ω_2= 440 rad/s, the force radius is 0.1905 m, A = 5 N, and R_x = 100 m. The Mach number of the rotating force is 0.3. The time domain method predictions are shown using the red curve frequency domain method predictions are shown using blue stars.

In order to assess whether then frequency domain method correctly simulated the noise produced by the stresses acting on the bottom propeller, a case was considered where the force rotated in the positive ϕ direction. The radius of the force and its rotational speed was varied to give Mach numbers of approximately 0.2, 0.4 or 0.7. Fig. A2. 6, Fig. A2. 7 and Fig. A2. 8 show the results obtained for an axial point force at two different observer polar angles for a number of different Mach numbers (the parameters used in the calculations are given in the captions). The observer azimuthal angle was ϕ_x = 0 for all cases. The agreement between the predictions made using the time- and frequency-domain methods is excellent.
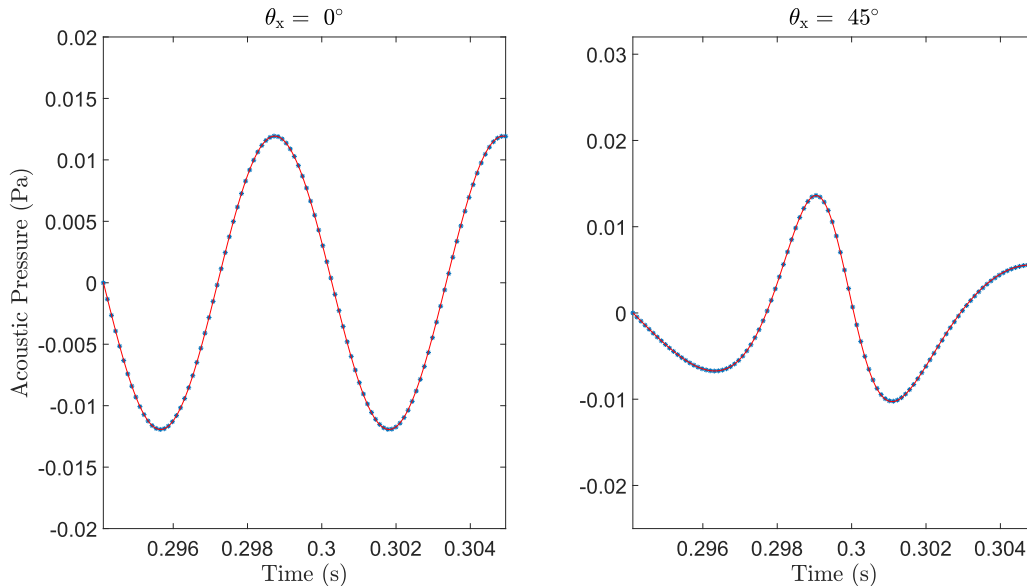
42
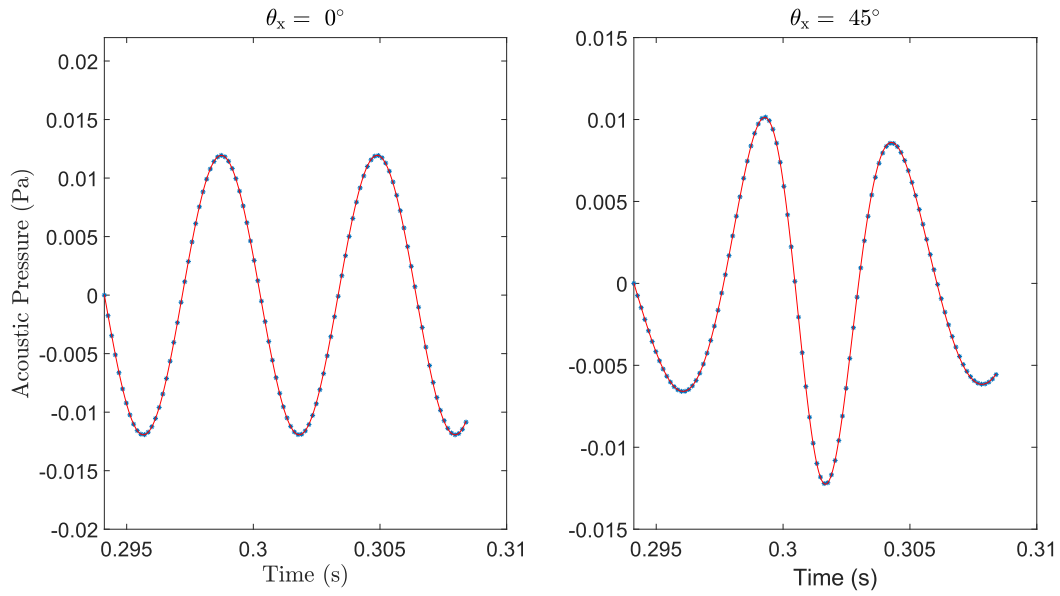
Fig. A2. 6 Comparison of the far-field pressure predicted using the time- and frequency-domain methods. For this case the force is purely axial, rotates in the positive ϕ-direction, Ω_1 = 580 rad/s, Ω_2= 440 rad/s, the force radius is 0.1905 m, A = 5 N, and R_x = 100 m. The Mach number of the rotating force is 0.2. The time domain method predictions are shown using the red curve frequency domain method predictions are shown using blue stars.
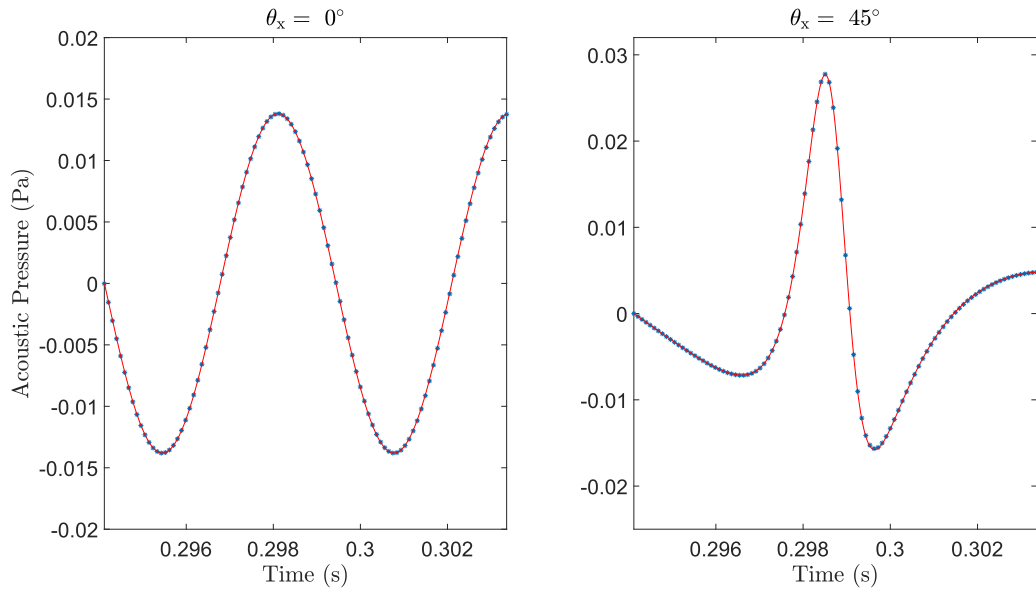

Fig. A2. 7 Comparison of the far-field pressure predicted using the time- and frequency-domain methods. For this case the force is purely axial, rotates in the positive ϕ-direction, Ω_1 = 680 rad/s, Ω_2= 500 rad/s, the force radius is 0.3 m, A = 5 N, and R_x = 100 m. The Mach number of the rotating force is 0.4. The time domain method predictions are shown using the red curve frequency domain method predictions are shown using blue stars.
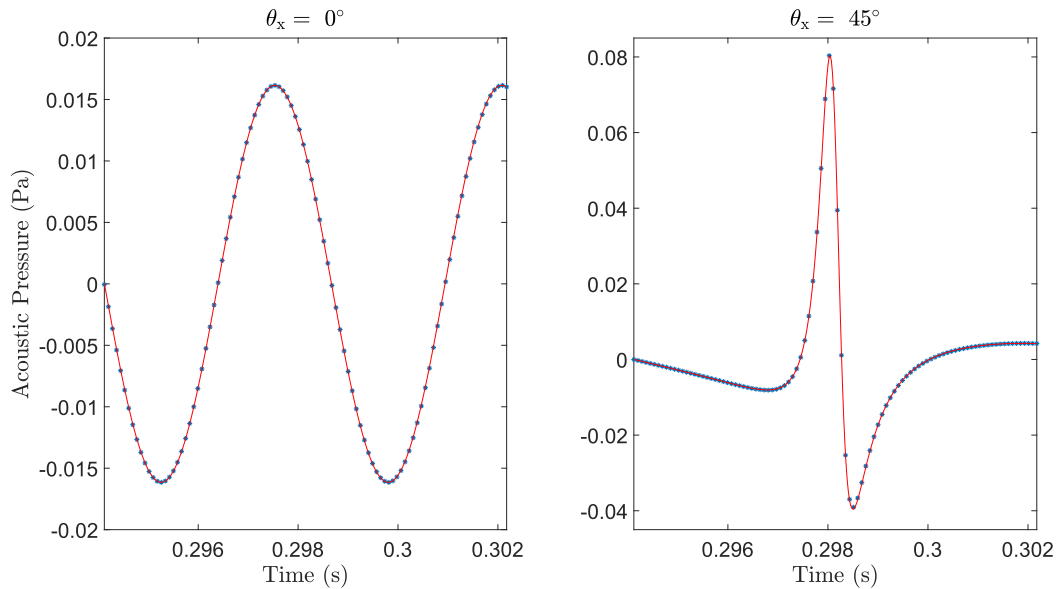
43
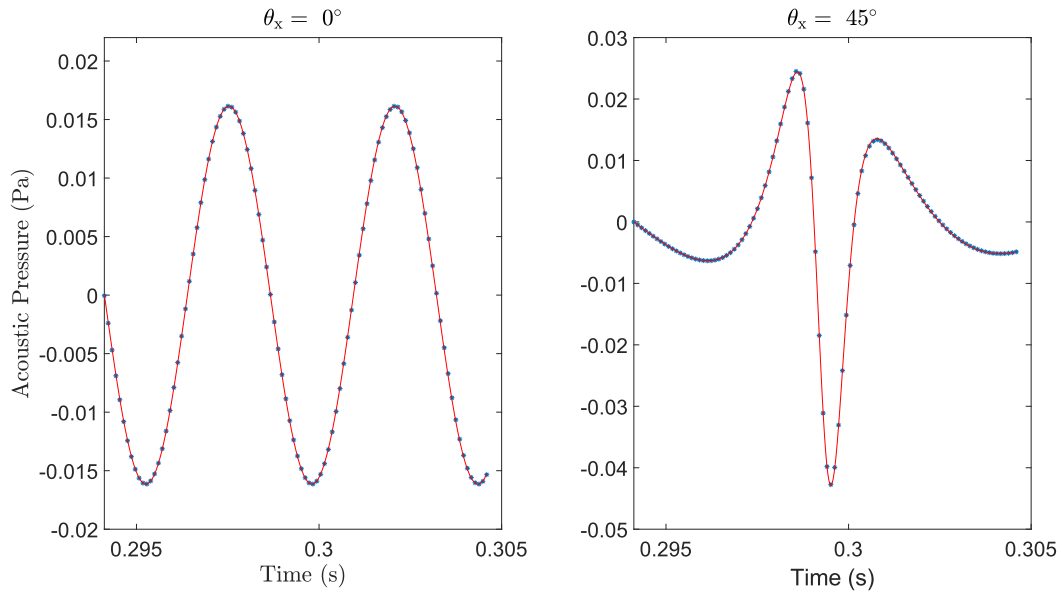
Fig. A2. 8 Comparison of the far-field pressure predicted using the time- and frequency-domain methods. For this case the force is purely axial, rotates in the positive ϕ-direction, Ω_1 = 780 rad/s, Ω_2= 600 rad/s, the force radius is 0.395 m, A = 5 N, and R_x = 100 m. The Mach number of the rotating force is 0.7. The time domain method predictions are shown using the red curve frequency domain method predictions are shown using blue stars.

Fig. A2. 9 and Fig. A2.10). plot the acoustic pressure vs time at two different observer locations for a radial (Fig. A2. 9) and a tangential (Fig. A2.10) point force rotating in the positive ϕ-direction. Aside from the orientation of the point force, the parameters used in these simulations are identical to those used to generate the results shown in Fig. A2. 6.
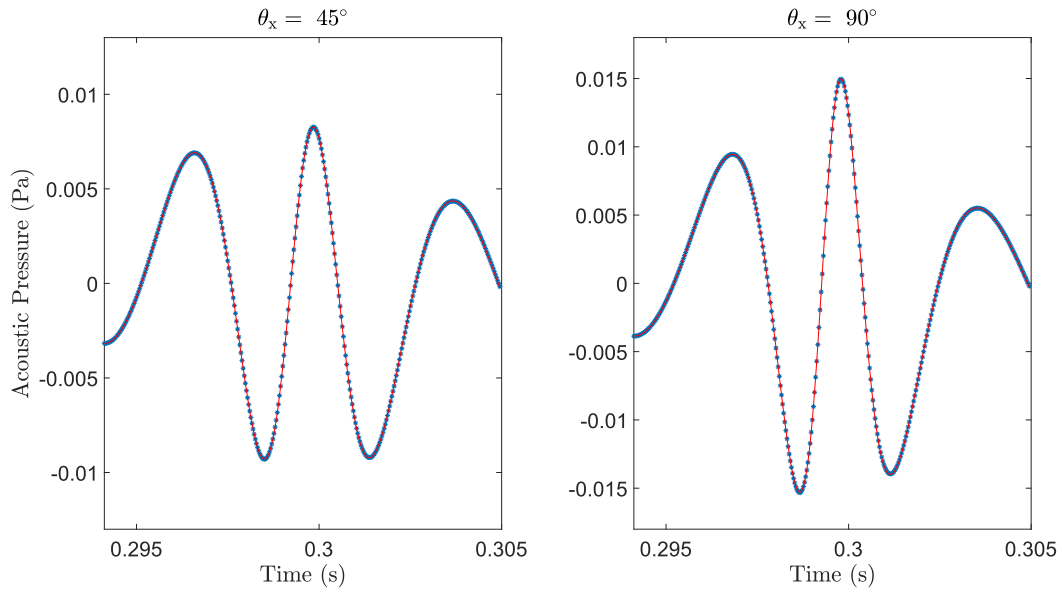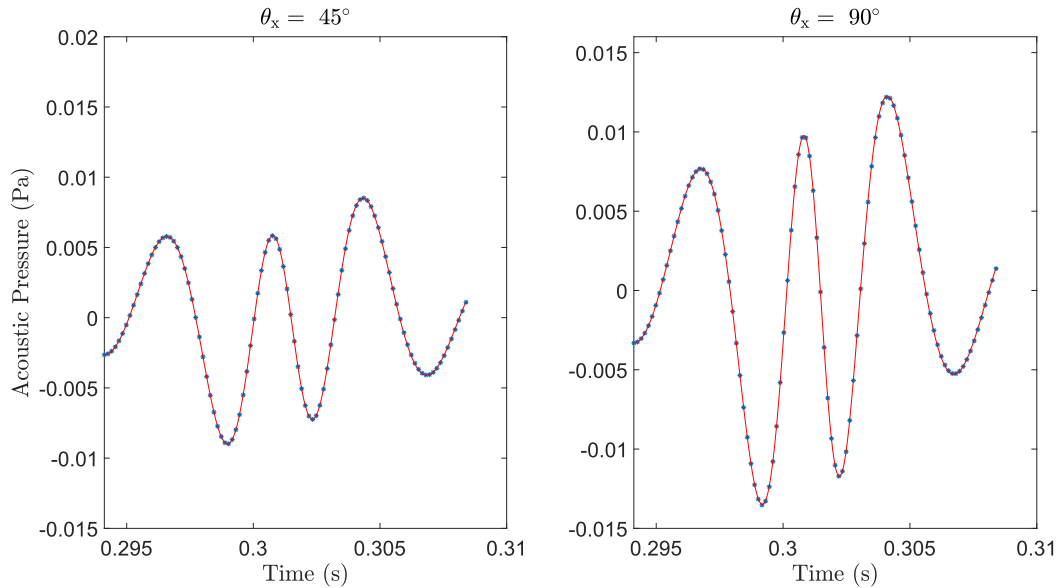

Fig. A2. 9 Comparison of the far-field pressure predicted using the time- and frequency-domain methods. For this case the force is purely radial, rotates in the positive ϕ-direction, Ω_1 = 580 rad/s, Ω_2= 440 rad/s, the force radius is 0.1905 m, A = 5 N, and R_x = 100 m. The Mach number of the rotating force is 0.2. The time domain method predictions are shown using the red curve frequency domain method predictions are shown using blue stars.
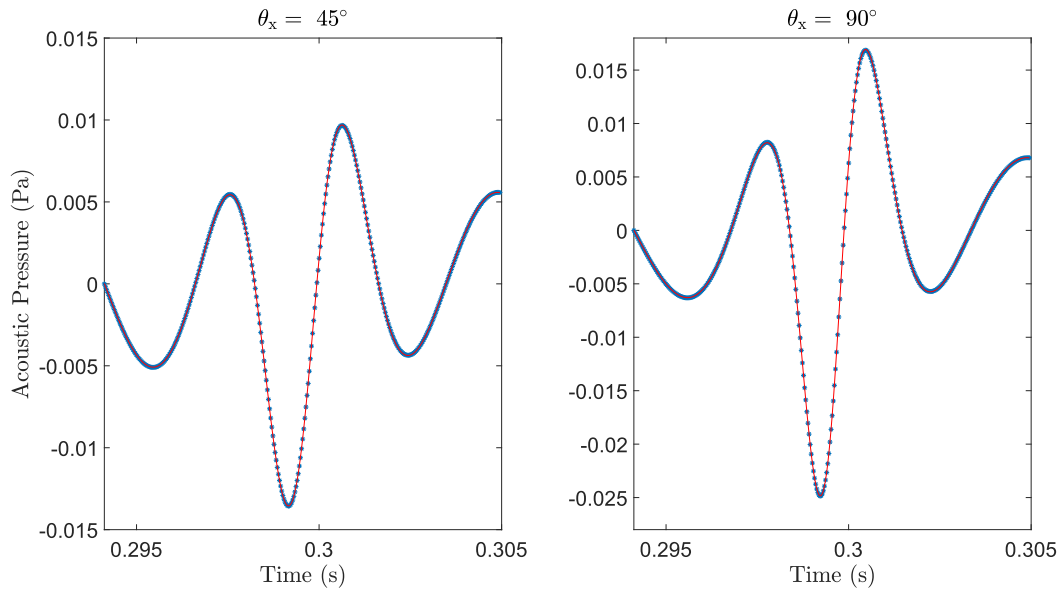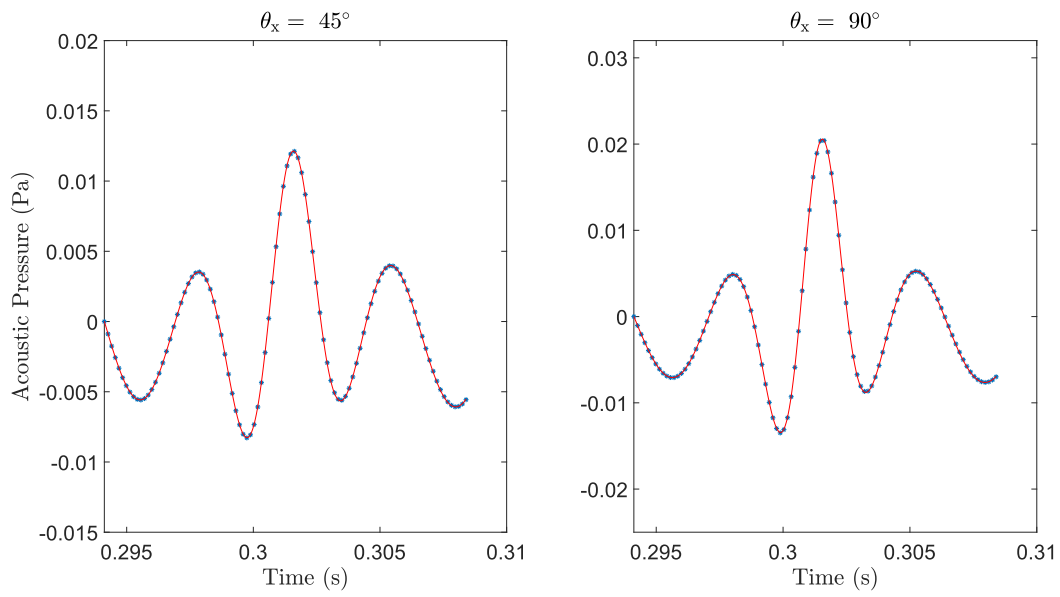
Fig. A2.10 Comparison of the far-field pressure predicted using the time- and frequency-domain methods. For this case the force is purely tangential, rotates in the positive ϕ-direction, $\Omega_1 = 580$ rad/s, $\Omega_2 = 440$ rad/s, the force radius is 0.1905 m, $A = 5$ N, and $R_x = 100$ m. The Mach number of the rotating force is 0.2. The time domain method predictions are shown using the red curve frequency domain method predictions are shown using blue stars.

3. Effect of blade skew on the noise produced by contra-rotating UAV rotor system

This chapter investigates the effect of curved, or 'skewed', blades (such as those shown in Fig. 23) on the interaction tones generated by a contra-rotating UAV rotor system. The motivation behind this idea was taken from contra-rotating open rotors, where 'sweeping' the downstream propeller blades, caused a lag between the times that the wake from an upstream propeller blade impacted on the leading-edge of a downstream propeller blade and that this in turn could produce a lag between the times at which the impulsive noise generated at different radii reached an observer location. This 'de-phasing' could result in a total acoustic pressure impulse of much lower amplitude compared to that produced by a propeller with straight blades.
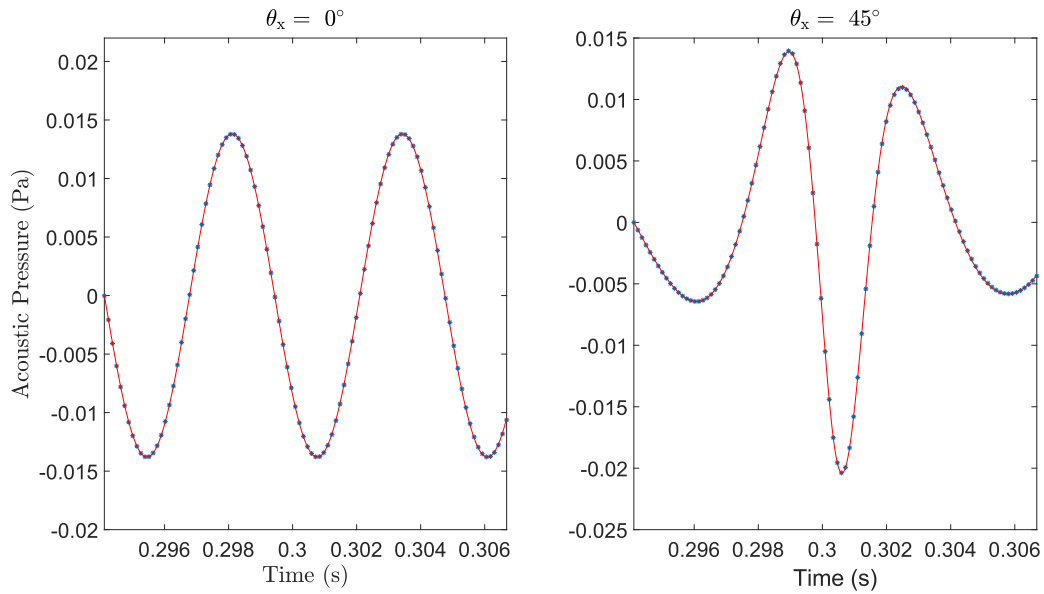
The rotor systems used here are similar to the second rotor system considered in chapter 2 which consists of two custom-made aluminium hubs with 15" diameter carbon fibre rotors attached. The hub system, the geometry of the rotors and the methods for manufacturing them are described in section 3.1. Section 3.2 briefly describes the methods used to calculate the unsteady loading on the rotor blades and the radiated acoustic field. Note that these methods are identical to those presented in chapter 2 and further details can be found therein. The procedures used to conduct the acoustical measurements are described in section 3.3 and the results of these experiments, comparisons with predictions, and analysis and discussion are presented in sections 3.4, 3.5 and 3.6 respectively. The conclusions of the chapter are presented in section 3.7.

3.1 Rotor geometry, manufacturing and operating conditions

The rotor blades used in the work described in this chapter all have a constant section profile along the blade span/radius. This profile has a chord-length of 26.6 mm, a pitch angle of 8° and a maximum thickness of 7.33 % of the chord-length. The section profile is also cambered with maximum camber of 3.76% of the chord length which is located at 55% of the chord-length from the leading edge. The rotor blades are either straight or have a curved shape which is characterised by the blade skew angle, ϕ_{skew}. The mid-chord of each blade section along the blade span lies in the same axial plane, but is located at an azimuthal angle $\phi_{\text{mid-chord}}$ given by

$$\phi_{\text{mid-chord}}(r) = \phi_i \pm \phi_{\text{skew}} \frac{(r - r_i)}{(r_t - r_i)}, \tag{60}$$

where ϕ_i is the azimuthal angle of the mid-chord at the inner radius, ϕ_{skew} is the skew angle of the blade which is defined as the magnitude of the change in azimuthal angle of the blade mid-chord between the inner radius and the tip radius, r is the radius, r_i is the inner radius (which is equal to 47.8 mm) and r_t is the tip radius (which is equal to 190.5 mm). Fig. 23 shows an illustration of a skewed blade with the skew angle, inner radius, and tip radius shown. The $\pm$ is selected depending on the direction of rotation of the rotor blade with the blade tip passing a through a fixed azimuthal angle after the inboard parts of the blade have passed through that angle.
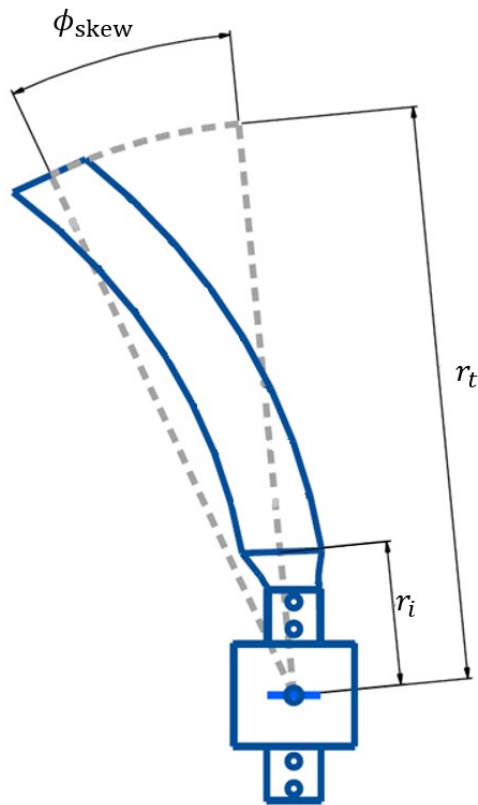
Fig. 23 Illustration of a skewed blade with the skew angle, inner radius and tip radius shown.

In this chapter, three different contra-rotating rotor systems were investigated. The first used straight blades on the top and bottom rotors with $\phi_{skew} = 0°$, whilst the second and third systems used blades with skew angles of 20° and 35° respectively. A single blade from the clockwise-rotating (viewed from above) rotor from each system is shown in Fig. 24. Note that inboard of the inner radius, these blades have a lofted section which joins to a long straight section which is clamped into a custom-built contra-rotating hub system. The hub was attached to a contra-rotating electric motor system as shown in Fig. 25. The axial separation between the rotors for all systems considered in this study was 40 mm.

$\phi_{\text{skew}} = 0°$ $\phi_{\text{skew}} = 20°$ $\phi_{\text{skew}} = 35°$
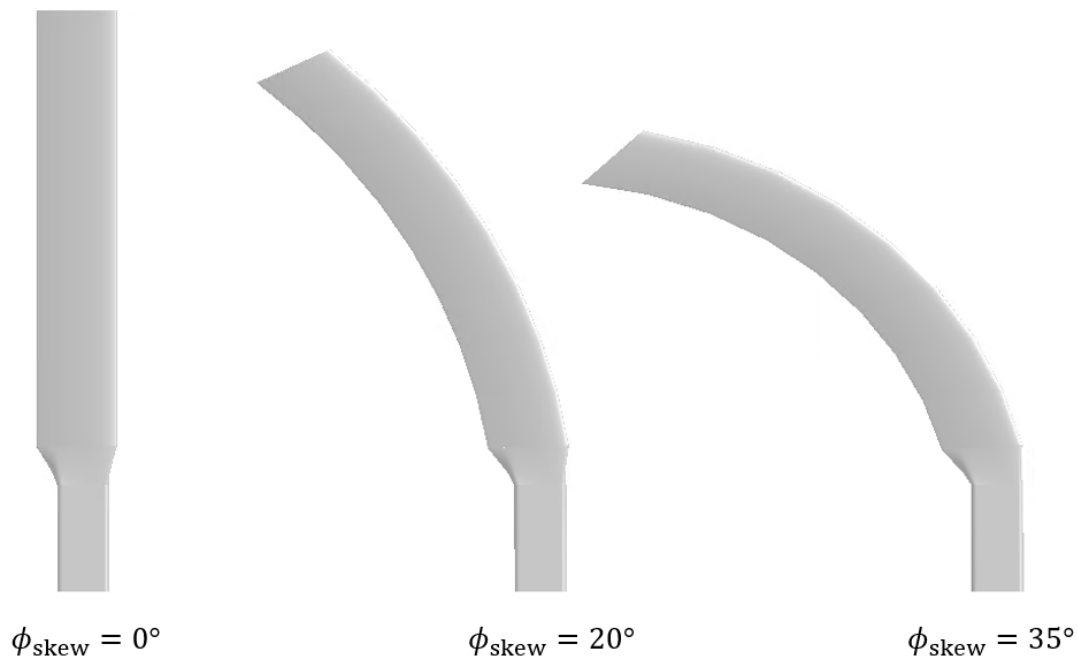
Fig. 24 Plan view of the three blade profiles investigated in this paper.
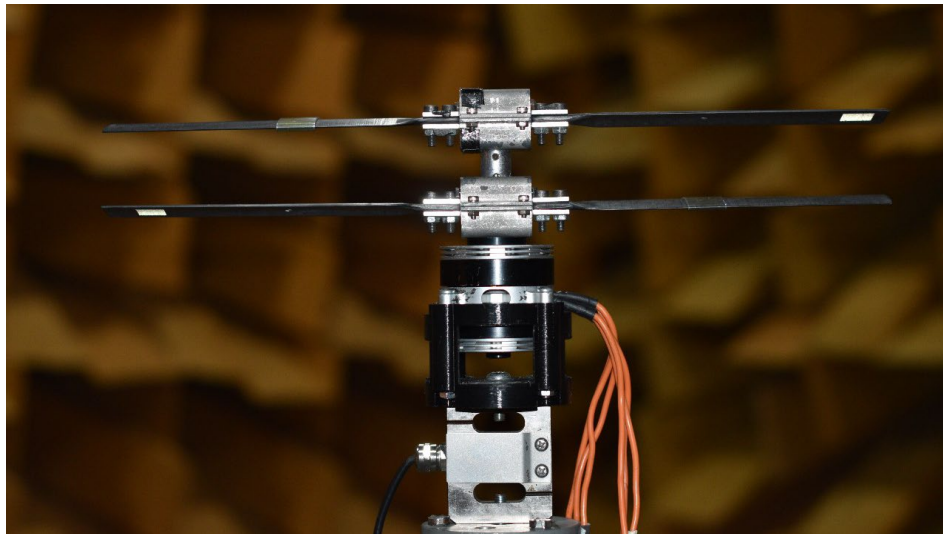
Fig. 25 Photograph of the contra-rotating UAV rotor system with straight blades mounted in the anechoic chamber at the University of Auckland.

For the experiments and simulations considered in this chapter, each rotor system was run using two different speed combinations. For the first speed combination, the top rotor rotated at 535 rad/s whilst the bottom rotor rotated at 465 rad/s. For the second speed combination, the top and bottom rotors both rotated at 500 rad/s.

Only the straight rotor blades and the blades with the 35° skew angle were manufactured and tested experimentally. Carbon fibre was selected as the primary material for the construction of the blades. Blade moulds were 3D printed using acrylonitrile butadiene styrene (ABS), with a glass transition temperature of 90℃. The moulds were in two parts, with a non-planar split line intersecting with the leading and trailing edges of the blade. All blades were manufactured using seven layers of

unidirectional (UD) epoxy carbon prepreg (Gurit SE 84LV). The laminate had the same symmetric stacking sequence, $[0/-30/+30/\overline{90}]_s$ indicating the angles at which the laminate layers were oriented Each ply was cut to match the shape of the blade in plan (as shown in Fig 2), with the exception of the centre, 90°, ply which was cut slightly oversize to help seal the mould at the split line. The fibre orientation angles of individual plies were defined relative to a reference line that was tangential to the curvature of the blade leading edge at mid radius. To create additional thickness at the blade root (for connection to the hub) 8 additional UD plies with radial orientation were added to this area only. The ABS mould halves were clamped together between 5mm steel plates. All blades were oven cured at atmospheric pressure. The curing process began at 20℃ with a ramping rate of 2 °C/min to 80 °C which was then held for 12 hours. All cured blades were post-machined in the University of Canterbury mechanical workshop to remove flash at the split line and to drill hub mounting holes. They were further polished to achieve a smooth surface finish.

3.2 Aerodynamic loading and noise radiation calculation methods

The interaction tones produced by a contra-rotating rotor system are caused by the periodic unsteady loading on the rotor blades due to their interaction with the unsteady flow field produced by the adjacent contra-rotating rotor. A noise prediction therefore requires these forces to be calculated. In this thesis this is done accurately using CFD simulations or approximately using a semi-analytical method.

The CFD simulations were conducted using the method described in [72] or in chapter 2. These simulations were run using Ansys Fluent and solved the incompressible, unsteady Reynolds-averaged Navier Stokes (URANS) equations. The pressure-based solver was used with the semi-implicit method for pressure-linked equations (SIMPLE) algorithm. The model utilised the k-ω SST turbulence model. For all simulations, the transient simulation was initialized using a solution obtained from steady calculations which used Fluent's multiple reference frame model. The transient simulations were initially run to simulate three revolutions of the top rotor using a time-step size corresponding to 1° of rotation for the top rotor per time-step. After this period, the total thrust acting on the rotors was observed to be periodic. The simulations were then run for one further revolution of the top rotor using a time-step size corresponding to 0.25° of rotation of the top rotor per time step. All simulations were run using 36 CPU cores of a Cray XC50 supercomputer.

The simulations utilised the overset mesh method [59] in which a region around the complex geometry of the rotor blades was meshed using a hexacore mesh which was surrounded by a structured background mesh. The component mesh surrounding each rotor occupied a cuboid shaped region and the mesh was refined such that the y^+ values of the closest mesh nodes to the blade surfaces was less than one. Each component mesh was superimposed onto a cylinder-shaped background mesh which rotated with the component mesh, and which had a diameter which was slightly larger than the rotor diameter. The top and bottom rotating domains were separated by a sliding mesh interface. The rotating domains were enclosed within a cylinder-shaped static domain and the static and rotating domains were also separated by a sliding mesh interface. The static domain had a diameter and height equal to two and three times the diameter of the rotors, respectively. The top surface and side of the static domain was set as a pressure inlet, whilst the bottom was set as pressure outlets.

For the rotor system with straight blades, two simulations were undertaken to simulate the two different speed combinations. The time taken to solve steady state simulations and transient simulations for both cases are shown in Table 1. For the steady state simulations, it was judged to have occurred when all of the normalised residuals had reduced to a value less than 10^{-5}. For the

transient simulations, initially solved for three revolutions of the top rotor using larger time-step size. It was judged that the forces produced on the blades of the top and bottom rotor was periodic. After, one revolution of the top rotor was solved using a smaller time-step size.

Table 1 Time taken to solve steady solution and transient solutions from CFD for different time step sizes.

Skew angle	Steady solution time	Transient solution time (3 revs, $\Delta t = 1°$ of rotation for top rotor)	Transient solution time (1 rev, $\Delta t = 0.25°$ of rotation for top rotor)
0°	17 hours	36 hours	72 hours
20°	27 hours	81 hours	59 hours
35°	17 hours	49 hours	32 hours

Grid independence studies were conducted for all simulations in order to ensure that the total unsteady loading on the rotors was independent of the number of cells used. The mesh used to simulate the rotor system with straight blades had 1.812×10^7 cells, whilst the rotor system with blades with skew angles of 20° and 35° had 1.991×10^7 and 1.622×10^7 cells respectively.

The total time-average thrust and the individual rotor time-average thrust calculated from the CFD simulations is given in Table 2. Also shown are the experimentally measured total time-average thrust values which are in reasonable agreement with the CFD results being approximately 5.5% different for the straight blade cases and 11.2% different for the 35° skewed blade case. The total thrust for 20° skewed blade was not measured, as they were not manufactured for this experiment. Note that the method for measuring the thrust experimentally is described in chapter 2.

Table 2 Time-average total thrust, and individual rotor thrust calculated from CFD simulations and measured experimentally for the different cases considered in this paper.

Case	Rotor system blade shape	Top rotor speed/ bottom rotor speed	Top rotor thrust (CFD)	Bottom rotor thrust (CFD)	Total thrust (CFD)	Total thrust (experiment)
1	Straight blades	535 rad/s / 465 rad/s	12.95 N	5.51 N	18.46 N	17.5 N
2	Straight blades	500 rad/s / 500 rad/s	10.81 N	7.65 N	18.46 N	17.4 N
3	20° skew angle	535 rad/s / 465 rad/s	12.79 N	5.53 N	18.32 N	–
4	20° skew angle	500 rad/s / 500 rad/s	10.75 N	7.69 N	18.44 N	–
5	35° skew angle	535 rad/s / 465 rad/s	11.93 N	4.79 N	16.72 N	15.0 N
6	35° skew angle	500 rad/s / 500 rad/s	10.03 N	6.84 N	16.87 N	16.0 N

The semi-analytical method described in chapter 2 is also used to calculate the blade loading for a limited number of the cases considered in this paper. This method only considers the unsteady loading caused by bound potential field interactions and is used here to demonstrate the importance of the bound potential field to the total unsteady loading on the rotor blades. The method is based on that presented in Parry [62] in which the unsteady force per unit span acting on a blade at a given radius is calculated using an equivalent two-dimensional problem. The bound potential field caused by the loading and thickness on the adjacent rotor blades is modelled as being equivalent to the loading

produced by a cascade of thin aerofoils, using standard thin aerofoil theory (with the field produced by the loading on each blade modelled using a vortex sheet placed along the blade chord-line and the field produced by the thickness of each blade modelled using a distribution of sources and sinks along the blade chord-line). The periodic velocity perturbations produced by this field are decomposed into a Fourier series and the unsteady loading/response to each Fourier harmonic is calculated using Kemp's analytical blade response function [73].

In this chapter, the acoustic radiation is calculated using the frequency-domain method described in Jung et al. [72] (which is similar to the frequency domain method presented by Hanson [8]), and this method is validated by comparison with an implementation of Farassat's formulation 1A [69,74], which is a commonly used time-domain method. The numerical implementation of both methods was verified by calculating the pressure time-histories and comparing them with one-another at many different observer locations. The frequency domain method was used to directly calculate the amplitude of specific interaction tones, and to calculate acoustic pressure time-histories (by summing the contribution of all significant interaction tones).

3.3 Experimental methods

Measurements of the noise produced by the contra-rotating UAV rotor systems were undertaken in the anechoic chamber at the University of Auckland. This anechoic chamber has internal dimensions of 5.3 m × 5.3 m × 5.3 m with a cut off frequency below 80 Hz. The contra-rotating UAV rotor system was mounted on a Honeywell Model 151 S-type load cell which was used to measure thrust as shown in Fig. 25. The rotors were driven by a contra-rotating motor system made by T-Motor which utilised two T-Motor MN501 motors. The motors ran off a 48 V power supply and were controlled using two T-Motor Alpha electronic speed controllers.

The acoustic measurements were made using G.R.A.S 46AE ½" microphones which were mounted on a C-shaped structure. The microphones were located at polar angles, θ_x, from 0° to 165° in increments of 15° as shown in Fig. 26 with the origin of the coordinate system located at the centre of the hub of the bottom rotor. The signals were acquired using a National Instruments data acquisition system which consisted of NI9234 modules in an NI cDAQ-9178 chassis. Measurements were taken over a period of 60 s at a sampling rate of 51.2 kHz. The tonal sound pressure levels calculated from these measurements were normalised to a distance of 1.5 m from the centre of the hub of the bottom rotor assuming spherical spreading.
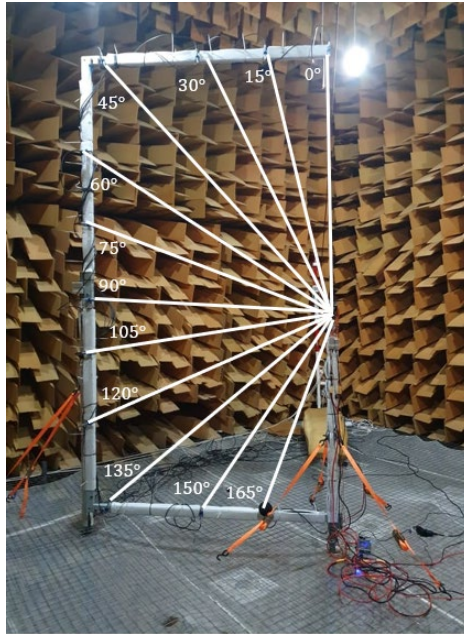
Fig. 26 Experimental setup of the rotor system with G.R.A.S 46AE ½" microphones attached to a C-shaped support structure.

3.4 Predicted unsteady blade loading

Interaction tones are produced by the unsteady loading on the blades of the contra-rotating rotors. In order to understand how the tones are generated, it is therefore useful to analyse the distribution of this loading on the rotor blades. For this purpose, the rotor blades were divided up into ten radial segments and the unsteady axial force acting on each segment was calculated from the CFD simulation results for the cases where the rotors rotated at different speeds. The average force-per-unit-span acting on each segment was then calculated by dividing by the segment length. The semi-analytical model was also used to calculate the axial force-per-unit-span acting on the blades at 22 radial stations across the span. Contours of the axial force-per-unit span (denoted as F_x), acting on each segment of the top and bottom rotor reference blades calculated from these results are plotted against radius (vertical axis) and time (horizontal axis) for all three rotor systems in Fig. 27 and Fig. 28. Fig. 27 presents the results for the top rotor reference blades with the CFD results shown on the left and the semi-analytical model results shown on the right. The straight-blade results are shown in the top plots and the 20° and 35° skew angle blade results are, respectively, shown in the middle and bottom plots. There is reasonable qualitative agreement between the semi-analytical model results and the CFD simulation results. The times at which the mid-chords of the top and bottom blades pass over each other are shown using red dashed lines on each plot. The impulsive loading due to the bound potential field interactions occurs close to these times. For the straight blades, the maximum and minimum loading occurs at approximately the same time along the blade span. As the skew angle increases, the times at which these peaks in the blade loading occur varies more across the blade span due to the change in the times that the blades pass over each other at a given radius.

Fig. 28 presents the corresponding results for the bottom rotor reference blades. As expected, there are differences between the CFD simulations (left) and the semi-analytical model results (right) because the CFD simulations include the effect of the tip vortices from the top rotor interacting with the

bottom rotor blades, whereas the semi-analytical model only models the bound potential field interactions. This tip vortex interaction produces unsteady loading on the outer portion of the blade. The approximate times at which the vortex region impinges on the blade are shown by the black ellipses. These times were estimated by visualising the tip vortex using an iso-surface of constant lambda-2 criterion and observing when this iso-surface was in contact with the bottom rotor reference blade at each radius. For these cases, the impingement of the tip vortex region (which is from the preceding top rotor blade) occurs during the times when the outboard portions of the top and bottom rotor reference blades pass over each other and is centred at a radius of approximately $0.83r_t - 0.92r_t$ due to the strong stream-tube contraction through the rotor system which causes the tip vortex to migrate radially inwards. A significant increase in the magnitude of the unsteady blade loading is observed at times and radii close to those at which the tip vortex region is in contact with the downstream rotor blade. At radii inboard of $0.75r_t$, the unsteady loading calculated from the CFD simulations appears qualitatively similar to the semi-analytical model results – with the peak loading occurring at times close to the times where the mid-chords of the top and bottom rotor reference blades pass over each other. This suggests that the loading at these radii is predominantly caused by the bound potential field interactions.
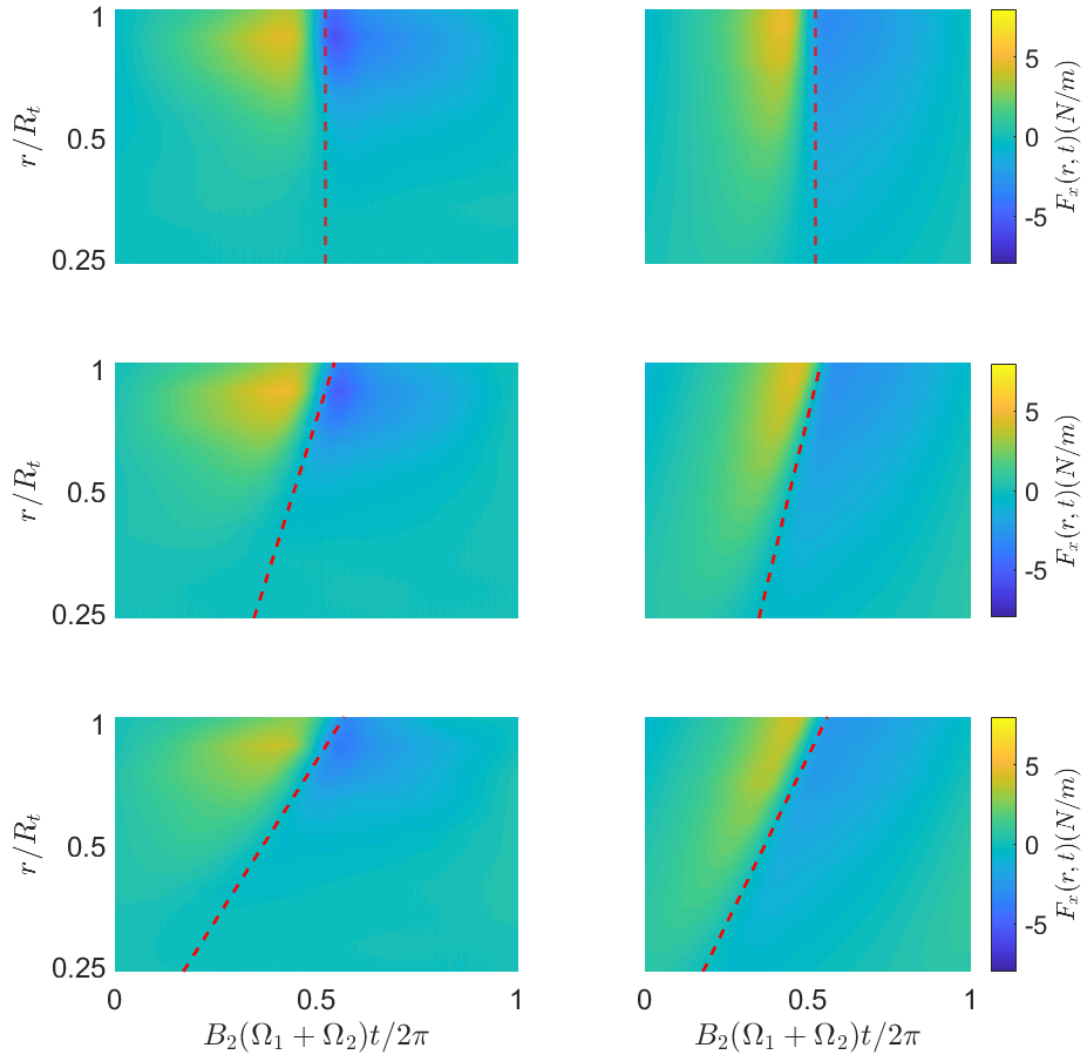
Fig. 27 Contours of unsteady axial loading on the top rotor reference blade versus normalised radius (*y*-axis) and normalised time (*x*-axis). The results from the CFD simulations are shown in subplots on the left which show results for blades with $\phi_{\text{skew}} = 0°$, 20° and 35° respectively. Subplots on the right present the results calculated using the semi-analytical models for blades with $\phi_{\text{skew}} = 0°$, 20° and 35° respectively. The dashed red lines show the times at which the mid-chords of the top and bottom reference blades pass over each other.

(d)
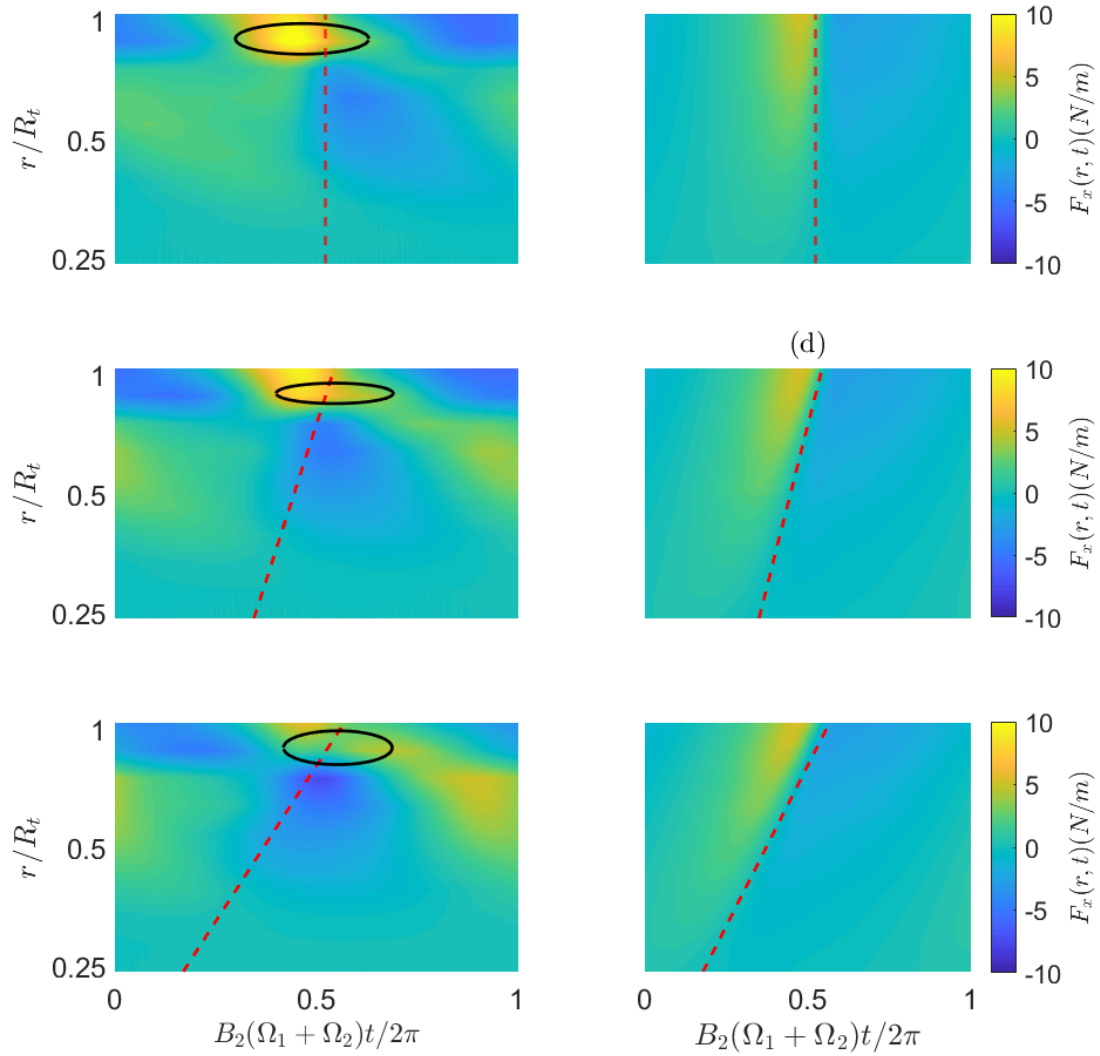
Fig. 28 Contours of unsteady axial loading on the bottom rotor reference blade versus normalised radius (*y*-axis) and normalised time (*x*-axis). The results from the CFD simulations are shown in subplots on the left which shows results for blades with $\phi_{\mathrm{skew}} = 0°$, $20°$ and $35°$ respectively. Subplots on the right present the results calculated using the semi-analytical models for blades with $\phi_{\mathrm{skew}} = 0°$, $20°$ and $35°$ respectively. The dashed red lines show the times at which the mid-chords of the top and bottom reference blades pass over each other. The black ellipses show an estimate of the times where the tip vortex core is in contact with the bottom reference blade.

3.5 Tone noise radiation

In this section, the measured and predicted sound pressure levels of individual interaction tones are presented. Each interaction tone occurs at a frequency (in Hz) given by $f = n_1 \text{BPF}_1 + n_2 \text{BPF}_2$, where BPF_1 and BPF_2 are, respectively, the blade-passing frequencies of the top and bottom rotors, and n_1 and n_2 are integers. In the discussion which follows, individual interaction tones will be denoted by the value of n_1 and n_2. For example, the first interaction tone will be denoted as the $\{n_1 = 1, n_2 = 1\}$ interaction tone, or just the $\{1,1\}$ interaction tone. Fig. 29 plots the narrow-band sound pressure level (SPL) measured at the microphone located at $\theta_x = 0°$ (on-axis) for case 1 in table 1 (the rotor system with the straight blades and the rotors operating at different speeds). Also shown (as red solid circles) are the sound pressure levels for each interaction tone which were calculated by integrating the power spectral density over the bandwidth of each tone. This was necessary as the energy associated with each interaction tone was spread over a small band of frequencies surrounding the nominal tone frequency calculated from the nominal motor speed. Each interaction tone present in the spectrum is also labelled. Note that for this case, as the observer is located on the rotor axis, only interaction tones for which $n_1 = n_2$ radiate efficiently and are thus clearly visible in the spectrum (see refs. [3 and 4] for more details).
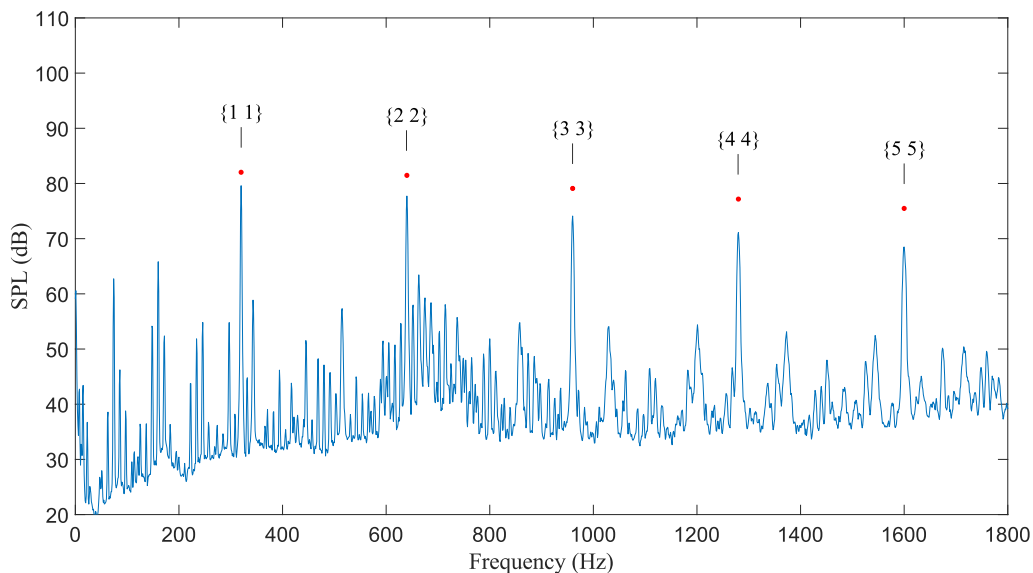
Fig. 29 Experimentally measured sound pressure level spectrum produced by the rotor system with the straight blades and the rotors operating at different speeds at $\theta_x = 0°$. The top rotor rotated at 535 rad/s and the bottom rotor rotated at 465 rad/s. The narrow-band spectrum (1 Hz bandwidth) is shown in blue, whilst the tonal levels are denoted by red circle markers.

Fig. 30 plots the measured and predicted sound pressure level polar directivity for six different interaction tones produced by the rotor system with the straight blades operating with the rotors running at different speeds. These predictions were made using the loading data taken from the CFD simulations. The agreement between the predictions and the measurements is very good with the predictions and measurements clearly showing the lobes in the directivity of each tone.
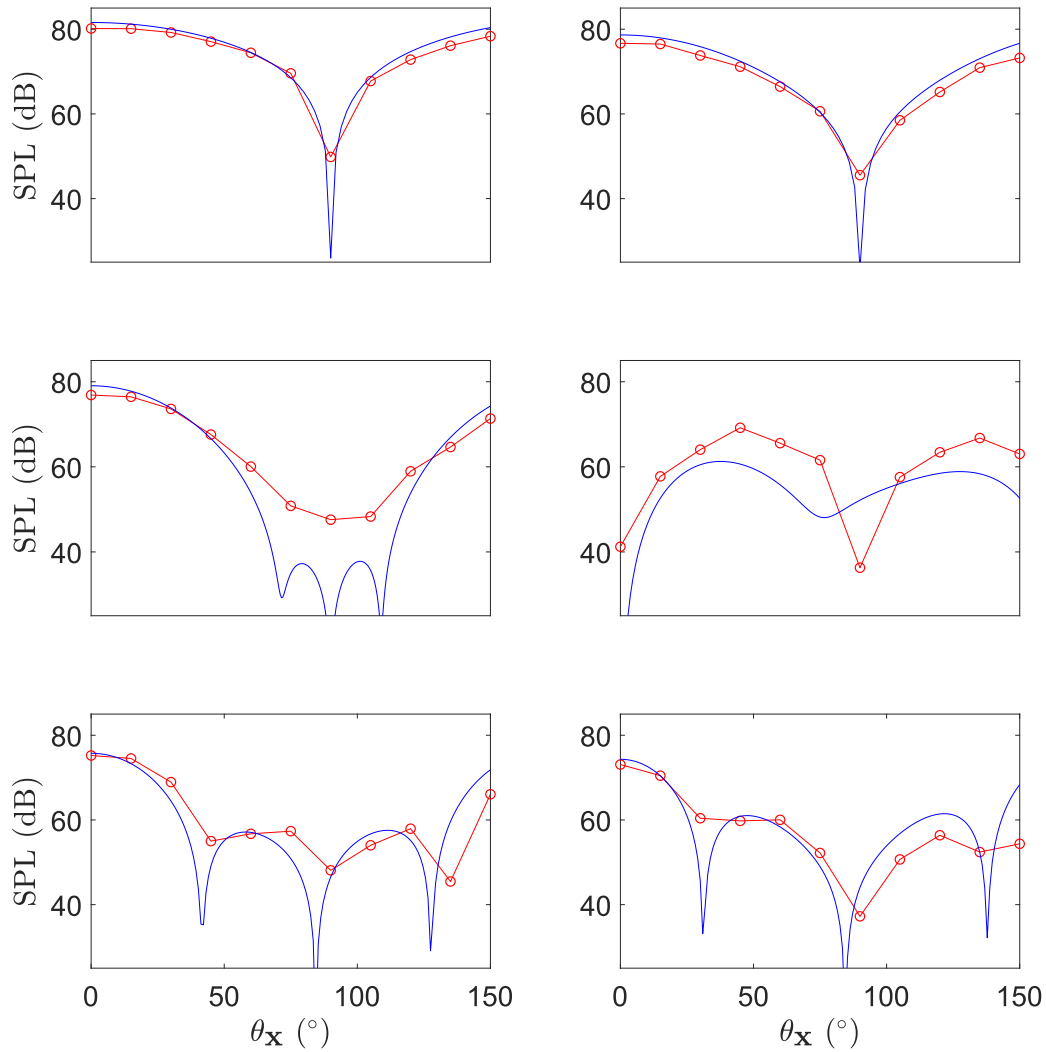
Fig. 30 Sound pressure level polar directivity of six different interaction tones produced by the rotor with straight blades and the rotors operating at different speeds. The top rotor rotated at 535 rad/s and the bottom rotor rotated at 465 rad/s. Experimental measurements (red lines with circle markers), numerical predictions (blue curves). $\{1, 1\}$ tone top-left, $\{2, 2\}$ tone top right, $\{3, 3\}$ tone middle left, $\{4, 3\}$ tone middle right, $\{4, 4\}$ tone bottom left and $\{5, 5\}$ tone bottom right.

Fig. 31 plots the measured and predicted sound pressure level polar directivity for interaction tones produced by the rotor system with the skewed blades ($\phi_{skew} = 35°$) operating with the rotors running at different speeds (case 5 in Table 2). Once again, the agreement between the measurements and the predictions is very good with both the measurements and predictions clearly capturing the prominent lobes in the directivity pattern of each tone.
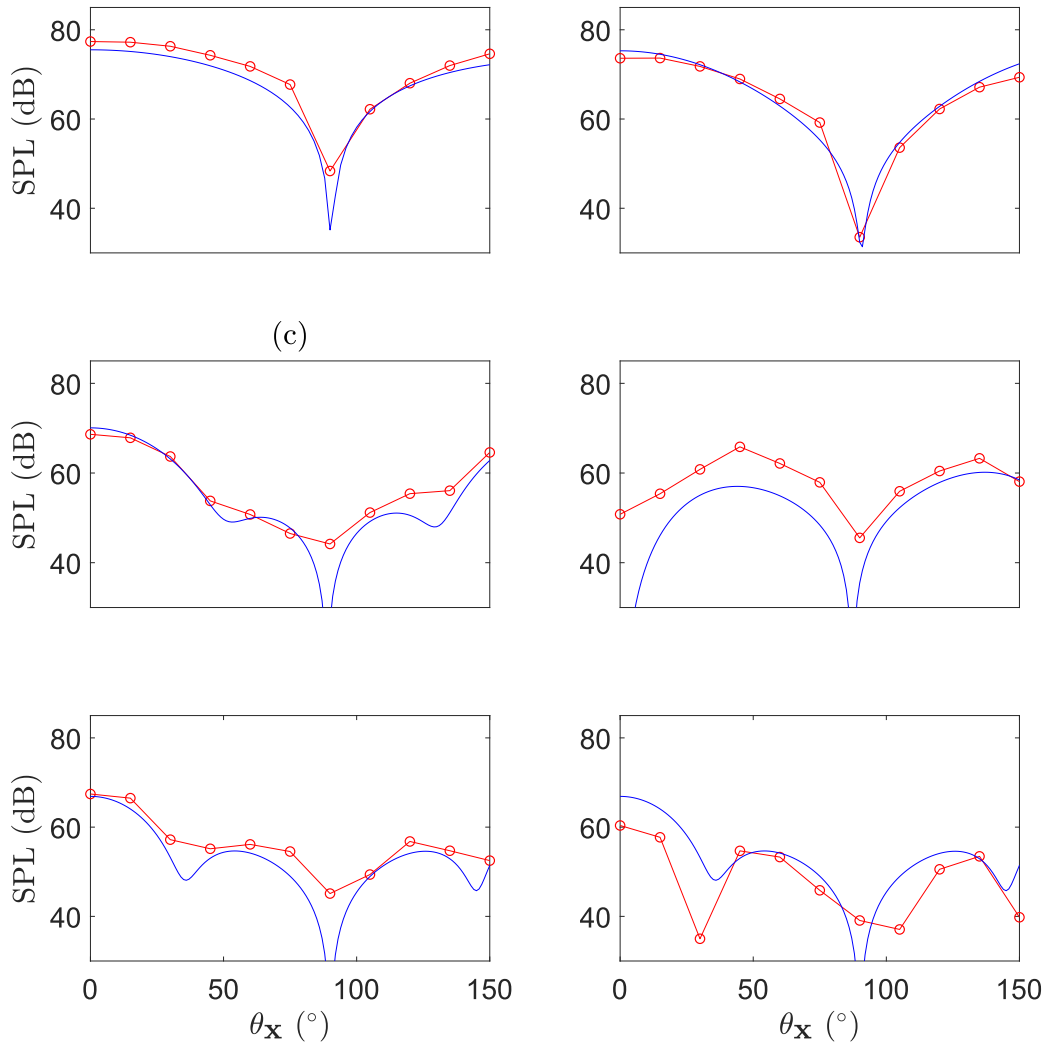
Fig. 31 Sound pressure level polar directivity of three different interaction tones produced by the rotor with the skewed blades ($\phi_{\text{skew}} = 35°$) operating with the rotors running at different speeds. The top rotor rotated at 535 rad/s and the bottom rotor rotated at 465 rad/s. Experimental measurements (red lines with circle markers), numerical predictions (blue curves). $\{1, 1\}$ tone top-left, $\{2, 2\}$ tone top right, $\{3, 3\}$ tone middle left, $\{4, 3\}$ tone middle right, $\{4, 4\}$ tone bottom left and $\{5, 5\}$ tone bottom right.

Fig. 32 plots the sound pressure levels of prominent interaction tones produced by the different rotor systems operating with the rotors running at different speeds (cases 1, 3 and 5 in Table 3) at an observer located at a polar angle of 0°. Measurements and predictions are shown, although recall that no experiments were performed for a rotor system with skewed blades with a skew angle of 20°. It is observed that at this location, the level of each interaction tone decreases significantly as the skew angle increases.

58
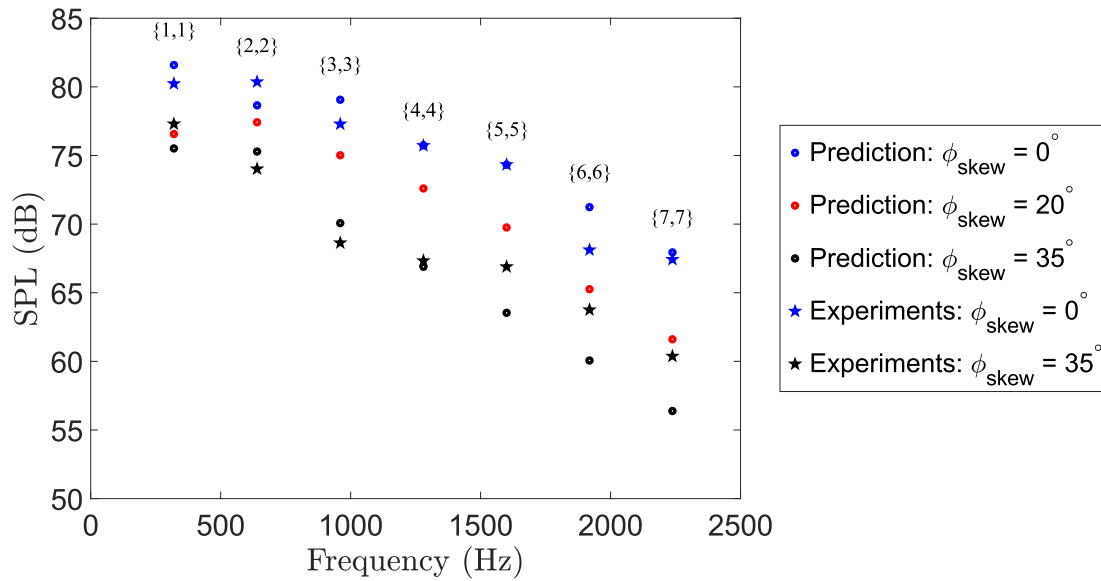
Fig. 32 Sound pressure level versus frequency for interaction tones produced by the rotor systems with blades with $\phi_{\text{skew}} = 0°$ (blue), 20° (red) and 35° (black) at $\theta_x = 0°$. The top rotor rotated at 535 rad/s and the bottom rotor rotated at 465 rad/s. Measurements are denoted by the solid pentagrams whilst the predictions are denoted by the circles.

Fig. 33 plots the measured and predicted sound pressure levels of the first three, and most prominent, interaction tones produced by the different rotor systems at an observer location with a polar angle of 45°. The comparison between the measured and predicted levels shows very good agreement. As was observed in the results presented in Fig. 32, the level of the interaction tones decreases as the skew angle increases.
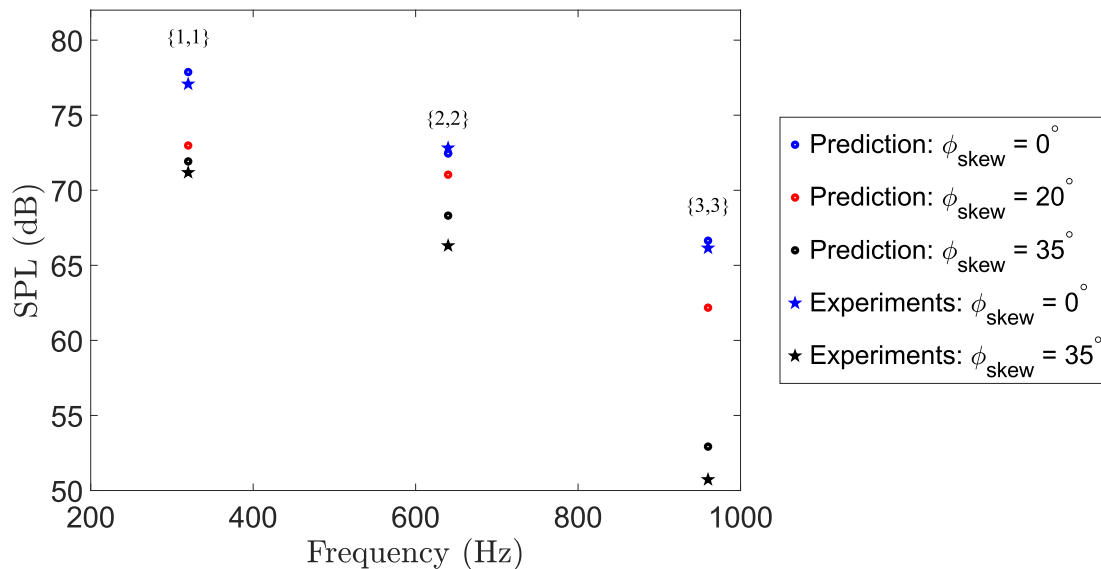
Fig. 33 Sound pressure level versus frequency for interaction tones produced by the rotor systems with blades with $\phi_{\text{skew}} = 0°$ (blue), 20° (red) and 35° (black) at $\theta_x = 45°$. The top rotor rotated at 535 rad/s and the bottom rotor rotated at 465 rad/s. Measurements are denoted by the solid pentagrams whilst the predictions are denoted by the circles.

The predicted sound pressure level polar directivity pattern of six prominent interaction tones produced by the three different rotor systems is shown in Fig. 34 for the cases where the rotor systems

operate with the rotors running at different speeds (cases 1, 3 and 5 in Table 3). For the {1,1} and {2,2} interaction tones, the sound pressure level decreases as the skew angle increases at all observer locations. The sound pressure level of the {3,3} interaction tone decreases as the skew angle increases for polar angles close to the axis of the rotors, however, near the plane of the rotors, a null in the directivity of the rotor with the straight blades results in the levels of the tones produced by the other rotor systems being higher at those angles – although the level of the tones at these locations is significantly lower than the levels predicted close to the axis for all rotor systems. The directivity of the {4,3} tone is different to those of the other tones shown in Fig. 34 – with no sound radiation along the rotor axis, a null close to the rotor plane and peak levels occurring at intermediate angles. The {4,3} tone produced by the rotor system with blades with a skew angle of 20° produces the lowest sound pressure levels at polar angles less than 85°, but is then highest at angles greater than 100°. Conversely, the {4,3} tone produced by the rotor system with straight blades produces the highest sound pressure level at angles less than 100°, but this tone has the lowest level at angles greater than 110°. Similar to the {1,1} and {2,2} interaction tones, the {4,4} and {5,5} interaction tones radiate strongly along the rotor axis. However, these tones have three nulls in the directivity pattern with the strongest null occurring close to the plane of rotation where the sound pressure level is lowest. At angles close to the rotor axis and before the first null, increases in the skew angle reduce the sound pressure level. The slightly different locations of the nulls make a comparison between the different rotor systems difficult at the intermediate polar angles. However, the peak sound pressure levels between the nulls are lowest for the rotor system with the largest skew angle.
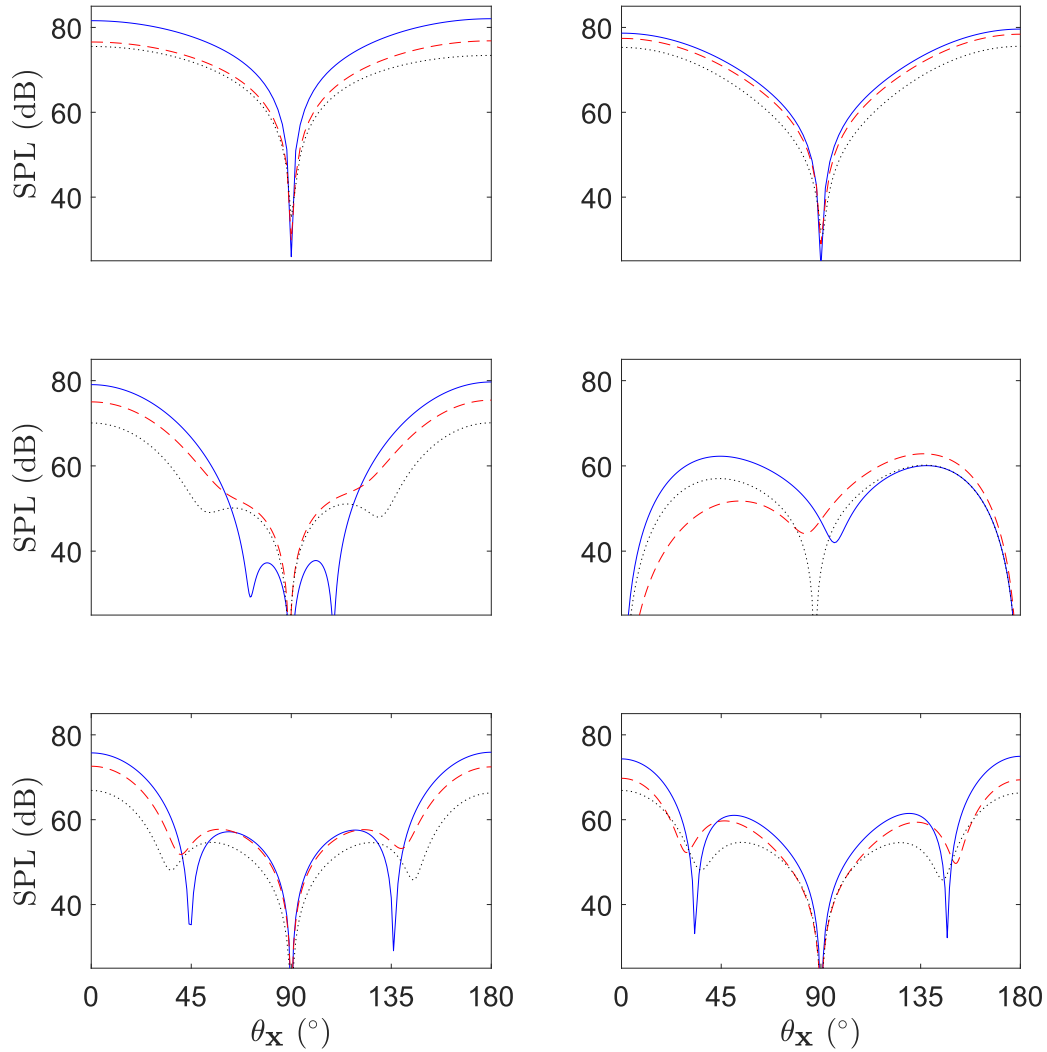
Fig. 34 Predicted sound pressure level polar directivity for six different interaction tones produced by the three different rotor systems operating with the rotors running at different speeds. The top rotor rotated at 535 rad/s and the bottom rotor rotated at 465 rad/s. Rotor system with straight blades (blue curve), $\phi_{\text{skew}} = 20°$ (dashed red curve) and $\phi_{\text{skew}} = 35°$ (dotted black curve). $\{1, 1\}$ tone top-left, $\{2, 2\}$ tone top right, $\{3, 3\}$ tone middle left, $\{4, 3\}$ tone middle right, $\{4, 4\}$ tone bottom left and $\{5, 5\}$ tone bottom right.

Fig. 35 and Fig. 36 presents comparisons of the predicted and measured sound pressure level spectra at $\theta_{\mathbf{x}} = 0°$ for the cases where the rotors were run at the same speeds and for which experimental data was available (i.e. cases 2 and 6 in Table 1). Because for these cases, both rotors had the same speed, each interaction tone contained contributions from multiple harmonics (e.g. the second interaction tone contains contributions from the {1,3}, {2,2} and {3,1} harmonics). For these cases, the interaction tones are simply referred to by one of the contributing harmonics (e.g. the second interaction tone is referred to as the {2,2} interaction tone). Fig. 35 presents data for the rotor system with the straight blades and Fig. 36 presents data for the rotor system with the skewed blades ($\phi_{\text{skew}} = 35°$). The plots show the measured narrow-band levels, the levels calculated by integrating the measured spectrum across the band-width of each interaction tone and the level predicted using the loading data taken

61

from the CFD simulations. The agreement between measured and predicted sound pressure levels produced by the straight blades is excellent with the predicted sound pressure levels being within 2 dB for all interaction tones shown in Fig. 35. Similarly, there is good agreement between the predicted and measured tone levels for the results shown in Fig. 36 – except for the second ({2,2}) and fifth ({5,5}) tones (where the difference is approximately 7 dB and 4 dB respectively).
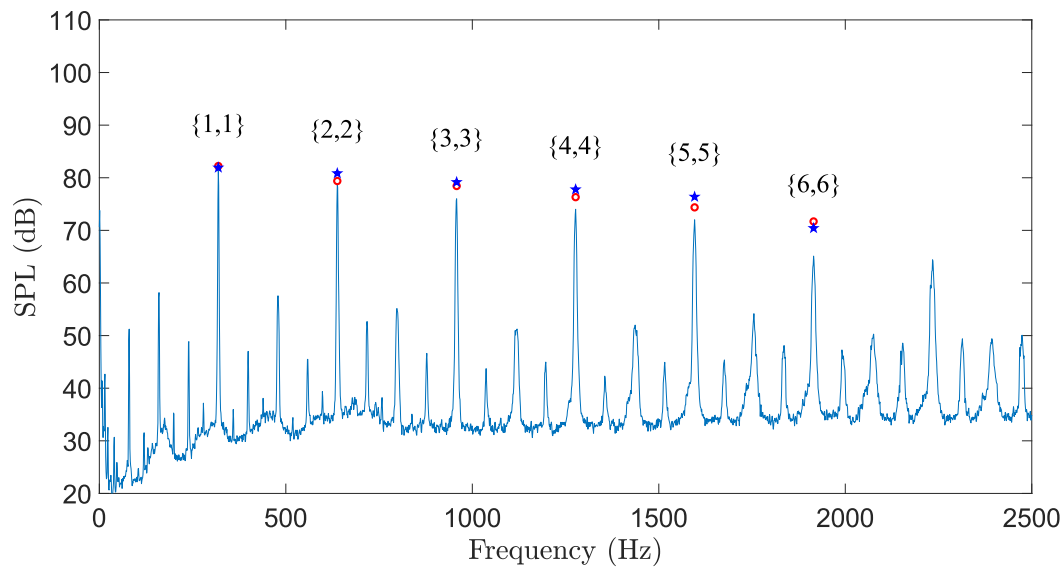
Fig. 35 Sound pressure level spectrum at $\theta_x = 0°$ produced by the rotor system with the rotors running at the same speed and with straight blades. The top and bottom rotor rotated at 500 rad/s. The narrow-band (1 Hz bandwidth) spectrum is shown in blue and the tonal levels calculated by integrating the measured spectrum over the tone bandwidth are denoted by the blue pentagram markers. The predicted tonal sound pressure levels are denoted by the red circle markers.
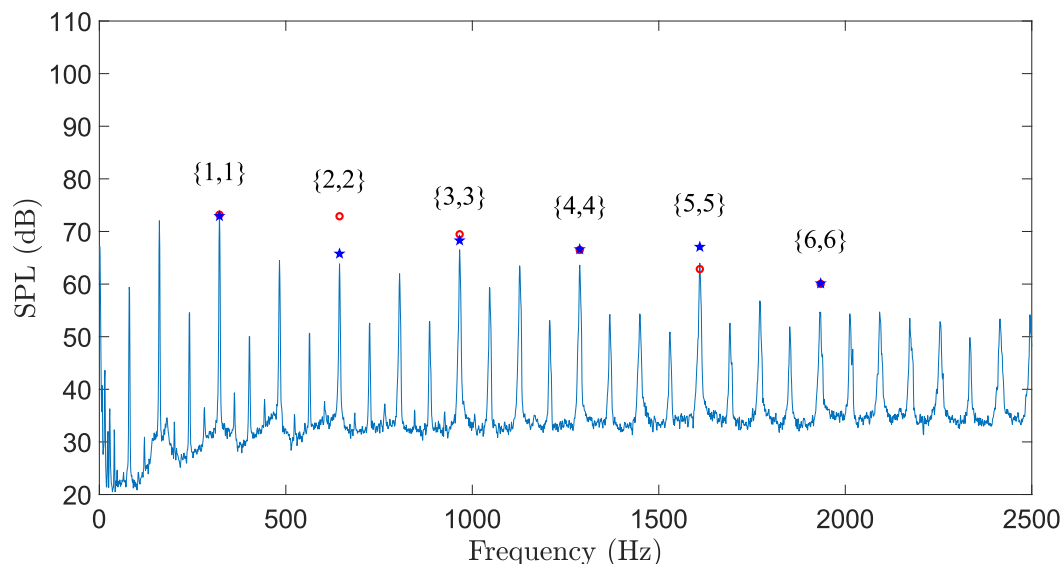
Fig. 36 Sound pressure level spectrum at $\theta_x = 0°$ produced by the rotor system with the rotors running at the same speed and with skewed blades ($\phi_{skew} = 35°$). The narrow-band (1 Hz bandwidth) spectrum is shown in blue and the tonal levels calculated by integrating the measured spectrum over the tone bandwidth are denoted by the blue pentagram markers. The predicted tonal sound pressure levels are denoted by the red circle markers.

The predicted sound pressure level polar directivities of six interaction tones produced by the different contra-rotating UAV rotor systems with the top and bottom rotors operating at the same speed are

shown in Fig. 37. As the skew angle increases, the sound pressure level decreases at most observer locations for the first four interaction tones (the {1,1}, {2,2}, {3,3} and {4,3} interaction tones), although the null close to the plane of the rotor occurs at slightly different angles for each rotor system – which affects the relative levels at angles close to these locations. For the {4,4} and {5,5} interaction tones, the sound pressure levels decrease as the skew angle increases near the rotor axis (i.e., $0 < \theta_x < 30°$ and $150° < \theta_x < 180°$). However, the different locations of the nulls in the directivity patterns away from the rotor axis make a comparison between the levels produced by the different rotor systems difficult at these angles. It should be noted that the sound pressure levels at these locations are significantly lower than those close to the rotor axis.
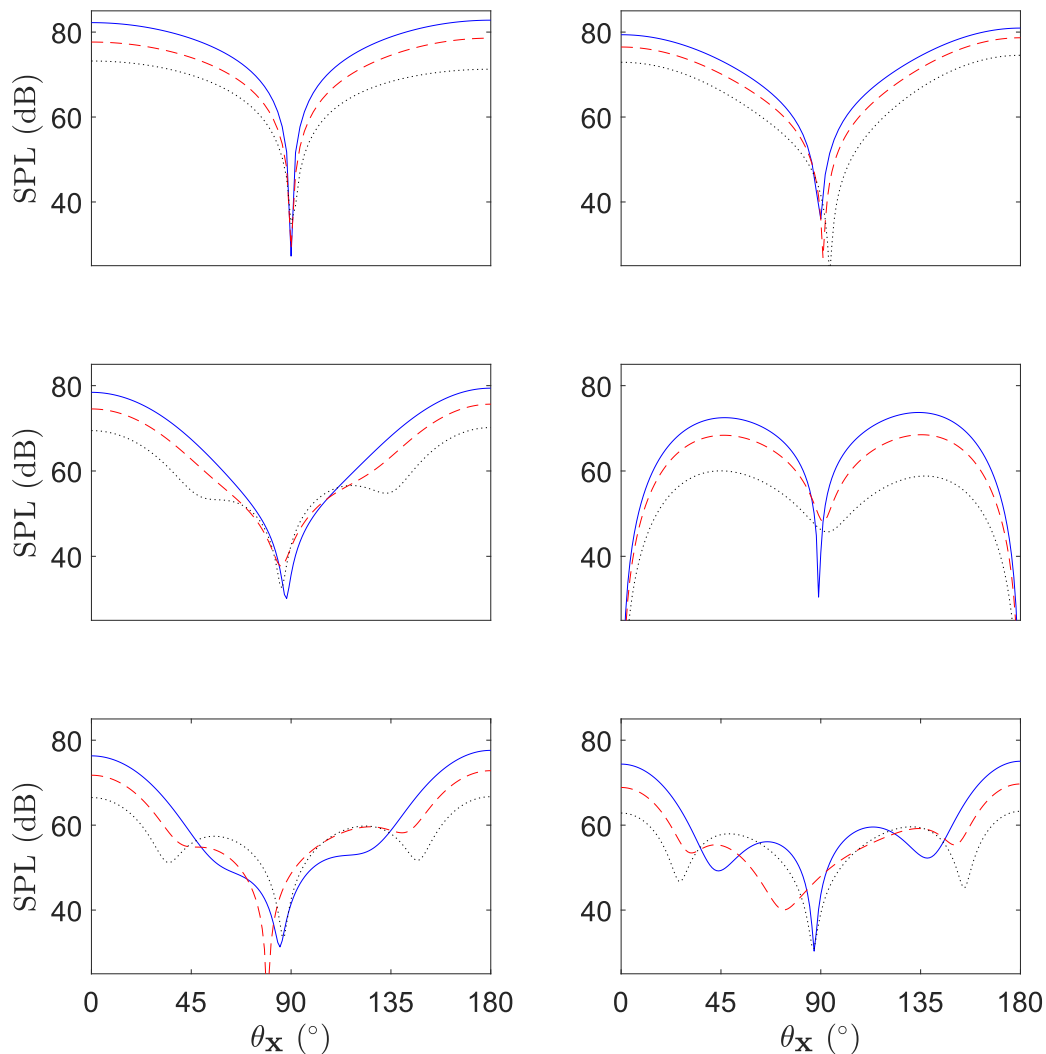
Fig. 37 Predicted sound pressure level polar directivity for six different interaction tones produced by the three different rotor systems with both rotors running at the same speed. These predictions were made at a fixed azimuthal angle. The rotor system with straight blades (blue curve), blades with $\phi_{skew} = 20°$ (dashed red curve) and blades with $\phi_{skew} = 35°$ (dotted black curve). $\{1, 1\}$ tone top-left, $\{2, 2\}$ tone top right, $\{3, 3\}$ tone middle left, $\{4, 3\}$ tone middle right, $\{4, 4\}$ tone bottom left and $\{5, 5\}$ tone bottom right.

The results presented above show that the sound pressure levels of the prominent interaction tones produced by the rotor systems with the skewed blades are, in general, lower in level compared to those produced by the rotor system with the straight blades and that the levels of the interaction tones produced by the rotor system with the largest skew angle were generally the lowest. However, an assessment of the effect of blade skew on the overall tonal sound pressure level and sound power level is also necessary to establish that the skewed blades do produce lower noise levels in general. To that end, the overall A-weighted sound pressure produced by the rotor systems operating at the same speeds was calculated at observer locations spaced over a sphere enclosing the rotors at every 5 degrees in the polar and azimuthal directions. These calculations were performed using the time-domain noise prediction method with loading data taken from the CFD simulations. The time-domain acoustic pressure was then A-weighted by passing it through a digital filter and the A-weighted mean-square pressure at each observer location was calculated. The A-weighted mean-square pressure was then averaged over the azimuthal angle and this was used to calculate an average A-weighted sound pressure level. The results of this calculation are shown in Fig. 38 which plots the average A-weighted sound pressure levels against polar angle for the three different rotor systems. As expected, the average sound pressure level is the strongest along the axis of the rotor and weakest close to the plane of the rotor for all rotor systems and it is observed that as the skew angle increases, the average sound pressure level decreases at all polar angles. Additionally, these predictions were used to estimate the A-weighted sound power. This was done by converting the A-weighted mean-square pressures to A-weighted time-average acoustic intensity in the radial direction (assuming spherical spreading), and then integrating the intensity over the spherical surface using a 2D numerical integration routine. The A-weighted sound power levels calculated using this approach were 92.8 dB for the rotor system with the straight blades, and 89.5 dB and 84.1 dB respectively for the rotor systems with the blades with skew angles of 20° and 35°. These results show an impressive 8.7 dB reduction in the A-weighted sound power level produced by the rotor system with the highly skewed blades compared with that produced by a rotor system with straight blades. An analysis of the cases where the rotor blades were run at different speeds is not included here as the calculation times required to accurately calculate mean-square pressures at each observer location were prohibitively long.
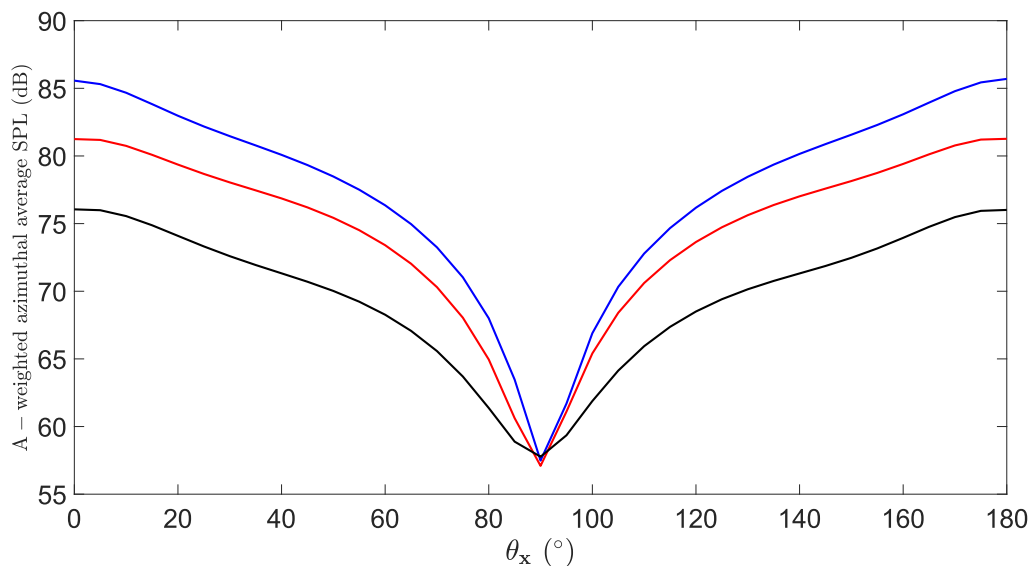

Fig. 38 Overall azimuthal average A-weighted tonal sound pressure level vs polar angle produced by the contra-rotating rotor systems at a spherical radius of 1.5 m. Level produced by the rotor system with blades with $\phi_{\text{skew}} = 0°$ (blue), 20° (red) and 35° (black).

3.6 Noise reduction mechanism investigation

The results presented above clearly show that the rotor systems with skewed blades, in general, produce lower interaction tone noise levels. In this section, the reasons for this noise reduction are explored using predictions of the radiated acoustic pressure made using the loading data from the CFD simulations.

The theoretical analysis of Kingan & Parry [24] noted that the interaction of the downstream propeller blades of a contra-rotating propeller system with the wakes from the upstream propeller produced impulsive loading and subsequently impulsive noise. They showed that sweeping the blades of the downstream propeller produced a delay in the time at which the wake impinged on the downstream blades at a particular radius and a corresponding delay in the impulsive noise radiated from that location. By selecting a sweep profile which ensured that the trace speed of the wakes across the leading edge of the downstream propeller blades was subsonic, the peak impulsive pressure emitted from different radii of the same blade could not arrive at the same time at any observer location. They also noted that the blade sweep could reduce the magnitude of the unsteady loading on the propeller blades. These effects produced a total acoustic pressure impulse which was less impulsive, and which had a lower peak pressure, than that produced by an equivalent straight-bladed propeller at all possible observer locations. For the contra-rotating UAV rotor systems considered here, the primary noise generation mechanism is not the wake from the top rotor impinging on the bottom rotor, but rather the bound potential field interactions which occur as the blades pass over one another. This is slightly different to the wake interaction mechanism for which the wake is typically very narrow and convects with the flow between the propellers. The bound potential field flow disturbances are instead 'bound' to the blades of the rotors and the magnitude of the disturbances decays away from the blade locations. Nevertheless, as shown in §5.1, these bound potential field interactions do produce impulsive loading as the blades pass over each other. Therefore, by skewing the rotor blades, this impulsive loading should be 'de-phased' along the blade span – reducing the amplitude of the total acoustic impulse radiated from the blade with each interaction. In order to try and maximise this effect, the time-lag between impulses radiated from different radii should be as large as possible. This can be achieved by minimising the speed at which the point where the mid-chords of the blades pass over each other moves (and ensuring that this speed is subsonic).

The azimuthal angle of the mid-chord of the reference blade on the top rotor (which rotates in the negative ϕ direction at speed Ω_1) is given by

$$\phi_{\text{mid-chord},1}(r) = -\Omega_1 t + \phi_{i,1} + \phi_{\text{skew}} \frac{(r-r_i)}{(r_t-r_i)},$$ (61)

where t is time and a subscript 1 is used to denote quantities associated with the top rotor. Similarly, the azimuthal angle of the mid-chord of the reference blade on the bottom rotor (which rotates in the positive ϕ direction at speed Ω_2) is given by

$$\phi_{\text{mid-chord},2}(r) = \Omega_2 t + \phi_{i,2} - \phi_{\text{skew}} \frac{(r-r_i)}{r_t-r_i},$$ (62)

where a subscript 2 is used to denote quantities associated with the bottom rotor.

The mid-chords of the top and bottom rotor blades thus pass over each other when

$$2\phi_{\text{skew}} \frac{(r-r_i)}{(r_t-r_i)} = (\Omega_1 + \Omega_2)t - \phi_{i,1} + \phi_{i,2}.$$ (63)

The Mach number at which this blade overlap point moves along the radial direction, M_o, is straightforwardly calculated as

$$M_o = \frac{1}{c_0}\frac{dr}{dt} = \frac{(\Omega_1 + \Omega_2)(r_t - r_i)}{2c_0\phi_{\text{skew}}}.$$

(64)

Clearly, the overlap point speed is infinite for a rotor system with straight blades and decreases as the skew angle increases. For the rotor system speed combinations considered in this paper, M_o is equal to 0.52 and 0.32, respectively, for the 20° and 35° skewed rotors. Thus, we expect that the impulses generated by the bound potential field interactions along the blade span will be "de-phased" at all observer locations.

In order to explore this de-phasing effect, the data from the CFD simulations was processed as follows: the reference blade of each rotor was divided into 10 segments, and the acoustic pressure time-history radiated from each segment was calculated at an observer location on the rotor axis above the rotor in the acoustic far-field (i.e., at $\theta_x = 0°$). Note that at this location, the acoustic pressure is periodic as the pressure produced by each impulse is identical regardless of the location of the rotor blades when the impulsive force is generated. Fig. 39, Fig. 40 and Fig. 41 present the acoustic pressure radiated from the top rotor reference blade for the rotor systems with straight and skewed blades. Each figure presents two subplots: the top subplot shows the total acoustic pressure plotted against non-dimensional time for a single impulse, whilst the bottom subplot is a pseudocolor plot showing the acoustic pressure radiated from each segment of the rotor blade plotted against non-dimensional time (on the horizontal axis) and the non-dimensional radial location of the segment (on the vertical axis). A red dashed line is also shown on these plots which indicates the times at which the sound generated when the mid-chords of the top and bottom reference blades overlap arrives at the observer location. Fig. 39 shows the results for the rotor system with the straight blades. It is observed that the peak pressure impulse radiated from each segment of the rotor blade occurs at approximately the same time resulting in a sharp total pressure impulse with a large amplitude and a relatively narrow period. Fig. 40 and Fig. 41 show, respectively, the results for the rotor systems with the blades with skew angles of 20° and 35°. In these plots it is observed that the peaks in the pressure radiated from each segment are offset in time – with the offset being larger for the rotor system with the blades with the 35° skew angle. This offset is partially responsible for the total pressure impulse having a relatively lower peak and occurring over a longer time period compared to the straight blade result – with the effect being more pronounced for the 35° skew angle case.

Fig. 39 The predicted total acoustic pressure time-history produced by the top blade with $\phi_{\text{skew}} = 0°$ (top). Pseudocolor plot of the predicted acoustic pressure radiated from each segment against normalised radius (vertical axis) and normalised time (horizontal axis) (bottom). The dashed red line indicates the times at which the sound generated when the mid-chords of the reference blades overlap arrives at the observer location.
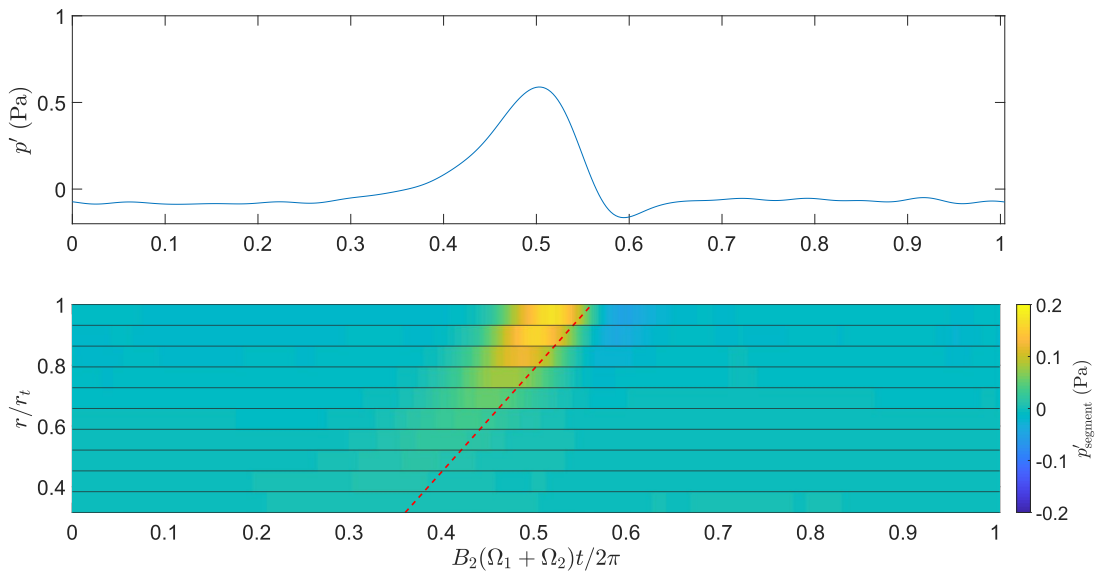
Fig. 40 The predicted total acoustic pressure time-history produced by the top blade with $\phi_{\text{skew}} = 20°$ (top). Pseudocolor plot of the predicted acoustic pressure radiated from each segment against normalised radius (vertical axis) and normalised time (horizontal axis) (bottom). The dashed red line indicates the times at which the sound generated when the mid-chords of the reference blades overlap arrives at the observer location.
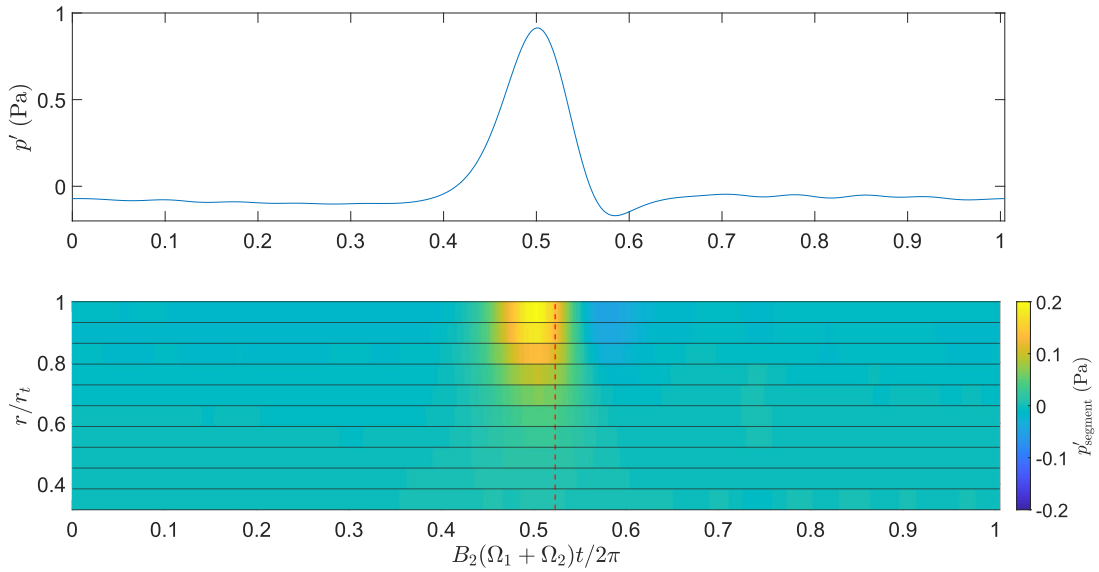
Fig. 41 The predicted total acoustic pressure time-history produced by the top blade with $\phi_{\text{skew}} = 35°$ (top). Pseudocolor plot of the predicted acoustic pressure radiated from each segment against normalised radius (vertical axis) and normalised time (horizontal axis) (bottom). The dashed red line indicates the times at which the sound generated when the mid-chords of the reference blades overlap arrives at the observer location.
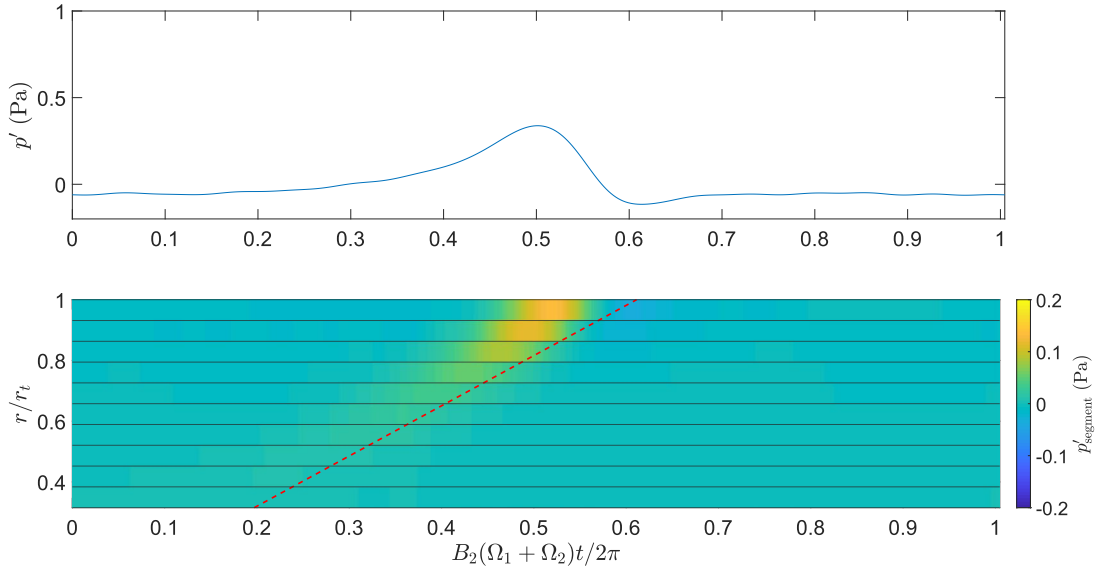
Similar results are presented in Fig. 42, Fig. 43 and Fig. 44 for the acoustic pressure at an observer located at $\theta_{\mathbf{x}} = 0°$ radiated from the reference blade of the bottom rotor. As before, red dashed lines are used to show the times at which the sound generated when the mid-chords of the top and bottom blades overlap arrives at the observer location. In addition, black ellipses indicate the times at which the sound generated when the vortex region impinges on the bottom rotor blade arrives at the observer location. Once again it is observed that the total acoustic pressure impulse radiated from the blade with a skew angle of 20° is reduced in amplitude and is broader than that produced by the straight blade. However, for this case, the tip vortex interaction complicates the situation. The pseudocolor plots show that the acoustic pressure produced by the outer portion of the blades is quite different in character to that produced by the inner portion of the blades where the bound potential field interactions are expected to dominate. The pressure produced by the outer portion of the blades contains a strong negative pressure impulse which appears to be generated at times when the tip vortex region begins to interact with the bottom rotor blade. The acoustic pressure produced by the bound potential field interactions at the inner radii has relatively low amplitude for all cases, presumably due to the low blade loading at these radii. The total pressure produced by the blade with a skew angle of 35° contains no clear impulse.

Fig. 42 The predicted total acoustic pressure time-history produced by the bottom blade with $\phi_{\text{skew}} = 0°$ is shown on the top. Pseudocolor plot of the predicted acoustic pressure radiated from each segment against normalised radius (vertical axis) and normalised time (horizontal axis) is shown on the bottom. The dashed red line indicates the times at which the sound generated when the mid-chords of the reference blades overlap arrives at the observer location. The black ellipse indicate the times at which the sound generated when the vortex region impinges on the bottom rotor blade arrives at the observer location.
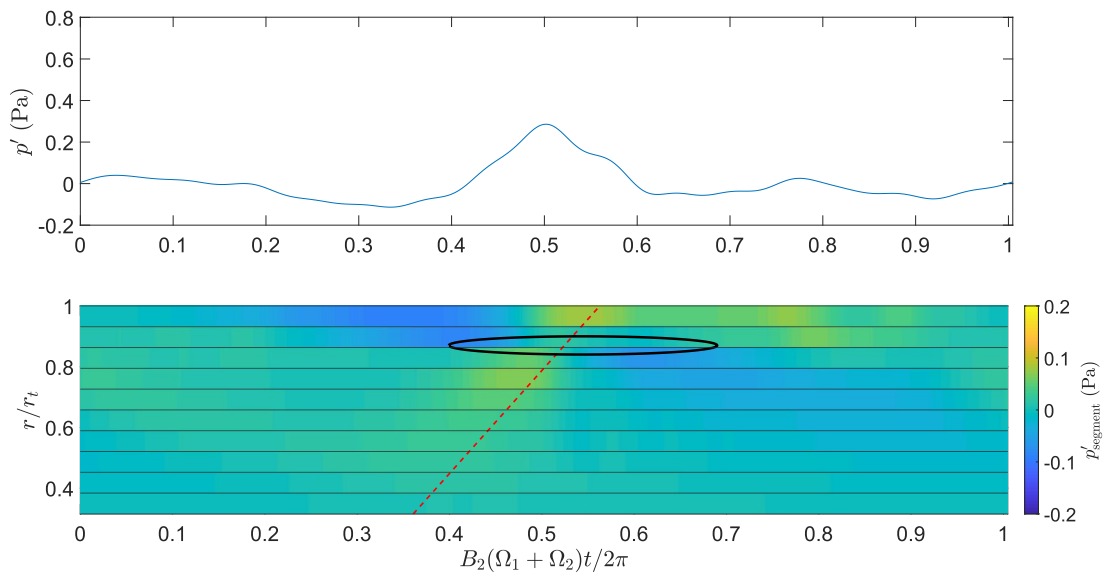
Fig. 43 The predicted total acoustic pressure time-history produced by the bottom blade with $\phi_{\text{skew}} = 20°$ is shown on the top. Pseudocolor plot of the predicted acoustic pressure radiated from each segment against normalised radius (vertical axis) and normalised time (horizontal axis) is shown on the bottom. The dashed red line indicates the times at which the sound generated when the mid-chords of the reference blades overlap arrives at the observer location. The black ellipse indicate the times at which the sound generated when the vortex region impinges on the bottom rotor blade arrives at the observer location.
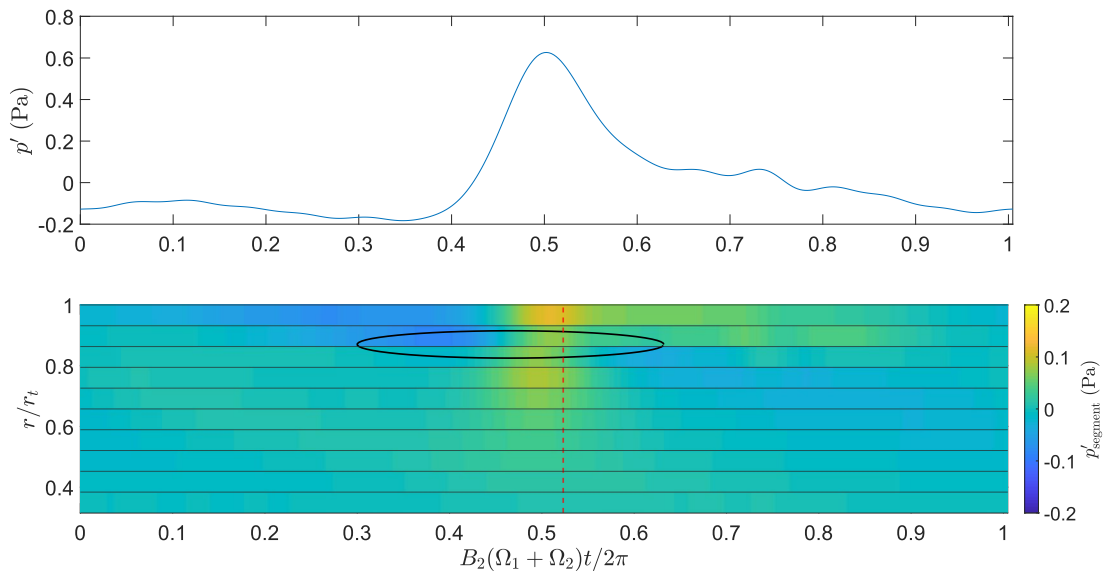
69
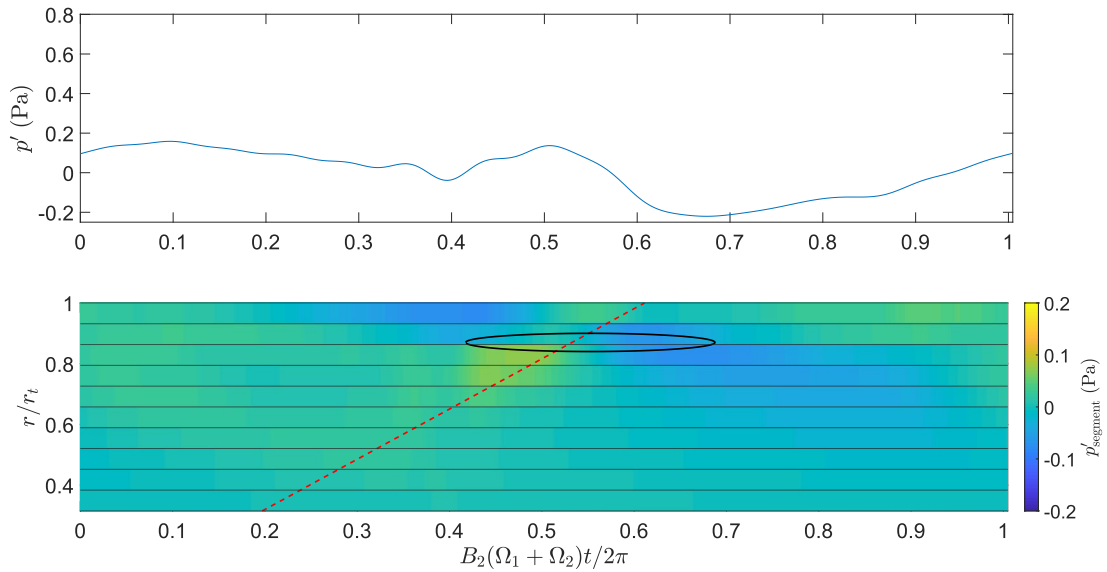
Fig. 44 The predicted total acoustic pressure time-history produced by the bottom blade with $\phi_{\text{skew}} = 35°$ is shown on the top. Pseudocolor plot of the predicted acoustic pressure radiated from each segment against normalised radius (vertical axis) and normalised time (horizontal axis) is shown on the bottom. The dashed red line indicates the times at which the sound generated when the mid-chords of the reference blades overlap arrives at the observer location. The black ellipse indicate the times at which the sound generated when the vortex region impinges on the bottom rotor blade arrives at the observer location.

The plot on the left shown in Fig. 45, compares the predicted total pressure impulses radiated from the top rotor reference blades for the three different rotor systems. This plot clearly shows how increasing the blade skew angle reduces the amplitude of the pressure impulse and increases the period over which the impulse occurs. The reduction in the peak total pressure amplitude, and the widening of the period over which the impulsive noise occurs, results in a reduction in the level of the tones – particularly at higher frequencies. To demonstrate this effect, the tonal sound pressure levels radiated from the top rotor reference blade are shown in the plot on the left shown in Fig. 46. This clearly shows that the levels of the tones produced by the rotor systems decreases as the blade skew angle increases and that the reduction in level becomes larger as the frequency of the tone increases. Corresponding plots for the pressure impulses radiated from the bottom rotor reference blade are shown in the plot on the right in both Fig. 45 and Fig. 46. As discussed above, although these impulses/tones are affected by the tip vortex interactions, (except for the first tone) there is generally a reduction in the amplitude of the impulses/tones as the blade skew angle increases.
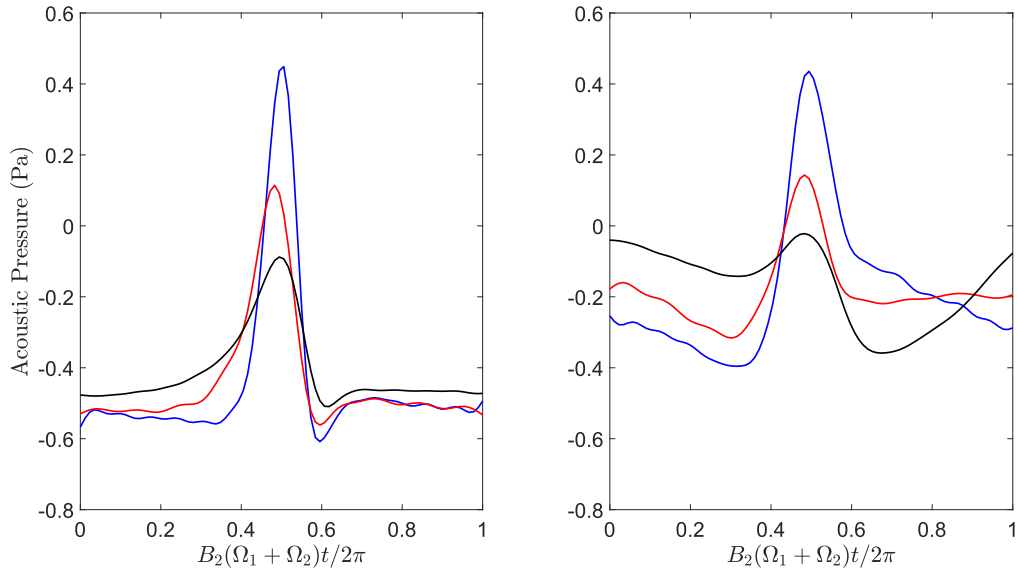
Fig. 45 Comparison of predicted total acoustic pressure at $\theta_x = 0°$ produced by the reference blade of the top (a) and bottom (b) rotors plotted against non-dimensional time. $\phi_{skew} = 0°$ (blue) , $20°$ (red) and $35°$ (black).
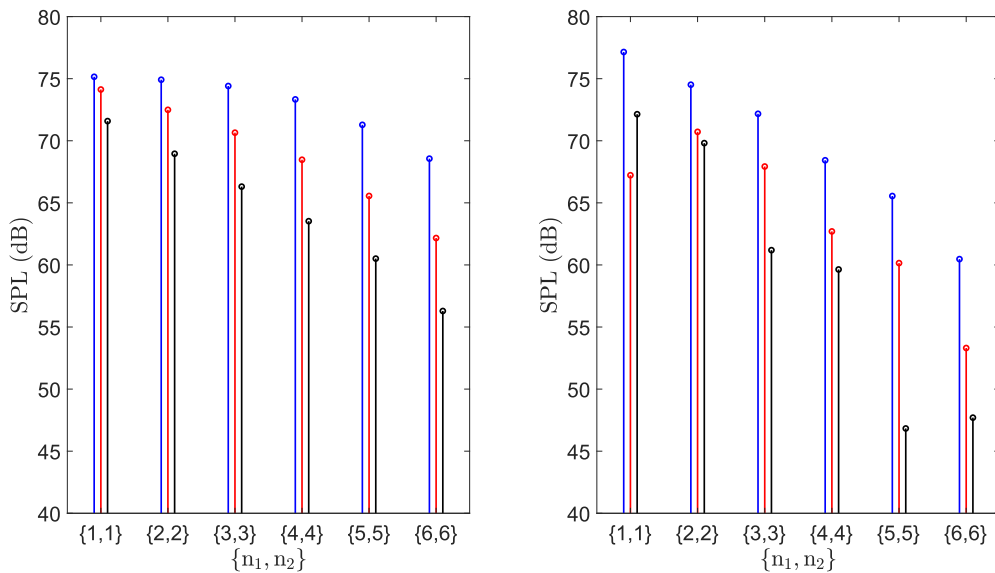
Fig. 46 Comparison of sound pressure level of the first six interaction tones at $\theta_x = 0°$ produced by the reference blade of the top (a) and bottom (b) rotors. $\phi_{skew} = 0°$ (blue) , $20°$ (red) and $35°$ (black).

Fig. 39, Fig. 40 and Fig. 41 show that the amplitude of the acoustic pressure impulse radiated from the top rotor reference blade decreases as the skew angle increases. This is in part due to the de-phasing effect but could also be caused changes in the response of the skewed blades to the bound potential field disturbance compared to the straight blades and/or the slight differences in blade loading between the different cases (which will affect the strength of the bound potential field).

71

In order to investigate the significance of the de-phasing effect, two calculations were performed in which a time-lag was applied to the pressure radiated from each of the 10 radial segments from the reference blade of the top rotor with straight blades (i.e. the results shown on the bottom plot in Fig. 39). For each calculation, this time-lag corresponded to that expected for one of the skewed blades and amounted shifting the pressure impulse radiated from a segment with mid-span location at radius r by a time τ, where

$$\tau = \frac{2\phi_{\text{skew}}(r - r_i)}{(\Omega_1 + \Omega_2)r_t}.$$
(65)

The results of the calculation for a blade with a skew angle of 20° are shown on left plot in Fig. 47. This is compared with the acoustic pressure impulse predicted directly from the CFD simulation of the rotor system with blades with a skew angle of 20°. Corresponding results for the 35° skew case are shown on the right plot in Fig. 47. Both plots show excellent agreement between the direct prediction and the prediction made by 'de-phasing' the pressure radiated from each segment of the straight-blades. These results demonstrate that the de-phasing effect is the primary cause of the reduction in the amplitude of the impulse radiated from the top rotor blades.
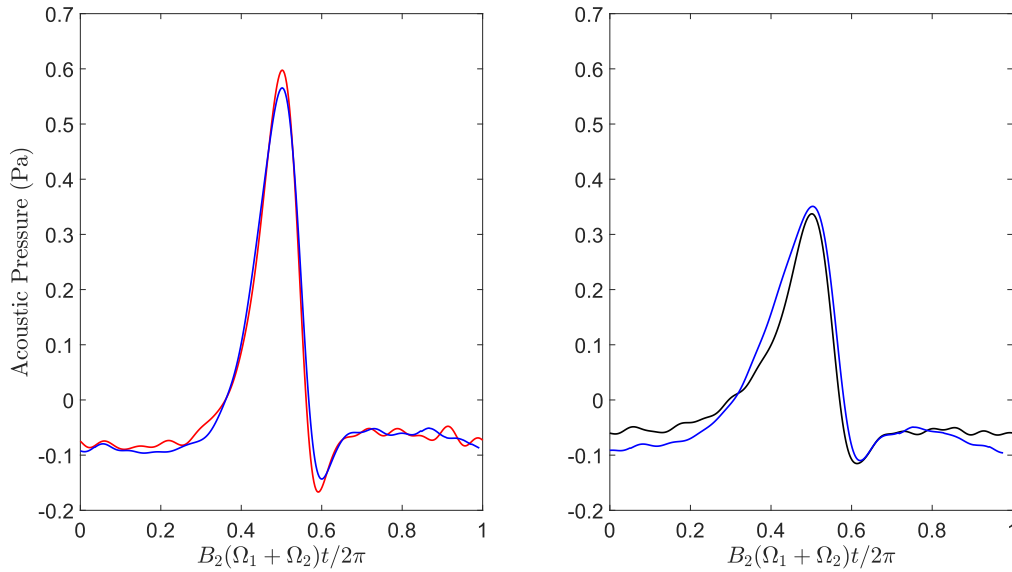
Fig. 47 Acoustic pressure versus non-dimensional time. The blue curves show the acoustic pressure predicted by de-phasing the sound radiated from the straight blades, whilst the red and black curves show the acoustic pressure predicted for the skewed blades. These plots were generated using loading data taken from the CFD simulations. Subplots on the left and right respectively show the results for the rotor systems with $\phi_{\text{skew}} = 20°$ and $35°$.

A similar calculation was performed using the semi-analytical model and the results are presented in Fig. 48. Recall that the semi-analytical model uses the steady loading from the CFD simulation, and thus the small differences in the strength of the bound potential field produced by the blades on the different rotor systems are accounted for. However, the semi-analytical model does not include the effect of blade skew on the unsteady loading response of the blades. Nevertheless, the results calculated by de-phasing the sound radiated from the straight blade are in good agreement with those

calculated for the skewed blades, supporting the hypothesis that the de-phasing effect is the predominant cause of the reduction in the interaction noise radiated from the top rotor blades.
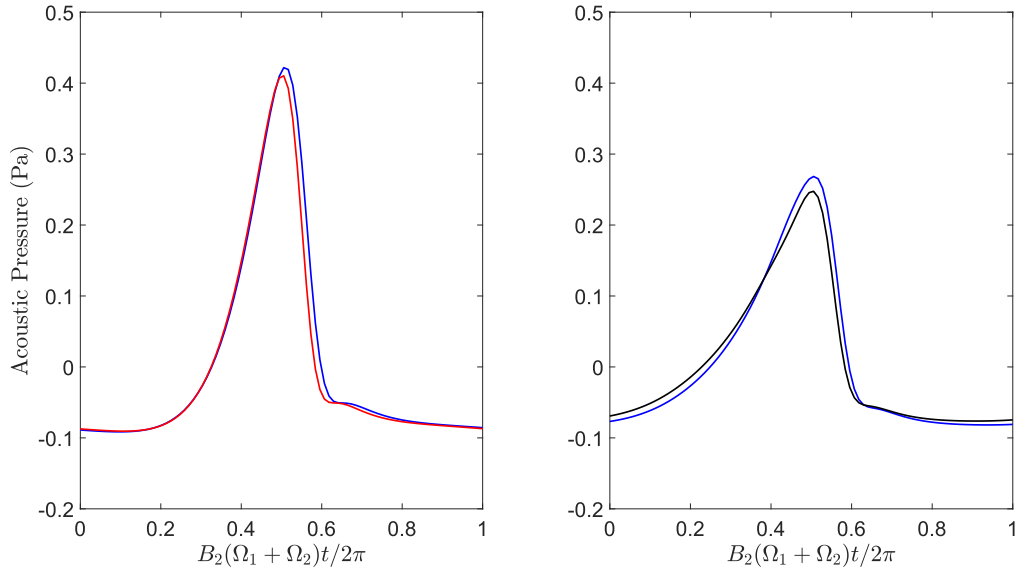
Fig. 48 Acoustic pressure versus non-dimensional time. The blue curves show the acoustic pressure predicted by de-phasing the sound radiated from the straight blades, whilst the red and black curves show the acoustic pressure predicted for the skewed blades. These plots were generated using the semi-analytical model. Subplots on the left and right respectively show the results for the rotor systems with $\phi_{skew} = 20°$ and $35°$.

3.7 Chapter summary

This chapter has investigated the effect of blade skew angle on the interaction tones produced by a contra-rotating UAV rotor system. Three different rotor systems were investigated: one with straight blades and two with skewed blades – with skew angles of 20° or 35°.

CFD simulations were used to predict the unsteady loading on the blades of each rotor system operating at two different speed settings. This loading data was then used in either a time- or frequency-domain acoustic analogy method to predict the radiated acoustic pressure time history or sound pressure levels of the interaction tones. A semi-analytical model was also used to assess the importance of the bound potential field interaction noise source. The numerical methods and the semi-analytical models used in this paper are presented in Jung et al.[72].

Two of the rotor systems were manufactured and were tested in an anechoic chamber at the two different operating conditions. During these tests, the total thrust and radiated acoustic pressure was measured. The measured thrust was in good agreement with the thrust predicted from the CFD simulations and the predicted sound pressure levels of the prominent interaction tones were also observed to be in generally good agreement with the measured levels. It was observed that increasing the blade skew angle generally reduced the level of the prominent interaction tones at many observer locations. The overall A-weighted sound power level of the interaction tones radiated from each rotor system was also calculated from the numerical simulations for one operating condition and it was found that there was an 8.7 dB reduction in the A-weighted sound power level produced by the rotor system with the highly skewed blades compared with that produced by the rotor system with straight blades.

The causes of the noise reduction were investigated, and it was shown to be primarily due to the de-phasing of the acoustic pressure impulses radiated from different radii along the blade span.

4. Effect of blade crop, skew and pitch angle on the noise produced by a contra-rotating UAV rotor system

This chapter presents an investigation into the effect of several different geometry modifications to the bottom rotor blades of a contra-rotating UAV rotor system on the level of the radiated interaction tones. These geometry modifications include cropping and changing the pitch of the bottom rotor blades, and these are described in detail in section 4.1. CFD simulations of each rotor system were performed using the general methods described in Chapters 2 and 3 and these are briefly described in section 4.2. The loading data from these simulations was then used to predict the radiated acoustic pressure using the time- and frequency-domain methods described in Chapter 2. Experiments were also undertaken to measure the noise and total thrust produced by these rotor systems. These were undertaken in the anechoic chamber at the University of Auckland using a similar set-up and method to the experiments described in Chapters 2 and 3. The results from these experiments and predictions are presented and compared in section 4.3. The results are analysed and discussed in section 4.4 and the chapter concludes with an overall summary in section 4.5.

4.1 Contra-rotating rotor system geometries

4.1.1 Rotor systems with cropped bottom rotors

The geometries of the rotor systems with cropped bottom rotors are identical to the three different rotor systems with straight and skewed blades (with skew angles of 20° and 35°) considered in Chapter 3, but with the downstream rotor cropped so that its tip radius was 80% of that of the top rotor and the bottom rotor pitch changed in order to match the thrust produced by the corresponding uncropped rotor system. This amount of cropping was based on the results presented in section 3.6 of Chapter 3 (see Figs. 42-44) where it was observed that unsteady loading on the outer 20% of the bottom rotor blades due to their interaction with the tip vortices from the top rotor produced significant levels of radiated noise.

For all the experiments and simulations of the rotor systems with cropped downstream blades presented in this chapter, the top rotor rotated at 535 rad/s whilst the bottom rotor rotated in the opposite direction at 465 rad/s.

In order to conduct a fair assessment of the effect of cropping on the noise produced by the rotor system, the total thrust should be held constant. This was achieved by adjusting the pitch of the bottom rotor blades to produce a total thrust which was very similar to that produced by the equivalent uncropped rotor system. The appropriate blade pitch angle was determined from unsteady CFD simulations which determined that the rotor systems with the straight blades and with the skewed blades with $\phi_{\text{skew}} = 20°$ required the bottom rotor blades to be pitched at 10°, whilst the rotor system with the skewed blades with $\phi_{\text{skew}} = 35°$ required the bottom rotor blades to be pitched at 8°.

A CAD rendering of the three different rotor systems with cropped bottom rotors is shown in Fig. 49.
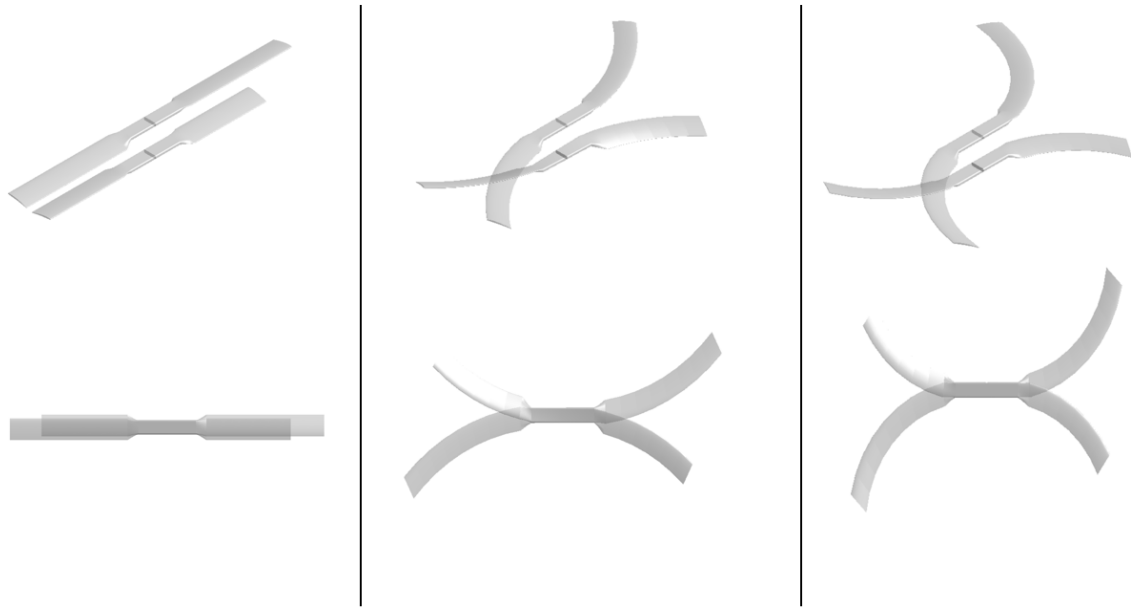
Fig. 49 CAD rendering of the three different rotor systems with cropped bottom rotors considered in this chapter.

4.1.2 Rotor systems with adjustable blade pitch

For the study investigating the effect of bottom rotor blade pitch, both rotors utilised the blades of a 15" diameter T-motor 15×5 propeller mounted in the custom-made hub shown in Fig. 50. This allowed the pitch angle of the bottom rotor to be tested at pitch angles $\beta = 0°$, 4°, 8° and 12°. A schematic diagram of the blade pitch angle that was varied is shown in Fig. 51. The spacing between the rotors was kept constant at 40 mm for all tests.

In this investigation, the rotational speed of the top rotor was kept constant while the rotational speed of the bottom rotor was varied. The overall total thrust produced by the contra-rotating UAV system was kept constant.

Fig. 50 Exploded view of variable pitch aluminium hub
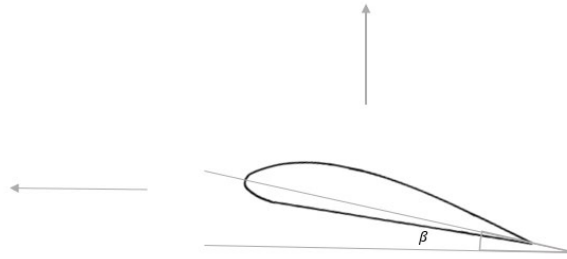
Fig. 51 A schematic drawing of the blade pitch angle that was varied by the lower blade.

4.2 Numerical prediction methods

URANS CFD simulations for each of the cases considered in this chapter were conducted using Ansys Fluent using the methods described in Chapters 2 and 3. For all simulations, the unsteady CFD simulations were initialised using the results obtained from steady RANS simulations which utilised Fluent's multiple reference frame model. The time-step size for the transient simulations was set so that top rotor rotated 1° per time step and the transient simulations were computed until the thrust force produced by the top and bottom rotors was observed to be periodic. This loading data was input into either the time- or frequency domain noise prediction methods described in Chapter 2.

4.3 Predictions versus measurements

4.3.1 Rotor systems with cropped bottom rotors

The measured and predicted thrust is summarised in table 1 below and show good agreement.

Table 1. Measured and predicted total thrust.

	Measured total thrust (N)	Predicted total thrust (N)
Rotor system with straight blades	18.25	18.82
Rotor system with skewed blades ($\phi_{\text{skew}} = 20°$)	-	19.49
Rotor system with skewed blades ($\phi_{\text{skew}} = 35°$)	16.32	17.53

Note that as for the results presented in Chapters 2 and 3, all sound pressure levels are normalised to a distance of 1.5 m from the centre of the bottom rotor assuming spherical spreading.

Fig. 52 and Fig. 53 respectively plot the measured and predicted sound pressure level polar directivity patterns for three different interaction tones produced by the contra-rotating UAV systems with cropped downstream rotors with straight blades ($\phi_{\text{skew}} = 0°$) and skewed blades ($\phi_{\text{skew}} = 35°$). The agreement between the predictions and the measurement is very good for the interaction tones that are presented. As expected for these interaction tones, the acoustic pressure radiates strongly along the rotor axis (at $\theta_x = 0°$ and 180°) and the amplitude of the acoustic pressure decreases as the observer moves toward the plane of the rotor at $\theta_x = 90°$.

Fig. 52 Sound pressure level polar directivity plot for three different interaction tones produced by the rotor system with a cropped downstream rotor and straight blades. Numerical predictions (red) and experimental measurements (blue with circle markers) are presented for the $\{n_1 = 1, n_2 = 1\}$ tone (top left), the $\{n_1 = 2, n_2 = 2\}$ tone (top right) and the $\{n_1 = 3, n_2 = 3\}$ tone (bottom).
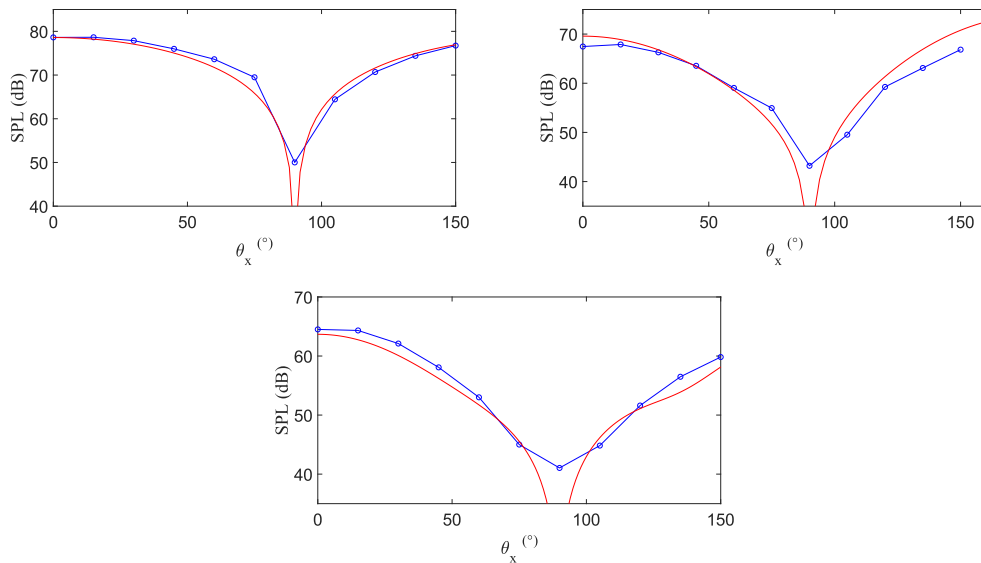
Fig. 53 Sound pressure level polar directivity plot for three different interaction tones produced by the rotor system with a cropped downstream rotor and skewed blades ($\phi_{\text{skew}} = 35°$). Numerical predictions (red) and experimental measurements (blue with circle markers) are presented for the $\{n_1 = 1, n_2 = 1\}$ tone (top left), the $\{n_1 = 2, n_2 = 2\}$ tone (top right) and the $\{n_1 = 3, n_2 = 3\}$ tone (bottom).

Fig. 54 plots the predicted polar sound pressure level directivities of three different interaction tones for the three different rotor systems with the cropped downstream rotors. These results show a similar trend to the results presented in Chapter 3 (Fig. 37) for the rotor systems with the uncropped rotors where as the skew angle increases, the sound pressure level generally decreases. Fig. 55 plots the sound pressure levels of prominent interaction tones at observer locations of $\theta_x = 0°$ and 45°. These

results are similar to those presented in Chapter 3 (Fig. 46) for the rotor systems with the uncropped rotors. Once again, it is observed that the sound pressure level decreases as the blade skew angle increases and that the decrease is more prominent at higher frequencies.
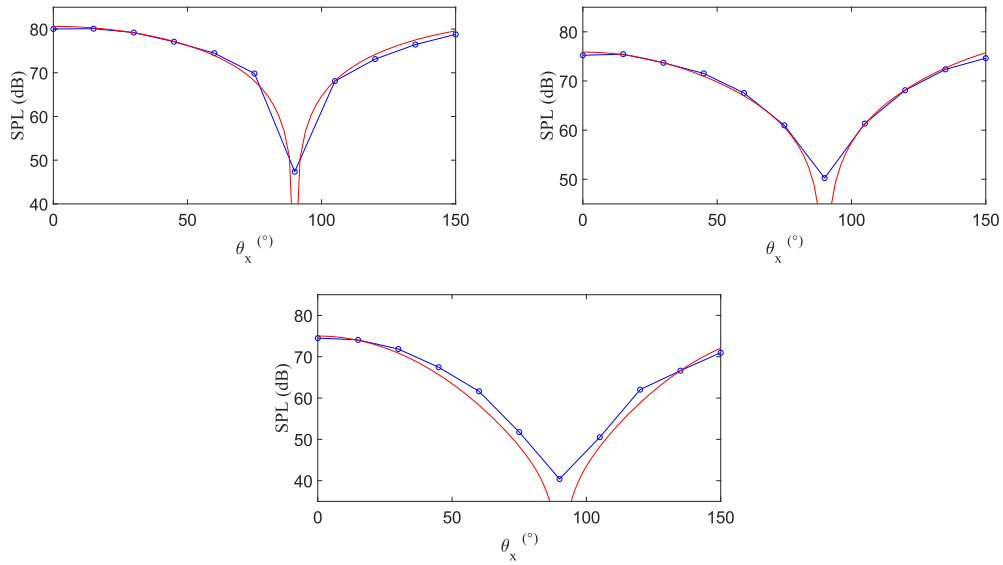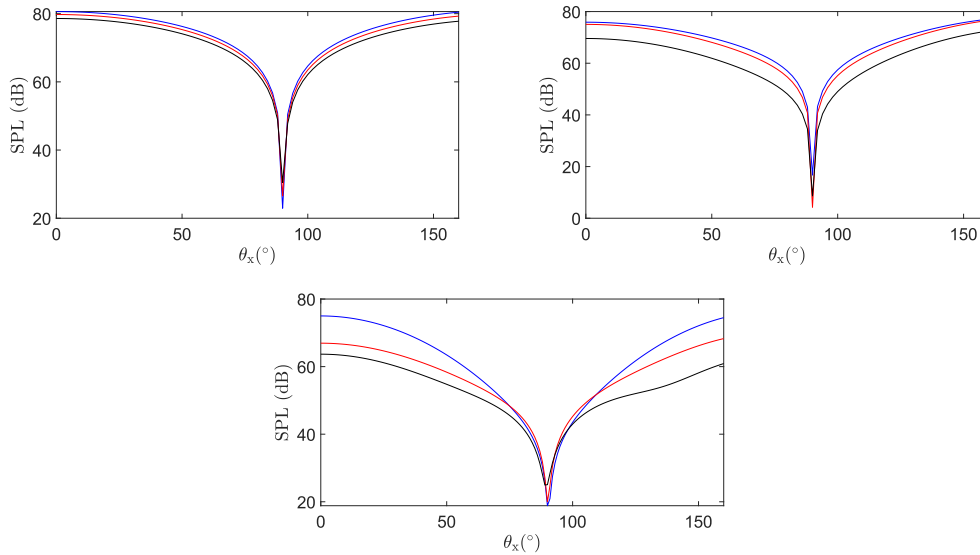

Fig. 54 Predicted sound pressure level polar directivity plots for three different interaction tones produced by the three different rotor systems with cropped lower rotors. The rotor system with straight blades ($\phi_{skew} = 0°$) (blue), $\phi_{skew} = 20°$ (red) and $\phi_{skew} = 35°$ (black). Predictions are presented for the $\{n_1 = 1, n_2 = 1\}$ (top left) tone, the $\{n_1 = 2, n_2 = 2\}$ tone (top right) and the $\{n_1 = 3, n_2 = 3\}$ tone (bottom).
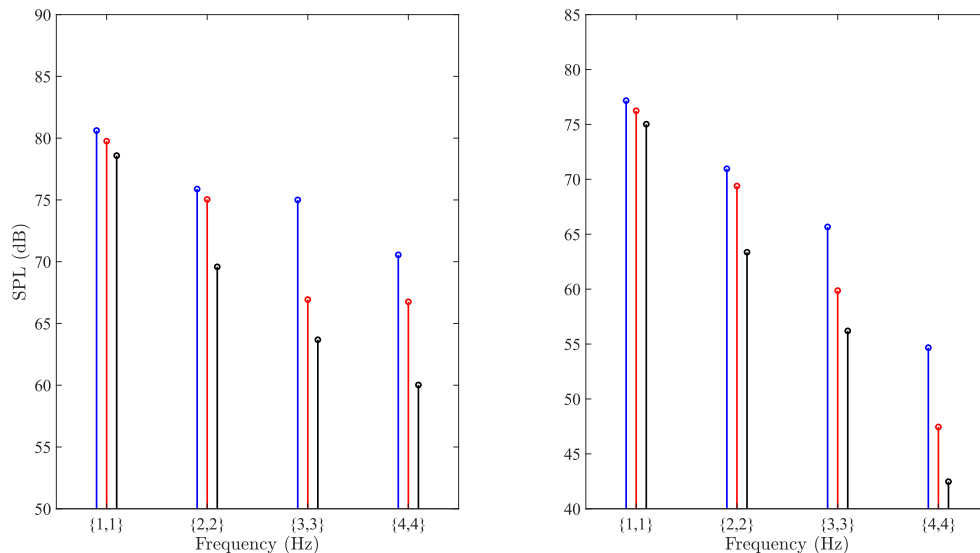

Fig. 55 Comparison of the sound pressure levels for four different interaction tones produced by rotor systems with cropped lower rotors at observer locations $\theta_x = 0°$ (left) and $\theta_x = 45°$ (right). The rotor system with straight blades ($\phi_{skew} = 0°$) (blue), $\phi_{skew} = 20°$ (red) and $\phi_{skew} = 35°$ (black).

The overall A-weighted sound power level was also calculated for the three rotor systems with cropped downstream rotors using the method described in Chapter 3. The overall A-weighted sound power level calculated for the rotor system with the straight blades was 89.9 dB, whereas the level for

79

the rotor systems with the skewed blades was 88.10 dB and 84.65 dB respectively for the rotors with skew angles of 20° and 35°. As for the uncropped rotors, there is a significant reduction in sound power level as the blade skew angle increases.

4.3.2 Rotor systems with adjustable blade pitch

Fig. 56 plots the measured and predicted sound pressure level polar directivities of six different interaction tones produced by the configuration where the bottom rotor was pitched at $\beta = 8°$. Note that the acoustic measurements were taken at four different locations ($\theta_x = 0°$, 45°, 90° and 135°). The agreement between the predictions and the measurement is very good which suggests that the unsteady loading predicted using the CFD simulations is well-predicted. As expected for these interaction tones – which all have zero azimuthal mode order – the sound pressure level is highest close to the rotor axis ($\theta_x = 0°$ and 180°) and generally decays to a minimum close to the rotor plane ($\theta_x = 90°$).

Note that for this particular case, the measured total time-average thrust was 18.7 N which compares well with the predicted value of 19.0 N.
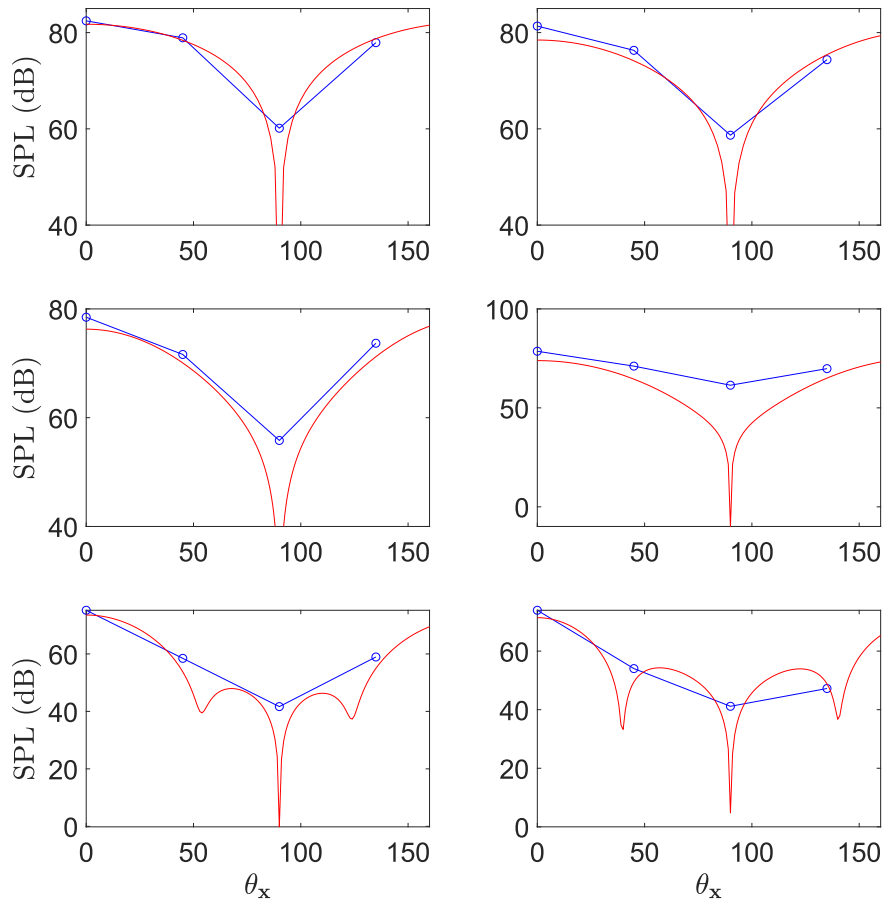
Fig. 56 Sound pressure level polar directivity for six different interaction tones produced with the rotor system with the bottom rotor blades pitched at $\beta = 8°$. Experimental measurements (blue curves with circle markers); numerical predictions (red curves). $\{n_1 = 1, n_2 = 1\}$ tone (top left), $\{n_1 = 2, n_2 = 2\}$ tone (top right), $\{n_1 = 3, n_2 = 3\}$ tone (middle left), $\{n_1 = 4, n_2 = 4\}$ tone (middle right), $\{n_1 = 5 \ n_2 = 5\}$ tone (bottom left) and $\{n_1 = 6 \ n_2 = 6\}$ tone (bottom right).

4.4 Discussion

4.4.1. Rotor systems with cropped bottom rotors

The CFD simulations were used to estimate the trajectory of the tip vortices produced by the top rotor using the following method. Firstly, isosurfaces of constant λ_2 criterion was generated. These isosurfaces include a tubular structure enclosing the centre of the tip vortex. Then, at a number of azimuthal angles, the centre of the tubular structure associated with each tip vortex was estimated. This was assumed to be the location of the centre of the tip vortex at that particular angle. This process was undertaken for the simulations of the rotor system with straight blades for the cases where the bottom rotor was cropped and uncropped and the predicted tip vortex trajectories are shown in Fig. 57. For both cases, the centre of the tip vortex passed through the location of the pitch-change axis of the bottom rotor at a radius equal to 80% of the tip radius of the top rotor. This cropping length was chosen based on the analysis in chapter 2 and 3, which demonstrated that the tip vortex predominantly interacted with the outer 20% portion of the bottom blade.

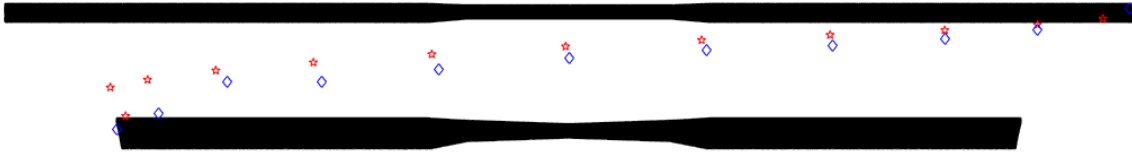**Fig. 57 Illustration showing the estimated tip vortex trajectory extracted from Isosurfaces of constant λ_2 criterion for the rotor systems with straight blades. Results for the rotor system with the uncropped bottom rotor are shown as blue diamonds whilst the results for the rotor system with the cropped lower rotor are shown as red stars.**

Fig. 58, Fig. 59 and Fig. 60 present the predicted acoustic pressure radiated from the top rotor reference blade at and observer location of $\theta_x = 0°$ and $R_x = 1.5$ m for the rotor systems with a cropped lower rotor. Fig. 58 presents the results calculated for the case where the rotor blades were straight, whilst Fig. 59 and Fig. 60 presents the results calculated for the cases where the rotor blades were skewed with skew angles of 20° and 35°. The top subplot in each figure shows the total pressure radiated from blade whereas the bottom subplot is a contour plot which shows contours of pressure radiated from each of ten equally sized radial segments of the blade versus non-dimensional radius (y-axis) and non-dimensional time (x-axis). The contour plots clearly show the impulsive noise produced as the rotor blade passes over the bottom rotor and that, for the straight blade, this impulse is generated at the same time (and therefore arrives at this observer location at the same time). However, for the rotor systems with the skewed blades, the impulses are generated at different times and therefore the impulse radiated from each radial segment arrives at the observer location at different times. This results in a total impulse produced by the skewed blades with lower amplitude. Additionally, for all cases it is observed that cropping the bottom rotor results in very little noise being generated by the tip region of the top rotor blades due to the fact that there is little interaction of these blades with the bound potential field of the bottom rotor at these radii.
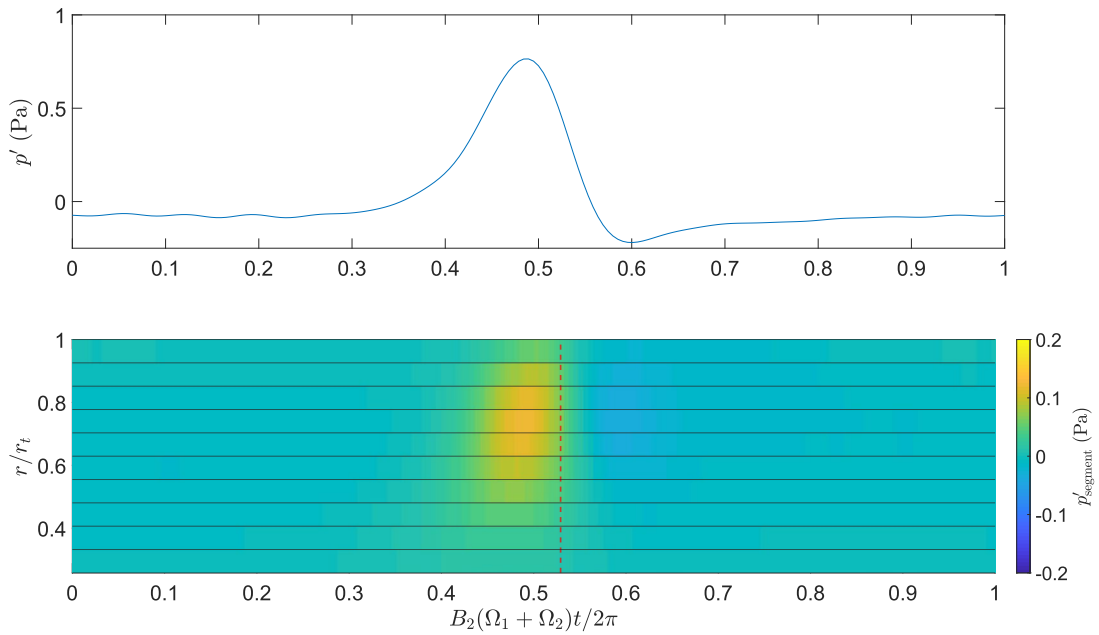
Fig. 58 Predicted total acoustic pressure produced by the top rotor reference blade of the rotor with straight blades (top). Contour plot of predicted acoustic pressure radiated from each of ten equally sized radial strips with the vertical axis plotting radius normalized by the tip radius and the horizontal axis plotting time normalized by the period of the unsteady loading (bottom).

Fig. 59 Predicted total acoustic pressure produced by the top rotor reference blade of the rotor with skewed blades ($\phi_{skew} = 20°$) (top). Contour plot of predicted acoustic pressure radiated from each of ten equally sized radial strips with the vertical axis plotting radius normalized by the tip radius and the horizontal axis plotting time normalized by the period of the unsteady loading (bottom).
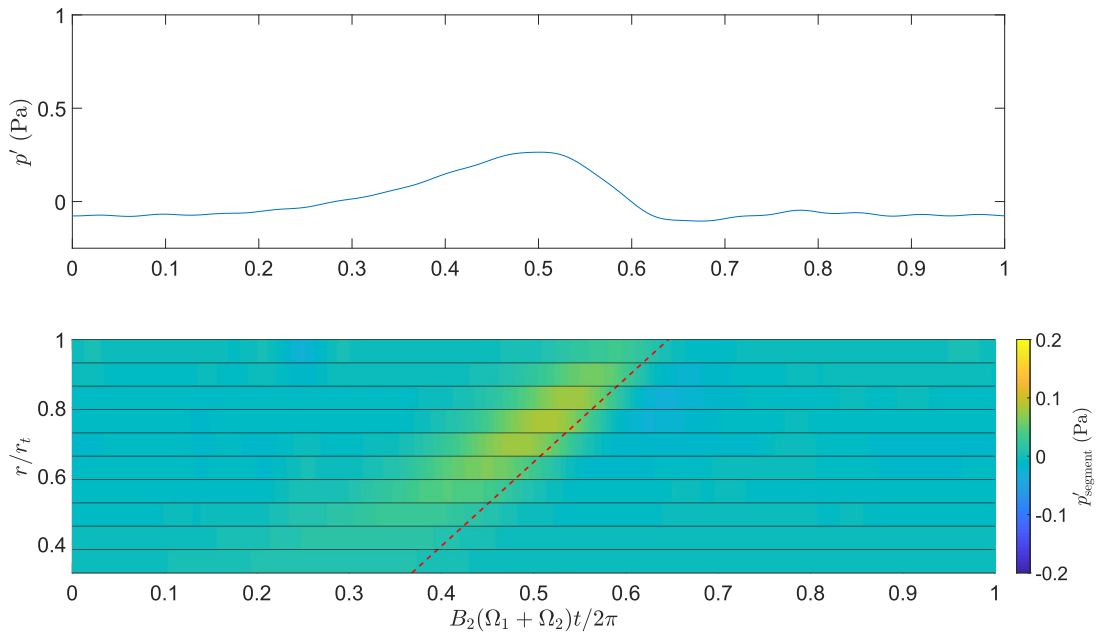
Fig. 60 Predicted total acoustic pressure produced by the top rotor reference blade of the rotor with skewed blades ($\phi_{\text{skew}} = 35°$) (top). Contour plot of predicted acoustic pressure radiated from each of ten equally sized radial strips with the vertical axis plotting radius normalized by the tip radius and the horizontal axis plotting time normalized by the period of the unsteady loading (bottom).

Fig. 61, Fig. 62 and Fig. 63 presents similar plots for the bottom rotor reference blades. The red dashed curves indicate the times at which an impulse generated when the top and bottom rotors mid-chords are aligned would arrive at the observer location. These plots show that there is a strong impulse generated close to the times where the top and bottom rotor blades are aligned. However, the magnitude of this impulse decreases significantly as the blade skew angle increases. Unlike for the uncropped rotor blades (shown in Figs. 42-44), there is no clear effect of the tip vortex impingement.
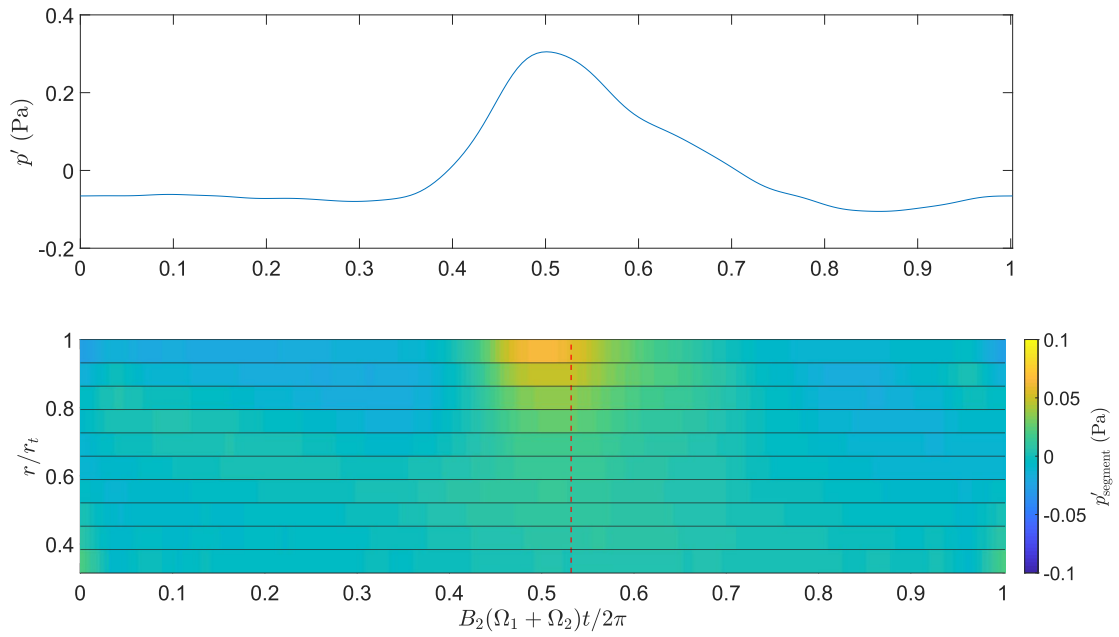
Fig. 61 Predicted total acoustic pressure produced by the cropped bottom blade with $\phi_{\text{skew}} = 0°$ (top). Contour plot of predicted acoustic pressure magnitude with vertical axis plotting radius normalized by the tip radius and horizontal axis plotting time normalized by the period (bottom).
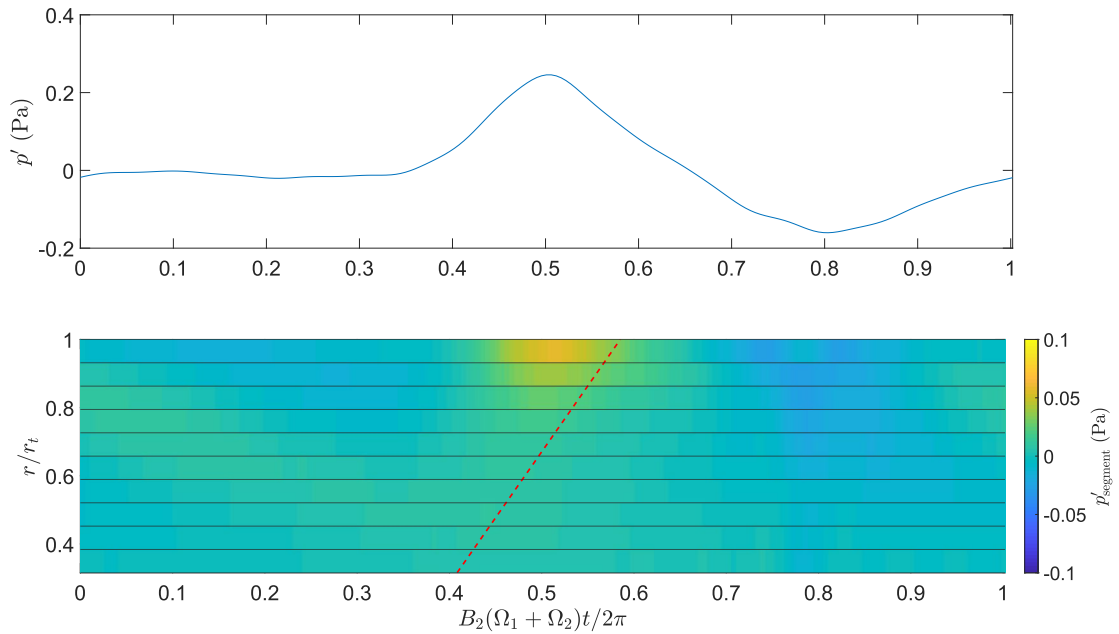
Fig. 62 Predicted total acoustic pressure produced by the cropped bottom blade with $\phi_{\text{skew}} = 20°$ (top). Contour plot of predicted acoustic pressure magnitude with vertical axis plotting radius normalized by the tip radius and horizontal axis plotting time normalized by the period (bottom).
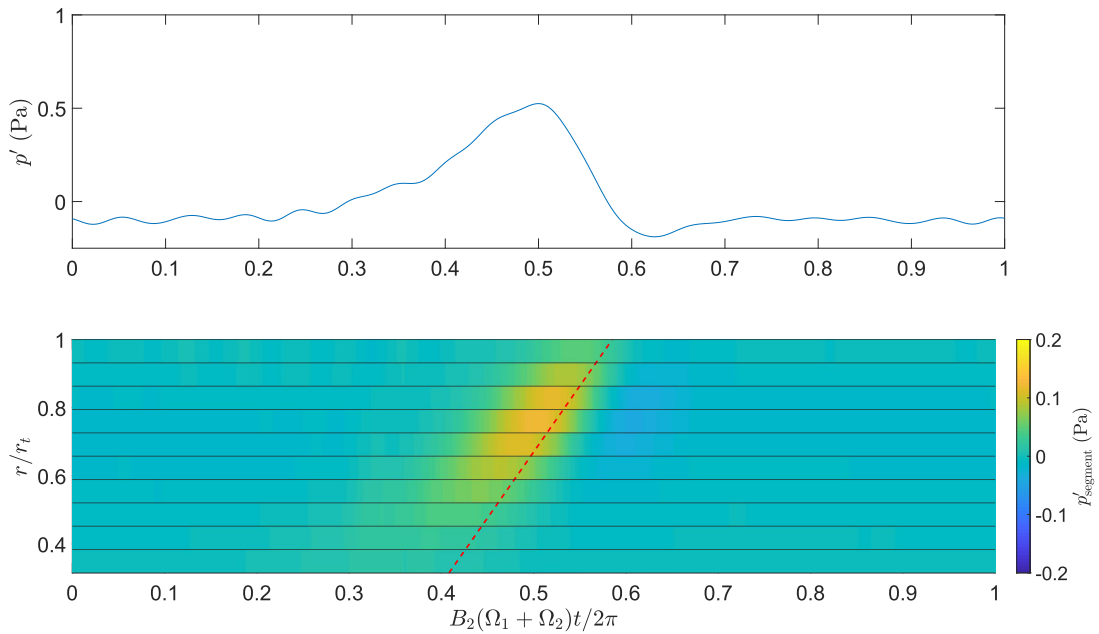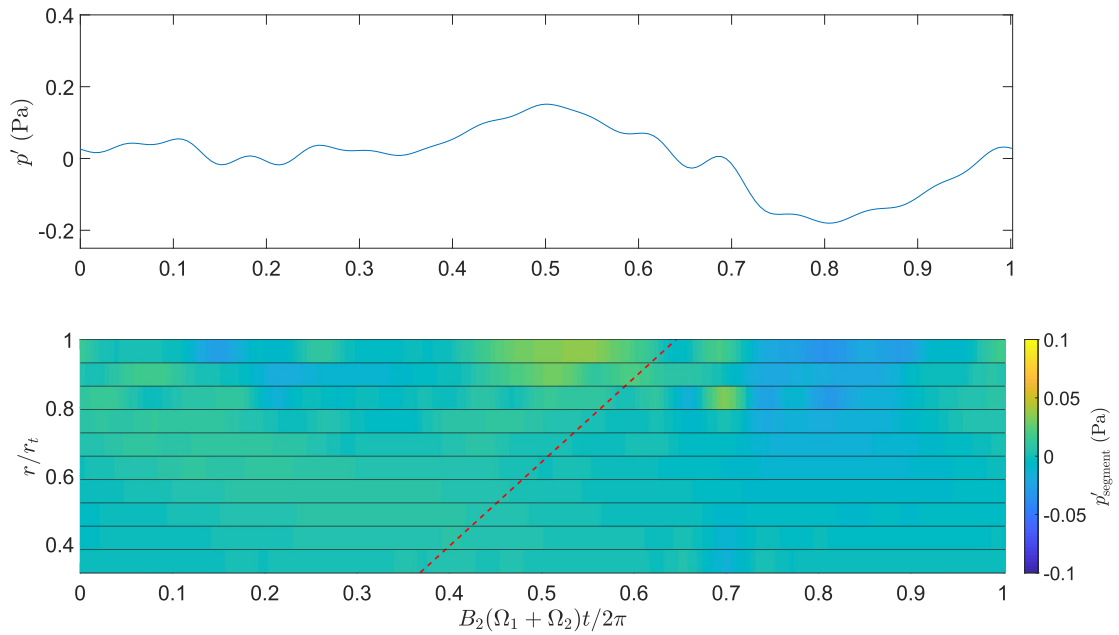
Fig. 63 Predicted total acoustic pressure produced by the cropped bottom blade with $\phi_{\text{skew}} = 35°$ (top). Contour plot of predicted acoustic pressure magnitude with vertical axis plotting radius normalized by the tip radius and horizontal axis plotting time normalized by the period (bottom).

4.4.2 Rotor systems with adjustable blade pitch

Fig. 64 plots a comparison of the measured sound pressure level of the first four interaction tones produced by the rotor systems with the bottom rotor pitched at $\beta = 0°$, $4°$, $8°$ and $12°$. These measurements were all made on the rotor axis at $\theta_x = 0°$ at $R_x = 1.5$ m. The sound pressure levels of the first interaction tone are similar for all four cases. There is some variation with the levels of the higher frequency tones, but no clear trend.
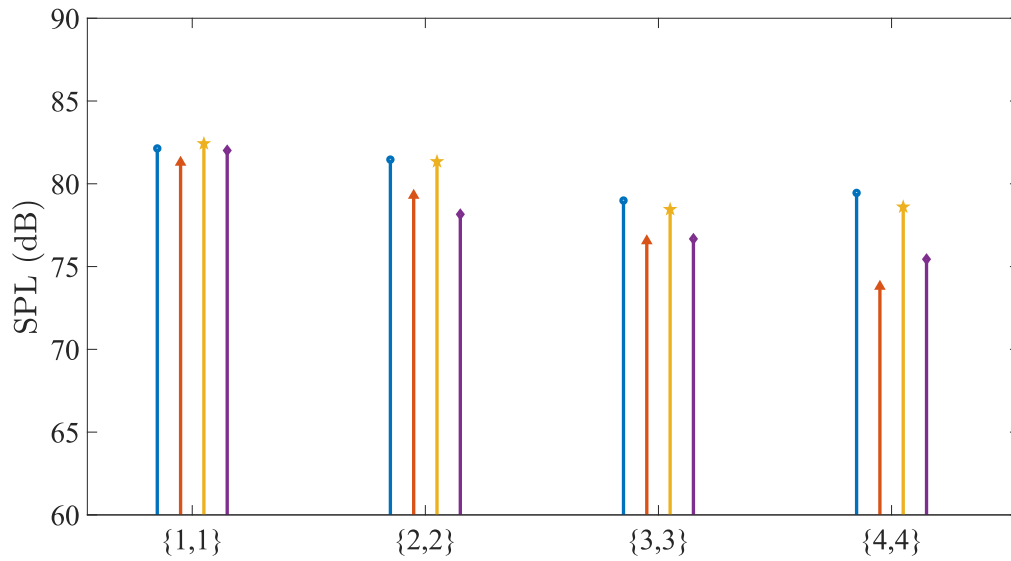
Fig. 64 Comparison of the measured sound pressure level of prominent interaction tones produced by a contra-rotating UAV rotor system with the bottom rotor pitched at $\beta = 0°$ (blue), 4° (red), 8° (yellow) and 12° (purple).

Fig. 65 plots the predicted levels for the cases presented in Fig. 65. Similarly, there is some small variation in the level of each tone for the different pitch angle cases, but no clear trend.
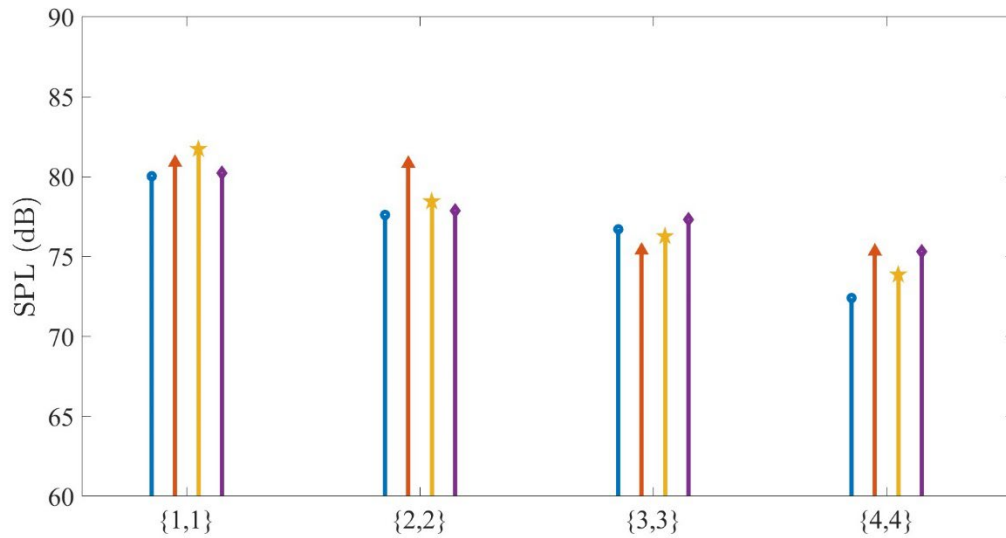
Fig. 65 Comparison of the predicted sound pressure level of prominent interaction tones produced by a contra-rotating UAV rotor system with the bottom rotor pitched at $\beta = 0°$ (blue), 4° (red), 8° (yellow) and 12° (purple).

4.5 Chapter summary

This chapter has investigated the effect of cropping the downstream rotor of the rotor systems considered in Chapter 3 of this thesis and has also considered the effect of adjusting the pitch angle of the lower rotor blades of a rotor system with straight blades. Predictions and measurements were presented and showed good agreement.

The trajectory of the tip vortex produced by the top rotor was estimated for the cases with straight rotor blades. It was observed that the tip vortex impinged on the lower rotor at similar locations regardless of whether the bottom rotor was cropped or uncropped.

Cropping the bottom rotor was shown to reduce the impulsive noise generated by the outer portion of the top rotor blades. Cropping the bottom rotor blades also reduced the noise which was generated by the interaction of the tip vortex with the bottom rotor blades. It was also observed that as the blade skew angle increased, the magnitude of the noise generated by the outer portions of the lower rotor blades decreased.

The overall sound power level radiated from the rotor systems with the cropped lower rotor was also shown to decrease as the blade skew angle increased.

Additionally, the effect of the pitch angle of the bottom rotor on the level of the interaction tones was explored. Acoustic measurements were taken at the University of Auckland's anechoic chamber with the bottom rotor pitched at $\beta = 0°$, $4°$, $8°$ and $12°$. The total thrust level was kept constant whilst the bottom rotor speed was decreased as the pitch angle was increased. It was observed that the sound pressure level of the first interaction tone did not change significantly as the blade pitch angle increased. No clear trend was observed for the other tones.

5 Conclusion

The objective of this thesis was to further the understanding of the noise produced by contra-rotating UAV rotor systems. A noise prediction method was developed and validated. This prediction method was used to identify the noise generating mechanisms. Based on this understanding, noise reduction methods were developed. This chapter summaries the key results and findings from each chapter. The implications of key findings are also discussed. Additionally, future extensions of this work are suggested.

5.1 Summary of key results

5.1.1 Chapter 2 results

A CFD simulation method and a semi-analytical model were developed and were used to calculate the unsteady loading on the blades of a contra-rotating rotor system. It was shown that there was reasonable agreement between the periodic unsteady loading on the top rotor blades predicted using the semi-analytical model and the CFD simulations. The periodic unsteady loading on the bottom rotor blades is caused by their interaction with the bound potential field, viscous wakes, and tip vortices from the top rotor.

A frequency domain method was presented for predicting the interaction tones produced by the periodic loading on the rotor blades. This method was used to predict the sound pressure level directivity for a number of different interaction tones produced by two different rotor systems using loading data taken from the CFD simulations and semi-analytical models. These predictions were in generally good agreement with measurements, indicating the importance of the bound potential field interaction noise source for this particular case. The effect of rotor spacing was also investigated using data from two CFD simulations and also the semi-analytical models. There was modest agreement between the predictions and the measurements, however the predictions captured the strong decay of the level of these tones as rotor spacing increased.

5.1.2 Chapter 3 results

CFD simulations were used to predict the unsteady loading on the straight and skewed blades of a contra-rotating UAV rotor system operating at two different speed settings. This loading data was used in either a time- or frequency domain acoustic analogy method to predict radiated acoustic pressure time history and sound pressure levels of interaction tones. A semi-analytical model was also used to assess the importance of the bound potential field interaction noise source. It was observed that increasing the blade skew angle generally reduced the level of the prominent interaction tones at many observer locations. The causes of the noise reduction were investigated, and it was shown to be in-part due to the de-phasing of the acoustic pressure impulses radiated from different radii along the blade span. These predictions were compared with experimental measurements and showed excellent agreement – confirming the validity of the findings.

5.1.4 Chapter 4 results

This chapter investigated the effect of cropping the downstream rotor of the rotor systems considered in Chapter 3. The trajectory of the tip vortex produced by the top rotor was estimated and it was shown that cropping the downstream rotor did not significantly affect the tip vortex trajectory. Cropping the downstream rotor was also shown to reduce the magnitude of the impulsive noise generated by the outer portion of the top rotor blades and reduce the influence of the tip vortex interaction loading on the bottom rotor. It was also shown that as the blade skew angle increased, the radiated noise levels from both the top and bottom rotor blades decreased.

This chapter also investigated the effect of changing the pitch of the bottom rotor whilst keeping the total rotor thrust constant. It was observed that the level of the first interaction tone did not change significantly as the blade pitch angle was changed. There was no clear trend for the higher frequency tones.

5.2 Key findings and implications

Objective 1 was to identify the physical mechanisms that generates interaction tones. This thesis has shown that the unsteady loading produced on the blades due to the bound potential field interaction is the dominant source of noise generation for the contra-rotating UAV rotor systems considered here.

Objective 2 was to develop prediction methods for tonal noise produced by a contra-rotating UAV rotor system. CFD simulations and semi-analytical models were used to calculate the unsteady loading on the blades which were used as an input to the frequency domain acoustic analogy method to calculate sound pressure level of interaction tones and acoustic pressure time-histories. The results were validated by comparing with the results produced from Farassat's Formulation 1A code and experimental measurements. The frequency domain acoustic analogy was used to more rapidly to calculate the sound pressure level of interaction tones when compared with the Farassat's time domain code.

Objective 3 was to identify the effect of blade skew on the interaction tones. After validating that the significant contributor of unsteady loading was the bound potential field interactions, it was necessary to attenuate this effect. One method proposed was to change the skew angle of the blades. Using the methods developed previously, the effect of blade skew on the unsteady loading and the resulting interaction tones was investigated.

It was found that with increasing blade skew, the unsteady loading, and the resulting acoustic pressure radiated from different radii, was de-phased. This reduced the sound pressure level of the prominent interaction tones produced by a contra-rotating UAV rotor system. There was little compromise in the aerodynamic performance as the skew angle was varied for the cases studied in this thesis.

Objective 4 was to investigate the effect of blade cropping on the interaction tones. The tip vortex interaction is a significant contributor to the unsteady loading on the bottom rotor blades of a contra-rotating UAV rotor system. The method proposed to reduce this effect was to crop the blades of the bottom rotor. This effect was investigated using experiments and CFD simulations.

The results conveyed that cropping the bottom blades reduced the unsteady loading on the outer portion of the top and bottom rotor blades which decreased the sound pressure level of prominent interaction tones. For a fair comparison, the pitch angle of the bottom rotor was varied to ensure that it produced the same thrust levels as the uncropped blades at the corresponding rotational speed.

Objective 5 was to investigate the effect of pitch angle of the bottom rotor on the interaction tones. The pitch angle and the rotational speed of the bottom rotor was varied such that the total thrust level was kept constant, and the pitch angle and rotational speed of the top rotor was kept constant. This investigation was explored using experimental and numerical simulations.

It was found that the sound pressure level of the first interaction tone was similar for all pitch angles. However, there was no clear trend for the higher frequency interaction tones.

5.3 Future work

This section discusses the future work that could be performed to further understand the noise produced by a contra-rotating UAV rotor system.

The work described in this thesis relied significantly on data from CFD simulations. While this provides an accurate model of the flow field and loading, it requires large computational resources. Developing low-fidelity models for the viscous wake and tip vortex interaction noise sources would be useful as a design tool for developing quiet contra-rotating UAV rotor systems.

Multi-wire hotwire anemometry measurements could be performed to measure the unsteady flow field produced by a contra-rotating UAV rotor system. These measurements could be used to tune analytical models for the unsteady flow field associated with the bound potential field, tip vortex and viscous wakes of the rotors.

This thesis has also focussed on measurements of isolated rotor systems operating in hover. Further investigations should be made of such rotor systems in forward flight, take-off, and landing as well as installed on a UAV and/or adjacent to other similar rotor systems.

References

[1] Zawodny, N. S., Boyd Jr., D. D., and Burley, C. L. "Acoustic Characterization and Prediction of Representative, Small-Scale Rotary-Wing Unmanned Aircraft System Components." *72nd American Helicopter Society (AHS) Annual Forum*, No. 1, 2016, pp. 34–48.

[2] Nardari, C., Casalino, D., Polidoro, F., Coralic, V., Brodie, J., and Lew, P. T. "Numerical and Experimental Investigation of Flow Confinement Effects on UAV Rotor Noise." *25th AIAA/CEAS Aeroacoustics Conference*, 2019. https://doi.org/10.2514/6.2019-2497.

[3] Robison, R. A. V., and Peake, N. "Noise Generation by Turbulence-Propeller Interaction in Asymmetric Flow." *Journal of Fluid Mechanics*, Vol. 758, 2014, pp. 121–149. https://doi.org/10.1017/jfm.2014.487.

[4] Glegg, S. A. L., Devenport, W., and Alexander, N. "Broadband Rotor Noise Predictions Using a Time Domain Approach." *Journal of Sound and Vibration*, Vol. 335, 2015, pp. 115–124. https://doi.org/10.1016/j.jsv.2014.09.007.

[5] Glegg, S. A. L. "Prediction of Blade Wake Interaction Noise Based on a Turbulent Vortex Model." *AIAA Journal*, Vol. 29, No. 10, 1991, pp. 1545–1551. https://doi.org/10.2514/3.10774.

[6] Brooks, T. F., Pope, D. S., and Marcolini, M. A. "Airfoil Self-Noise and Prediction." *NASA Reference Publicaton 1218*, 1989.

[7] Peake, N., and Parry, A. B. "Modern Challenges Facing Turbomachinery Aeroacoustics." *Annual Review of Fluid Mechanics*, 2011, pp. 227–248. https://doi.org/10.1146/annurev-fluid-120710-101231.

[8] Hanson, D. B. "Noise of Counter-Rotation Propellers." *Journal of Aircraft*, Vol. 22, No. 7, 1985, pp. 609–617. https://doi.org/10.2514/3.45173.

[9] Majjigi, R. K., Uenishi, K., and Gliebe, P. R. "An Investigation of Counterrotating Tip Vortex Interaction." *NASA Contract Report 185135*, 1989.

[10] Kingan, M. J., and Self, R. H. "Counter-Rotation Propeller Tip Vortex Interaction Noise." *15th AIAA/CEAS Aeroacoustics Conference*, 2009. https://doi.org/10.2514/6.2009-3135.

[11] Metzger, F. B., and Brown, P. C. "Results of Acoustic Tests of a Prop-Fan Model." *Journal of Aircraft*, Vol. 25, No. 7, 1988, pp. 653–658. https://doi.org/10.2514/3.45637.

[12] Quaglia, M. E., Léonard, T., Moreau, S., and Roger, M. "A 3D Analytical Model for Orthogonal Blade-Vortex Interaction Noise." *Journal of Sound and Vibration*, Vol. 399, 2017, pp. 104–123. https://doi.org/10.1016/j.jsv.2017.03.023.

[13] Tormen, D., Giannattasio, P., Zanon, A., De Gennaro, M., and Kühnelt, H. "Semi-Analytical Tip Vortex Model for Fast Prediction of Contrarotating Open Rotor Noise." *AIAA Journal*, Vol. 59, No. 5, 2021, pp. 1629–1644. https://doi.org/10.2514/1.J059314.

[14] Moreau, S., and Roger, M. "Advanced Noise Modeling for Future Propulsion Systems." *International Journal of Aeroacoustics*, Vol. 17, 2018, pp. 576–599. https://doi.org/10.1177/1475472X18789005.

[15] Blandeau, V. P., and Joseph, P. F. "Broadband Noise Due to Rotor-Wake/Rotor Interaction in Contra-Rotating Open Rotors." *AIAA Journal*, Vol. 48, No. 11, 2010, pp. 2674–2686. https://doi.org/10.2514/1.J050566.

[16] Kingan, M. J., and Sureshkumar, P. "Open Rotor Centrebody Scattering." *Journal of Sound and Vibration*, Vol. 333, No. 2, 2014, pp. 418–433. https://doi.org/10.1016/j.jsv.2013.08.010.

[17] Parry, A. B., Kingan, M., and Tester, B. J. "Relative Importance of Open Rotor Tone and

Broadband Noise Sources." *17th AIAA/CEAS Aeroacoustics Conference 2011 (32nd AIAA Aeroacoustics Conference)*, No. June, 2011, pp. 5–8. https://doi.org/10.2514/6.2011-2763.

[18] Kingan, M. J., Ekoule, C. M., Parry, A. B., and Britchford, K. M. "Analysis of Advanced Open Rotor Noise Measurements." *20th AIAA/CEAS Aeroacoustics Conference*, No. June, 2014. https://doi.org/10.2514/6.2014-2745.

[19] Ekoule, C. M., McAlpine, A., Parry, A. B., Kingan, M. J., and Sohoni, N. G. "Development of a Hybrid Method for the Prediction of Advanced Open Rotor Tone Noise." *23rd AIAA/CEAS Aeroacoustics Conference*, 2017. https://doi.org/10.2514/6.2017-3870.

[20] Parry, A. B., and Kingan, M. J. "Acoustic Theory of the Many-Bladed Contra-Rotating Propeller: Physics of the Wake Interaction Noise Critical Sources." *Journal of Fluid Mechanics*, 2019, pp. R11–R112. https://doi.org/10.1017/jfm.2019.755.

[21] Parry, A. B., and Kingan, M. J. "Acoustic Theory of the Many-Bladed Contra-Rotating Propeller: The Event Line and the Precession of the Interaction Source." *Journal of Fluid Mechanics*, Vol. 909, 2020, pp. 1–11. https://doi.org/10.1017/jfm.2020.992.

[22] Parry, B. A. B. "The Effect of Blade Sweep on the Reduction and Enhancement of Supersonic Propeller Noise." *Journal of Fluid Mechanics*, Vol. 293, 1995, pp. 181–206.

[23] Kingan, M. J., and Parry, A. B. "Acoustic Theory of the Many-Bladed Contra-Rotating Propeller : The Effects of Sweep on Noise Enhancement and Reduction." *Journal of Sound and Vibration*, Vol. 468, 2020, p. 115089. https://doi.org/10.1016/j.jsv.2019.115089.

[24] Kingan, M. J., and Parry, A. B. "Time-Domain Analysis of Contra-Rotating Propeller Noise : Wake Interaction with a Downstream Propeller Blade." *Journal of Fluid Mechanics*, 2020. https://doi.org/10.1017/jfm.2020.504.

[25] Walsh, G., Brentner, K. S., Jacobellis, G., and Gandhi, F. "An Acoustic Investigation of a Coaxial Helicopter in High-Speed Flight." *Annual Forum Proceedings - AHS International*, Vol. 1, 2016, pp. 156–187.

[26] Kim, H. W., R, K. A., Duraisamy, K., and Brown, R. E. "Interactional Aerodynamics and Acoustics of a Propeller-Augmented Compound Coaxial Helicopter." *9th American Helicopter Society Aeromechanics Specialists' Meeting*, No. January, 2008, pp. 23–25.

[27] Kim, H. W., Duraisamy, K., and Brown, R. "Aeroacoustics of a Coaxial Rotor in Level Flight." *Annual Forum Proceedings - AHS International*, Vol. 1, 2008, pp. 649–662.

[28] Kim, H. W., and Brown, R. E. "Modelling the Aerodynamics of Coaxial Helicopters – from an Isolated Rotor to a Complete Aircraft." *Springer Proceedings in Physics*, Vol. 124, 2008, pp. 45–59. https://doi.org/10.1007/978-3-540-85190-5_4.

[29] Yoon, S., Lee, H. C., and Pulliam, T. H. "Computational Study of Flow Interactions in Coaxial Rotors." *American Helicopter Society International - AHS Specialists' Conference on Aeromechanics Design for Vertical Lift 2016*, 2016, pp. 98–108.

[30] Barbely, N., and Komerath, N. "Coaxial Rotor Flow Phenomena in Forward Flight." *SAE Technical Papers*, Vols. 2016-Septe, No. September, 2016. https://doi.org/10.4271/2016-01-2009.

[31] Lakshminarayan, V. K., and Baeder, J. D. "Computational Investigation of Microscale Coaxial-Rotor Aerodynamics in Hover." *Journal of Aircraft*, Vol. 47, No. 3, 2010, pp. 940–955. https://doi.org/10.2514/1.46530.

[32] Shukla, D., and Komerath, N. "Drone Scale Coaxial Rotor Aerodynamic Interactions Investigation." *Journal of Fluids Engineering, Transactions of the ASME*, Vol. 141, No. 7,

2019. https://doi.org/10.1115/1.4042162.

[33]   McKay, R. S., Kingan, M. J., Go, S. T., and Jung, R. "Experimental and Analytical Investigation of Contra-Rotating Multi-Rotor UAV Propeller Noise." *Applied Acoustics*, Vol. 177, 2021. https://doi.org/10.1016/j.apacoust.2020.107850.

[34]   Chaitanya, P., Joseph, P., Prior, S. D., and Parry, A. B. "On the Optimum Separation Distance for Minimum Noise of Contra-Rotating Rotors." *Journal of Sound and Vibration*, Vol. 535, 2022, p. 110456. https://doi.org/10.1016/j.jsv.2022.117032.

[35]   Torija, A. J., Chaitanya, P., and Li, Z. "Vehicles Psychoacoustic Analysis of Contra-Rotating Propeller Noise for Unmanned Aerial Vehicles." *Journal Acoustical Society of America*, Vol. 835, 2021. https://doi.org/10.1121/10.0003432.

[36]   Zhong, S., Ma, Z., Zhou, P., Wu, H., and Zhang, X. "Predicting the Aerodynamic Noise of Counter-Rotating Coaxial Rotors." *Journal of Sound and Vibration*, 2022, p. 117487. https://doi.org/10.1016/j.jsv.2022.117487.

[37]   Cabell, R., McSwain, R., and Grosveld, F. "Measured Noise from Small Unmanned Aerial Vehicles." *NOISE-CON Paper 20160010139*, 2016, pp. 1–10.

[38]   Kloet, N., Watkins, S., and Clothier, R. "Acoustic Signature Measurement of Small Multi-Rotor Unmanned Aircraft Systems." *International Journal of Micro Air Vehicles*, Vol. 9, No. 1, 2017, pp. 3–14. https://doi.org/10.1177/1756829316681868.

[39]   Hioka, Y., Kingan, M., Schmid, G., McKay, R., and Stol, K. A. "Design of an Unmanned Aerial Vehicle Mounted System for Quiet Audio Recording." *Applied Acoustics*, Vol. 155, 2019, pp. 423–427. https://doi.org/10.1016/j.apacoust.2019.06.001.

[40]   Intaratep, N., Nathan Alexander, W., Deveport, W. J., Grace, S. M., and Dropkin, A. "Experimental Study of Quadcopter Acoustics and Performance at Static Thrust Conditions." *22nd AIAA/CEAS Aeroacoustics Conference, 2016*, 2016, pp. 1–14. https://doi.org/10.2514/6.2016-2873.

[41]   Lu, Z., Liu, Y., Debiasi, M., and Khoo, B. C. "Acoustic Characteristics of a Multi-Rotor MAV and Its Noise Reduction Technology." *Proceedings of the INTER-NOISE 2016 - 45th International Congress and Exposition on Noise Control Engineering: Towards a Quieter Future*, No. August, 2016, pp. 725–735.

[42]   Feight, J. A., Jacob, J. D., and Gaeta, R. J. "Acoustic Characterization of a Multi-Rotor UAS as a First Step towards Noise Reduction." *AIAA SciTech Forum - 55th AIAA Aerospace Sciences Meeting*, No. January, 2017. https://doi.org/10.2514/6.2017-1174.

[43]   Tinney, C. E., and Sirohi, J. "Multirotor Drone Noise at Static Thrust." *AIAA Journal*, Vol. 56, No. 7, 2018, pp. 2816–2826. https://doi.org/10.2514/1.J056827.

[44]   Vieira, A. A., Lau, F., and Mort, P. "A New Computational Framework for UAV Quadrotor Noise Prediction." *5th CEAS Air & Space Conference*, 2015, pp. 1–14.

[45]   Stephenson, J. H., Weitsman, D., and Zawodny, N. S. "Effects of Flow Recirculation on Unmanned Aircraft System (UAS) Acoustic Measurements in Closed Anechoic Chambers." *The Journal of the Acoustical Society of America*, Vol. 145, No. 3, 2019, pp. 1153–1155. https://doi.org/10.1121/1.5092213.

[46]   McKay, R., and Kingan, M. J. "Experimentally Isolating Multi-Rotor UAV Propeller Noise from Motor Noise." *25th International Congress on Sound and Vibration 2018*, 2018.

[47]   McKay, R., and Kingan, M. "Multi-Rotor Unmanned Aerial System Noise: Quantifying the Motor's Contribution." *24th Acoustical Society New Zealand Conference, no. 1*, 2018.

[48] McKay, R. S., and Kingan, M. J. "Multirotor Unmanned Aerial System Propeller Noise Caused by Unsteady Blade Motion." *25th AIAA/CEAS Aeroacoustics Conference*, 2019. https://doi.org/10.2514/6.2019-2499.

[49] Whelchel, J., Alexander, W. N., and Intaratep, N. "Propeller Noise in Confined Anechoic and Open Environments." *AIAA Scitech 2020 Forum*, Vol. 1 PartF, No. January, 2020, pp. 1–25. https://doi.org/10.2514/6.2020-1252.

[50] Glegg, S., and Devenport, W. *Aeroacoustics of Low Mach Number Flows: Fundamentals, Analysis, and Measurement*. Academic Press, 2017.

[51] Casalino, D., Grande, E., Romani, G., Ragni, D., and Avallone, F. "Definition of a Benchmark for Low Reynolds Number Propeller Aeroacoustics." *Aerospace Science and Technology*, 2021. https://doi.org/10.1016/j.ast.2021.106707.

[52] Castelli, M. R., Garbo, F., and Benini, E. "Numerical Investigation of Laminar to Turbulent Boundary Layer Transition on a Naca 0012 Airfoil for Vertical-Axis Wind Turbine Applications." *Wind Engineering*, Vol. 35, No. 6, 2011, pp. 661–685. https://doi.org/10.1260/0309-524X.35.6.661.

[53] Menter, F. R., Langtry, R. B., Likki, S. R., Suzen, Y. B., Huang, P. G., and Völker, S. "A Correlation-Based Transition Model Using Local Variables - Part I: Model Formulation." *Journal of Turbomachinery*, Vol. 128, No. 3, 2006, pp. 413–422. https://doi.org/10.1115/1.2184352.

[54] Langtry, R. B., Menter, F. R., Likki, S. R., Suzen, Y. B., Huang, P. G., and Völker, S. "A Correlation-Based Transition Model Using Local Variables - Part II: Test Cases and Industrial Applications." *Journal of Turbomachinery*, Vol. 128, No. 3, 2006, pp. 423–434. https://doi.org/10.1115/1.2184353.

[55] Chandar, D., Boppana, V., and Kumar, V. "A Comparative Study of Different Overset Grid Solvers between OpenFoam, Star-CCM+ and ANSYS Fluent." *AIAA Aerospace Sciences Meeting, 2018*, No. 210059, 2018. https://doi.org/10.2514/6.2018-1564.

[56] Ventura Diaz, P., and Yoon, S. "High-Fidelity Computational Aerodynamics of Multi-Rotor Unmanned Aerial Vehicles." *AIAA Aerospace Sciences Meeting, 2018*, No. 210059, 2018, pp. 1–22. https://doi.org/10.2514/6.2018-1266.

[57] Lakshminarayan, V. K. *Computational Investigation of Micro- Scale Coaxial Rotor Aerodynamics in Hover*. PhD Thesis, University of Maryland, College Park, 2010.

[58] Chan, Wi. M., Gomez, R. J., Rogers, S. E., and Buning, P. G. Best Practices in Overset Grid Generation. 2002.

[59] *ANSYS Fluent Theory Guide*. ANSYS Inc., Canonsburg, PA,.

[60] Carazo, A., Roger, M., and Omais, M. "Analytical Prediction of Wake-Interaction Noise in Counter-Rotation Open Rotors." *17th AIAA/CEAS Aeroacoustics Conference*, 2011. https://doi.org/10.2514/6.2011-2758.

[61] Landahl, M. T. *Unsteady Transonic Flow*. Cambridge University Press, 1989.

[62] Parry, A. B. *Theoretical Prediction of Counter-Rotating Propeller Noise*. PhD Thesis, University of Leeds, 1988.

[63] Kemp, N. H. "On the Lift and Circulation of Airfoils in Some Unsteady-Flow Problems." *Journal of the Aeronautical Sciences*, 1952. https://doi.org/10.2514/8.2433.

[64] Katz, J., and Plotkin, A. *Low Speed Aerodynamics*. Cambridge University Press, 2001.

[65] Hanson, D. B., and Parzych, D. J. "Theory for Noise of Propellers in Angular Inflow with Parametric Studies and Experimental Verification." *NASA Contractor Report*, 1993.

[66] Goldstein, M. "Unified Approach to Aerodynamic Sound Generation in the Presence." *Journal of the Acoustical Society of America*, 2014, pp. 497–509. https://doi.org/10.1121/1.1903283.

[67] McKay, R. S. *Multirotor Unmanned Aerial Vehicle Propeller Noise*. PhD Thesis, University of Auckland, 2021.

[68] Brentner, K. S. "Prediction of Helicopter Rotor Discrete Frequency Noise - A Computer Program Incorporating Realistic Blade Motions and Advanced Acoustic Formulation." *NASA TM 87721*, Vol. 25, No. 5, pp. 420–427. https://doi.org/10.2514/3.45598.

[69] Farassat, F., and Succi, G. P. "A Review of Propeller Discrete Frequency Noise Prediction Technology with Emphasis on Two Current Methods for Time Domain Calculations." *Journal of Sound and Vibration*, 1980. https://doi.org/10.1016/0022-460X(80)90422-8.

[70] Parry, A. B., Howarth, N., and Taylor, M. D. Aeroengine, United States Patent Application, , 2010.

[71] Farassat, F. "Derivation of Formulations 1 and 1A of Farassat." *Nasa/TM-2007-214853*, Vol. 214853, No. March, 2007, pp. 1–25.

[72] Jung, R., Kingan, M. J., Dhopade, P., Sharma, R., and McKay, R. S. "Investigation of the Interaction Tones Produced by Contra-Rotating Unmanned Aerial Vehicle Rotor Systems." *AIAA Journal*, 2023, pp. 1–16. https://doi.org/https://doi.org/10.2514/1.J062531.

[73] Kemp, N. H. "On the Lift and Circulation of Airfoils in Some Unsteady-Flow Problems." *Journal of the Aeronautical Sciences*, Vol. 19, No. 10, 1952, pp. 713–714. https://doi.org/10.2514/8.2433.

[74] Brentner, K. S. "Prediction of Helicopter Rotor Discrete Frequency Noise - A Computer Program Incorporating Realistic Blade Motions and Advanced Acoustic Formulation." *NASA TM 87721*, Vol. 25, No. 5, pp. 420–427.